Cranfield University

Divya Tiwari

Photochemical Growth of Metal Nanoparticles on Domain Patterned Ferroelectric Surfaces

School of Applied Sciences

PhD

Cranfield University

School of Applied Sciences

PhD Thesis

2009

Divya Tiwari

Photochemical Growth of Metal Nanoparticles on Domain Patterned Ferroelectric Surfaces

Supervisor Dr Steve Dunn

Academic Year 2006 to 2009

Abstract

In this work, the growth of metal nanoparticles on domain patterned ferroelectric $Pb(Zr_xTi_{1-x})O_3$ and $LiNbO_3$ by photochemical reaction is demonstrated. The photochemical properties and phenomena occurring on the surface of $Pb(Zr_xTi_{1-x})O_3$ and $LiNbO_3$ under ultraviolet illumination are investigated. Ferroelectric materials possess a reversible spontaneous polarisation that has an effect on photochemical reactivity of a surface. Since the spontaneous polarisation is reversible, a desired pattern can be drawn on a ferroelectric surface in the form of domains. A combination of domain patterning and domain specific surface reactions can lead to fabrication of complex nanostructures.

It is found that on a PZT (30/70) thin film, under UV irradiation, metal deposition occurred only on C^+ domains and no deposition occurred on C^- domains. Hence, the chemical reactivity of ferroelectric surface was found to be dependent on the polarisation of domain that is underlying the surface. Annealing of PZT samples at high temperatures alters the defect concentration of the PZT as shown by an increase in the deposition of silver on the surface. When the PZT samples were annealed in air at temperatures ranging from 530-690°C the silver deposition increased by more than 150% and the size of deposited silver clusters increased by four times. The photochemical properties of PZT thin films of different compositions $PbZr_{0.3}Ti_{0.7}O_3$, $PbZr_{0.52}Ti_{0.48}O_3$ and $PbZr_{0.7}Ti_{0.3}O_3$ were investigated by undertaking silver nanocluster deposition experiments. The composition of PZT film (Zr/Ti ratio) affects silver deposition such that on $PbZr_{0.3}Ti_{0.7}O_3$ silver deposits only on C^+ domains, whereas $PbZr_{0.52}Ti_{0.48}O_3$ and $PbZr_{0.7}Ti_{0.3}O_3$ experience deposition on both C^+ and C^- domains. This difference in silver deposition pattern is shown to be due to the difference in width of the space charge region and band

gap of the three samples. The impact of size of poled pattern on silver deposition at the surface is shown. It is found that for smaller size of C^+ domains (smaller than 1 μm) the amount and size of deposited silver decreased with the decrease in domain size. On a PZT surface, formation of spherical, triangular and hexagonal nanoplates of gold via photoreduction has also been demonstrated.

Silver cation reduction on C^+ and C^- domains of ferroelectric lithium niobate (LN) by photochemical and photoelectric process is demonstrated. The interaction of photoelectric and domain dependent influences can be observed in $LiNbO_3$ due to the low electron affinity (ca 1.1-1.5eV). The impact of composition of LN on the photoreduction of silver has been shown. It is found that the photochemical reactivity of MgO-doped LN is significantly higher as compared to non-doped LN. The energy and intensity of incident photon is also found to have an impact on the photoreduction of silver on LN surface. In addition to this, deposition of Al and Mn nanoparticles on LN surface by means of photoreduction reaction has been demonstrated. It is shown that for a metal to photoreduce on C^+ domain of a ferroelectric material, the reduction potential of the metal has to be within the band-gap of the material. It is shown that under atmospheric conditions, it is possible to selectively adsorb molecules of opposite charge on the surface of LN due to uncompensated polarisation charge.

Acknowledgments

I would like to thank Dr Steve Dunn for his invaluable supervision and support during this work.

I would like to thank Dr Qi Zhang, Dr Paul Jones, Dr Zhaorong Huang, Dr Rob Dorey, Dr Chris Shaw, Ms Enza Giaracuni, Mr Andrew Stallard, Mr Matthew Taunt, Dr Matthew Kershaw and Ms Christine Kimpton for their helping hand.

I would like to thank my husband Dr Ashutosh Tiwari for his unwavering support and encouragement, and my four year old son Achintya for his love and quiet support. I would like to thank my parents Mr P N Shukla and Mrs Vandana Shukla for their encouragement and moral support. I would like to thank my parents-in-law and the rest of my family for their support.

Table of Contents

List of figures

List of tables

1. Introduction

1.1 Motivation

After the discovery of ferroelectricity in Rochelle Salt by Valasek[1] in 1920, ferroelectric materials have emerged as a very promising material group with wide applications such as memory devices[2], waveguides[3] and numerous novel applications including micro electromechanical systems (MEMS)[4,5,6]. In 2002, Kalinin *et al.*[7] proposed a novel application of ferroelectrics 'ferroelectric lithography', which facilitates the growth of metal nanoparticles on pre-defined locations on a ferroelectric surface. In ferroelectric materials, polarisation of a domain has an effect on the surface properties and this leads to some domain specific reactions. Therefore, domain patterning combined with domain specific reactivity can facilitate fabrication of complex structures[7,8].

Owing to great scientific and technological interest in the synthesis of devices with micro and nano scale dimensions, several methods for the growth of nanostructures have been reported in literature e.g. Nanoimprint lithography[9], Dip-pen Lithography[10] and approaches based on ink jetprinter strategies[11], approaches based on AFM systems[12] etc. These methods have various limitations e.g. some are limited in down scaling the nanowire diameter below 50 nm, operating on one class of material at a time and some are limited by the types of shape that can be grown.

Ferroelectric lithography technique possesses several advantages over traditional methods reported in literature e.g. it has an advantage of growing nanoparticles of various morphologies in one process and it can position multiple components made of various materials into pre-defined configuration. In addition to this, ferroelectric material can be patterned at length scales that range from tens of nanometres to many centimetres. Another advantage of ferroelectric lithography technique is that the

ferroelectric materials used e.g. lead zirconate titanate (PZT) and lithium niobate (LN) are mechanically stable and rigid, which allows the reuse of the same substrate for many deposition test series. Due to these factors, ferroelectric lithography bears a huge potential for synthesis of complex nanostructures and microelectronic devices. To facilitate the control of synthesis process it is important to gain an understanding of the properties and phenomenon occurring on the surface of ferroelectric material.

The research presented in this thesis is a study of photochemical deposition processes on two different ferroelectric materials. First is polycrystalline PZT, and second is single crystal LN. In order to control and optimise the process of metal growth, the chemical and physical interactions occurring on the surface of the ferroelectric material under the non equilibrium conditions by super band gap irradiation must be understood. Work focussing on the semiconductor nature of a ferroelectric has shed light on what is happening at the interface between a poled ferroelectric material and its wider environment. This understanding is achieved by tracking the change in photochemical reactivity of ferroelectric lead zirconate titanate (PZT) and lithium niobate (LN) by varying experimental parameters such as composition of material, temperature of annealing, incident photon energy and metal salts.

1.2 Overview of thesis

The organisation of this thesis is as follows: Chapter 2 is a literature review of photochemical deposition on ferroelectric materials. It starts with an overview of ferroelectrics, semiconductors, ferroelectric materials as semiconductors, and then discusses the photochemistry at ferroelectric-solution interface. Specific properties of PZT and LN are also discussed in this chapter. Chapter 3 is dedicated to experimental procedure used in the research work. Chapter 4 talks about the photoreduction of

metallic salt solutions on domain patterned PZT. The effects of varying the stoichiometric composition of PZT, annealing temperatures of PZT, domain size and size of ferroelectric on the photochemical deposition process are demonstrated. Formation of nanoplates of silver via photoreduction is also demonstrated. Chapter 5 demonstrates photochemical and photoelectric cation reduction on LN surface. Photoreduction of Al and Mn salts on LN is shown in this chapter. Impact of energy and intensity of incident photon on photochemistry at LN surface is also shown. Selective molecular adsorption of stearic acid on LN surface is demonstrated. Chapter 6 provides a summary of the conclusions drawn from the work and future work is discussed.

References

[1] J. Valasek, *Phys. Rev*., 15, 537 (1920)

[2] M. Dawber, K. M. Rabe, and J. F. Scott, *Rev. Mod. Phys.*, 77, 1083 (2005)

[3] F. Chen, M. Stepić, C. E. Rüter, D. Runde, D. Kip, V. Shandarov, O. Manela, and M.Segev, *Opt. Express,* 13, 4314 (2005)

[4] D. L. Polla and L. F. Francis, *Annu. Rev. Mater. Sci*., 28, 563–97 (1998)

[5] D. M. Dabbs and I. A. Aksay, *Annu. Rev. Phys. Chem*., 51, 601–622 (2000)

[6] U. P. Schonholzer and L. J. Gauckler, *Adv. Mater*., 11, 630–632 (1999)

[7] S.V. Kalinin, D. A. Bonnell, T. Alvarez, X. Lei, J. H. Ferris, S. Dunn, Q. Zhang, *Nanoletters,* 2, 589 (2002)

[8] S.V. Kalinin, D.A. Bonnell, T. Alvarez, X. Lei, Z. Hu, R. Shao and J.H. Ferris, *Adv. Mater.,* 16, 795 (2004)

[9] S.Y. Chou, *MRS Bull.*, 26**,** 512 (2001)

[10] R.D. Piner, J. Zhu, F. Xu, S. Hong, and C.A. Mirkin, *Science,* 283**,** 661 (1999)

[11] T.R. Hughes *et al*., *Nat. Biotechnol.,* 19**,** 342 (2001)

[12] L. L. Sohn and R. L.Willett, *Appl. Phys. Lett.*, 67, 1552 (1995)

2. Literature Review

2.1 Ferroelectric Materials

2.1.1. Piezoelectricity

Piezoelectricity is a phenomenon in which a crystal can be polarised by the application of mechanical stress. Conversely when an electric field is applied across a piezoelectric crystal, it will change its dimensions i.e. it either expands or contracts. Therefore, the application of pressure to a piezoelectric crystal between two electrodes causes a charge to flow in one direction. Piezoelectricity was first discovered by French scientists J. Curie and P. Curie in 1880[1]. A sub-set of piezoelectrics is pyroelectrics. A pyroelectric material is polar in nature because it possesses a spontaneous polarisation or electric moment per unit volume which is generally temperature dependent. A sub-set of pyroelectrics is ferroelectrics in which the spontaneous polarisation is switchable on the application of an electric field. The relationship between piezoelectrics, pyroelectrics and ferroelectrics is shown in Figure 2.1.

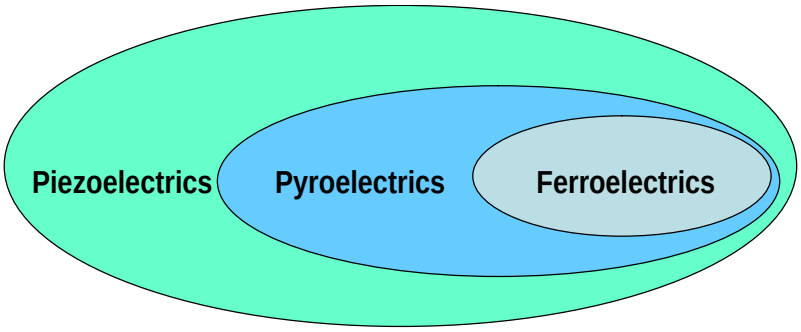

Figure 2.1 Relationship between piezoelectrics, pyroelectrics and ferroelectrics.

2.1.2 Ferroelectricity

Ferroelectricity is the property of a crystal to exhibit two or more orientational states in the absence of an electric field and shift from one to another of these states by the application of an electric field[2]. Jona and Shirane[3] define a ferroelectric crystal as a pyroelectric crystal with reversible polarisation. After the discovery of ferroelectricity in Rochelle Salt[4] in 1920 a large number of ferroelectric crystals have been discovered with their spontaneous polarisation varying from the order of 10^{-7} C/cm^2 (e.g. Rochelle salt 2.5 × 10^{-7} C/cm^2) to 10^{-4} C/cm^2 (e.g. Lithium niobate 0.78 × 10^{-4} C/cm^2). The most frequently applied ferroelectric materials are those with perovskite-type structures with general formula ABO_3 and structure as shown in Figure 2.2. Here A and B are cations such as Pb/Ba and Zr/Ti respectively and O is oxygen anion O^{2-}. In perovskite lead zirconate titanate (PZT) the displacement of body centred cation Zr^{4+}/Ti^{4+} gives rise to a dipole and hence polarisation in the unit cell.

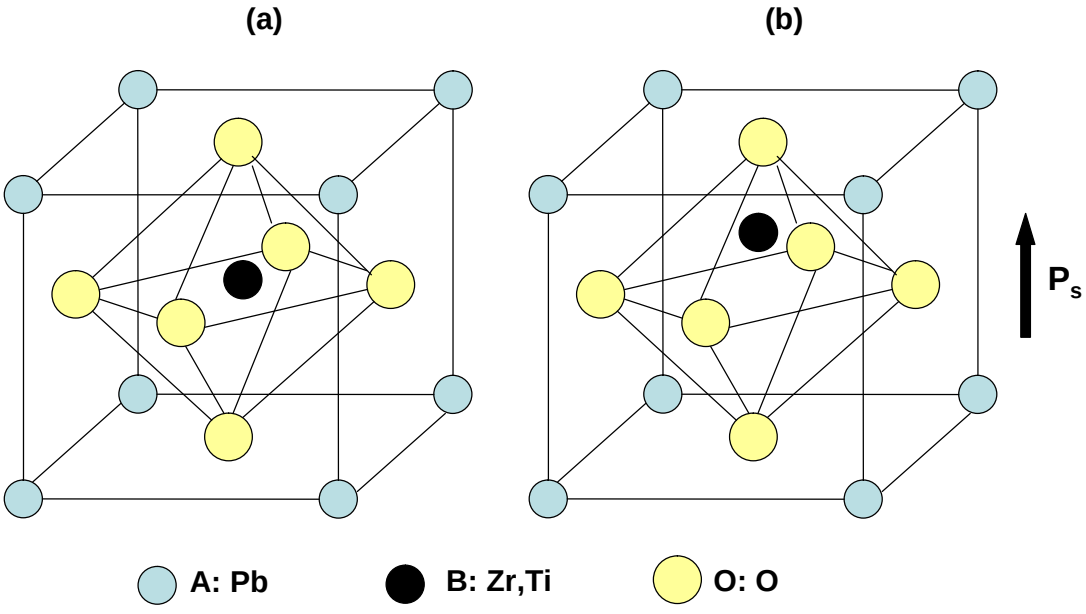

Figure 2.2 (a) A perovskite PZT unit cell. There is no displacement of the central atom and no net dipole moment, therefore no spontaneous polarisation. Figure 2.2 (b) shows the displacement of

Zr/Ti cation and inherent dipole moment resulting in polarisation. The arrow represents the direction of spontaneous polarisation (P_s).

As discussed above, ferroelectric materials are that subset of pyroelectrics in which the spontaneous polarisation can be reversed, at least partially, by the application of electric field. According to Merz and Fatuzzo[5] the relationship between polarisation (P) and electric field (E) in a ferroelectric is given by a hysteresis loop as shown in Figure 2.3 . At low electric field we have a linear relationship between P and E because the field is not large enough to switch any of the dipoles, as the electric field is increased the dipoles will switch in the direction of applied electric field and polarisation increases rapidly up to a stage when all the dipoles are aligned in one direction and saturation state is reached. When the electric field is reversed the polarisation will start to decrease and at zero electric field some dipoles are still aligned in the opposite direction giving a remnant polarisation (P_r). Increasing the electric field will cause the dipoles to align themselves in its direction and at electric field E_c the polarisation reaches zero value. Further increasing the field in a negative direction will eventually cause all the dipoles aligned in that direction.

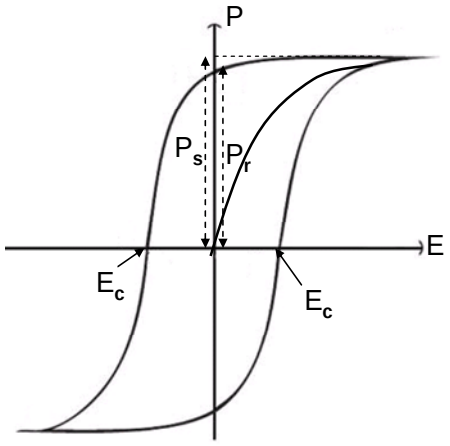

Figure 2.3 A typical ferroelectric hysteresis loop

2.1.3 Domains and domain walls

All ferroelectric materials possess a Curie point (T_c) which is a temperature at which a transition from polar into non-polar phase occurs. When a ferroelectric material is cooled below its Curie point different regions orient themselves in one of the directions in which spontaneous polarisation can develop. The regions of a ferroelectric crystal with uniformly oriented polarisation are called ferroelectric domains and the plane separating two domains is called a domain wall. Unpoled ferroelectric materials tend to form multiple domains so that the total free energy of the crystal is minimised[6]. The total free energy of a crystal is a combination of energy associated with depolarising field, energy associated with the formation of domains etc.

Domains that have polarisation vector pointing in +z direction are 'up'(C^+) domains, in -z direction are 'down'(C^-) domains and the domains in which polarisation direction lies on the surface plane are lateral domains 'a', as shown in Figure 2.4. The boundaries separating 'a-c' domains are called 90º boundaries, and those separating C^+ - C^- domains are 180º boundaries [the name implies the angle between the polarisation vectors in adjacent domains].

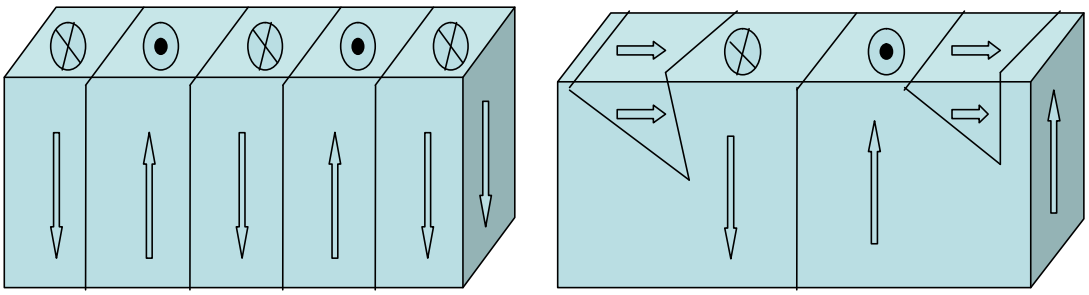

Figure 2.4 Diagram of ferroelectric domain configurations. (a) Depicts domain structure with 180° domains which are referred to as *c* domains. Domains that have polarisation vector pointing in +z direction are 'up'(C^+) domains, in –z directions are 'down'(C^-) domains. (b) Depicts domain

structure that has 90° domain wedges in a region of 180° domains. Domains in which polarisation direction lies on the surface plane are 'a' domains.

2.1.4 Spontaneous polarisation and depolarising field

In a unit cell of a ferroelectric crystal, displacement between centres of positive and negative charge gives rise to spontaneous polarisation. The magnitude and direction of spontaneous polarisation is not uniform throughout the material. The relation between electric displacement (D), field (E) and polarisation (P) is shown in (Equation 2.1.

$$D = \varepsilon_0 E + P \quad \textbf{(Equation 2.1)}$$

ε_0 is permittivity of free space.

According to first Maxwell equation

$$\nabla D = \rho \quad \textbf{(Equation 2.2)}$$

ρ is space-charge density.

Therefore

$$\nabla E = \frac{1}{\varepsilon_0}(\rho - \nabla P) \quad \textbf{(Equation 2.3)}$$

The total polarisation arises from polarisability of the material in an electric field $P_E = \varepsilon_0 \chi E$ and the spontaneous polarisation P_s. χ is the electric susceptibility of the ferroelectric semiconductor and ε_r is dielectric constant of the semiconductor. Therefore (Equation 2.3) becomes

$$\nabla E = \frac{1}{\varepsilon_r \varepsilon_0}(\rho - \nabla P_s) \quad \textbf{(Equation 2.4)}$$

Where $\varepsilon_r = 1 + \chi$

Spontaneous polarisation decreases to zero at surfaces and it varies in the vicinity of defects. Therefore, divergence of spontaneous polarisation is non zero and it acts as a source for a depolarising field. This depolarising field is compensated by internal and/or external screenings[7] which are explained in detail in section 2.3.

2.2 Semiconductors

2.2.1 Electronic structure of solids

In an atom, the electrons are allowed to be in discrete energy levels characterised by their energy; these levels are denoted by 1s, 2s, 2p, 3s...etc. Each energy level can accommodate a maximum of two electrons, of opposite spin orientations (Pauli's exclusion principle). Here we take an example of Li atom that contains 3 electrons, two of which occupy 1s shell and third occupies the 2s shell. When two Li atoms combine through their $2s^1$ electrons, they form doubly occupied binding molecular orbital and an unoccupied antibonding level as shown in Figure 2.5 (a). When 2×3 Li atoms combine, they behave the same resulting in the formation of three doubly occupied bonding and unoccupied antibonding molecular orbital levels as shown in Figure 2.5(b). When 1 mole of Li atoms combine, they form 1 mole (6×10^{23}) of bonding and 1 mole of antibonding molecular orbitals. These 6×10^{23} molecular orbitals are close to each other and they can be considered as continuous band of energy as shown in Figure 2.5 (c). The energy spectrum of a solid is made up of set of energy bands separated by intervals where energy levels are absent. These gaps where energy levels are absent are called forbidden bands or band gap (E_g).

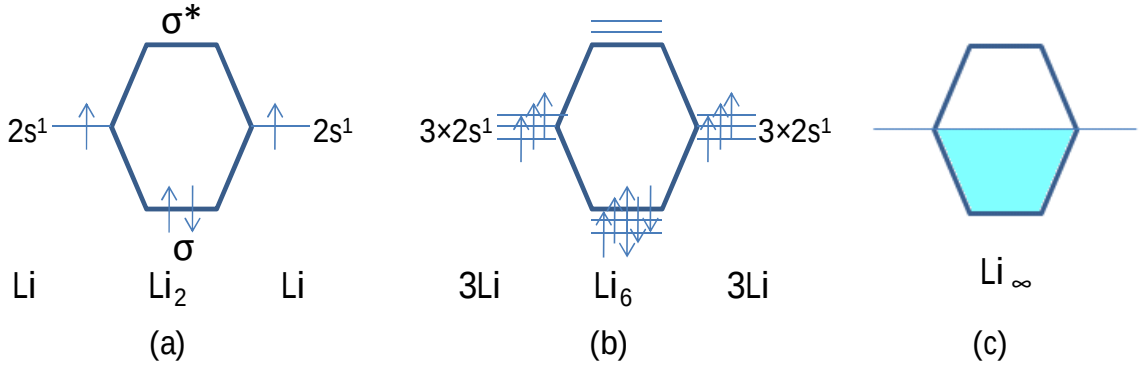

Figure 2.5 A diagram showing formation of an energy band in Lithium. (a) Two Li atoms (b) 3 ×2 Li atoms and (c) 1 mole of Li atoms combine to form an energy band.

Solids can be classified into two major categories – metals and insulators. A metal or conductor is a substance that conducts electricity on the application of an electric field and an insulator can not conduct electricity on the application of an electric field. An energy band that is completely full of electrons can not conduct electricity. Therefore a solid is a conductor when at least one of its bands is partially filled with electrons. By contrast, in an insulator the lower bands are completely filled with electrons and upper bands are completely empty (Figure 2.6). An example of insulator is diamond (Carbon) that has a band gap of 7 eV. The top of the filled bands is called the valence band (E_v) and the bottom of the unfilled bands is called the conduction band (E_c).

There is an intermediate category between metals and insulators called the semiconductor. When the band gap is small, an electron from the valence band can move to conduction band by the absorption of photon of energy equal to the band gap (E_g), or larger. The frequency (ν) of the photon must therefore be:

$$\nu \geq \left(\frac{E_g}{h} \right) \quad \textbf{(Equation 2.5)}$$

Where h is Planck's constant.

As a result E_c becomes partially filled and contributes to conduction (Figure 2.6). Such a material is called a semiconductor, typical examples of which are Si and Ge with band gaps 1 and 0.7 eV respectively. A material with E_g less than 2 eV behaves as a semiconductor at room temperature. A solid with E_g greater than 2 eV behaves as an insulator whereas under illumination from a source with photons greater than band gap, the electrons in the valence band jump to conduction band and the material behaves as a semiconductor (Figure 2.6). There is no clear distinction between an insulator and a semiconductor. It depends on energy gap, temperature and impurity levels of a material.

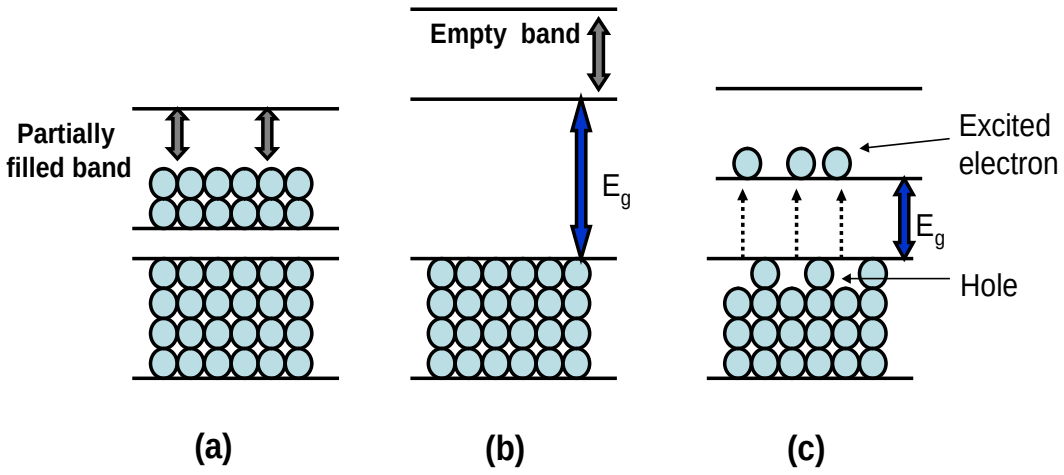

Figure 2.6 Energy level diagram of (a) metal, (b) insulator and (c) semiconductor as a function of bandgap width.

2.2.2 Ferroelectrics as semiconductors

The band gap of ferroelectric perovskites is large e.g. around 3.2–3.7eV[8] for PZT-type materials, and 3.2eV[9] for $BaTiO_3$, and therefore traditionally they are considered as insulators. However according to Scott *et al.*[10] ferroelectric perovskites are also wide band gap semiconductors. This is owing to the large amount of impurities present in perovskites, in addition to this under the influence of sufficiently high energy radiation,

ferroelectric perovskites follow basic semiconductor theory. There has been extensive research on the semiconducting properties of ferroelectric thin films. Boerasu *et al.*[11] studied the semiconducting and ferroelectric properties of PZT thin films by analysing the capacitance-voltage and current-voltage characteristics and found that in certain conditions e.g. application of DC voltage across the metal-PZT-metal structures, semiconducting properties are dominant over the ferroelectric ones. Application of a DC voltage leads to the formation of space charge region (SCR) of size comparable to the thickness of the film, which altered the ferroelectric properties e.g. remnant polarisation of the film. Pintilie *et al.*[12] took this research further and proposed that PZT thin films are wide-gap semiconductors and they form Schottky contacts at the electrode ferroelectric interface. A non-doped PZT possesses naturally occurring acceptor type impurities such as Al^{3+}, Na^{+} and Fe^{3+} resulting in a p-type behaviour of the film[13]. However Mihara et al[14] have also reported an oxygen deficient layer with n-type conductivity at the surface because of the volatilisation of lead oxide from the film composition during the crystallisation annealing of films at high temperatures.

2.2.3 Semiconductor surface

The surface of a semiconductor is different from the bulk due to the break in lattice at the surface. Shockley[15] analysed the chemical bonds on the surface of semiconductor and defined that due to dangling electron bonds some localised energy levels exist on the surface of a crystal. These energy levels can trap electrons and holes producing a surface electric charge and thus inducing a charge of opposite sign in the bulk. The presence of charges in these surface states changes the electric potential at the surface and

consequently the energy level of bands at the surface changes and the bands are bent. Take an example of n-type semiconductor where the surface states have been introduced (E_{ss}). The states are empty and below the Fermi level, and will therefore trap some of the electrons from the conduction band. This will make the surface negatively charged and induce a positive space charge region (SCR) below it. As a result of this, the energy bands at the surface are bent upwards with respect to the Fermi level. Similarly when surface states trap holes, the surface will be positively charged inducing a negative SCR below it and consequently bands will be bent downwards. A diagrammatic representation of energy band bending on the surface of n-type semiconductor and charge distribution in the SCR is shown in Figure 2.7.

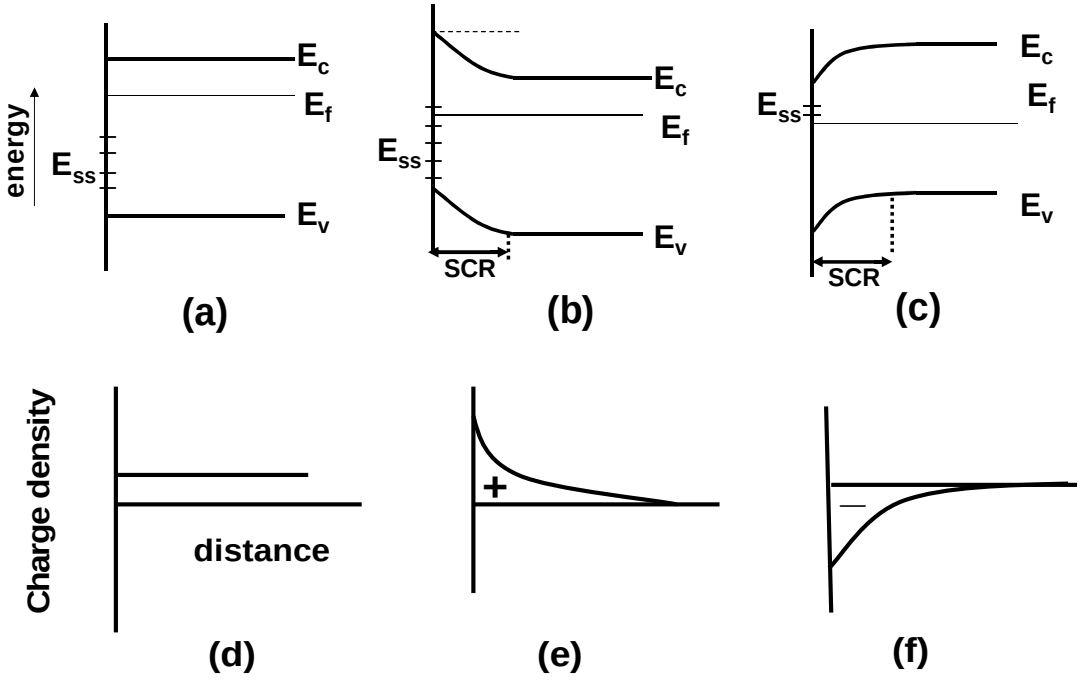

Figure 2.7 Energy diagram and band bending for a n-type semiconductor (a) immediately after the introduction of surface states (d) charge distribution in the SCR (b) upward band bending (e) and charge distribution and (c) downward band bending and (f) charge distribution. SCR denote the space charge region.

As discussed already that ferroelectrics are wide band gap semiconductors, the same technical rules (e.g. band bending at the surface) can be applied to ferroelectrics.

2.3 Ferroelectric surface and energy band bending

On the surface of a ferroelectric the atomic polarisation induces a surface charge (σ) which is:

$$\sigma = \vec{P} \bullet \hat{n} \quad \textbf{(Equation 2.6)}$$

Where σ is surface or polarisation charge, $\vec{P}$ is polarisation vector, $\hat{n}$ is unit vector normal to the surface. This polarisation charge affects surface topography, chemical reactivity[16], optical and electronic properties of ferroelectric surfaces, and is clearly demonstrated by phenomena such as ferroelectric electron emission[17,18], polarisation dependent work function[19] and metal deposition[20, 21]. There are two possible mechanisms for the compensation of induced surface charge. First is surface adsorption of charged molecules from the environment (external screening) and second is compensation of polarisation charge by free charge carriers and defects in the bulk of the material (internal screening). On a surface with positive polarity, the positive polarisation charge is screened by free electrons, negatively ionised acceptors or defects in the bulk and/or adsorption of negative ions from the air (as shown in Figure 2.8). Similarly on the surface with negative polarity, the negative polarisation charge is screened by free holes, positively ionised donors, defects and/or adsorption of positive ions from the atmosphere. Figure 2.8 shows the screening mechanism in PZT and $LiNbO_3$ materials. In PZT films, the concentration of defect states near the surface is high (10^{14} cm^{-2})[10] and therefore the

predominant mechanism of screening is internal whereas in $LiNbO_3$ a low concentration of defects near the surface (10^{12} cm^{-2})[51] leads to predominant external screening.

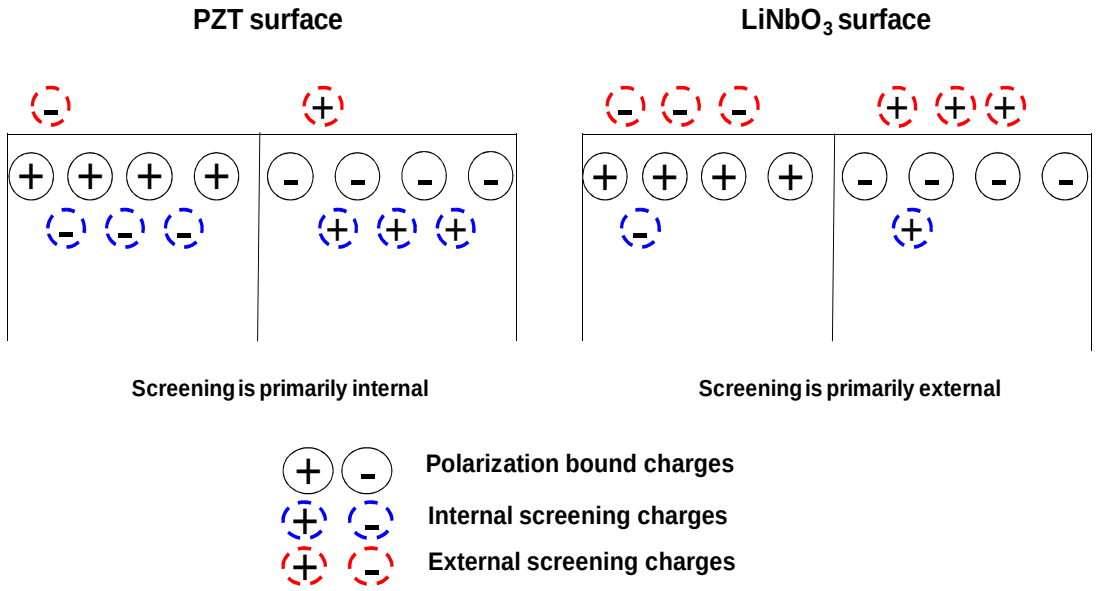

Figure 2.8 A schematic diagram showing surface charges on ferroelectric PZT and $LiNbO_3$

The intrinsic screening gives rise to an internal electric field which causes band bending in the near surface region, resulting in the formation of SCR as shown in Figure 2.9.

The first suggestion about the existence of space charge layer was given by Kanzig[22] on the basis of experiments performed on $BaTiO_3$. It was observed that a strong electric field of 10^4 -10^6 V/cm and a low dielectric constant could be observed in the volume of the surface layer. It was then shown that the surface layer is not a foreign film but is a surface region of the crystal in which dielectric saturation occurs because of strong electric field[23]. Through detailed investigation of properties and nature of the surface layer, Treibwasser [24] modelled it as a Schottky barrier. Recently, Yang *et al.*[19] have verified the presence of band bending on the ferroelectric surface by photoelectron microscopy measurements.

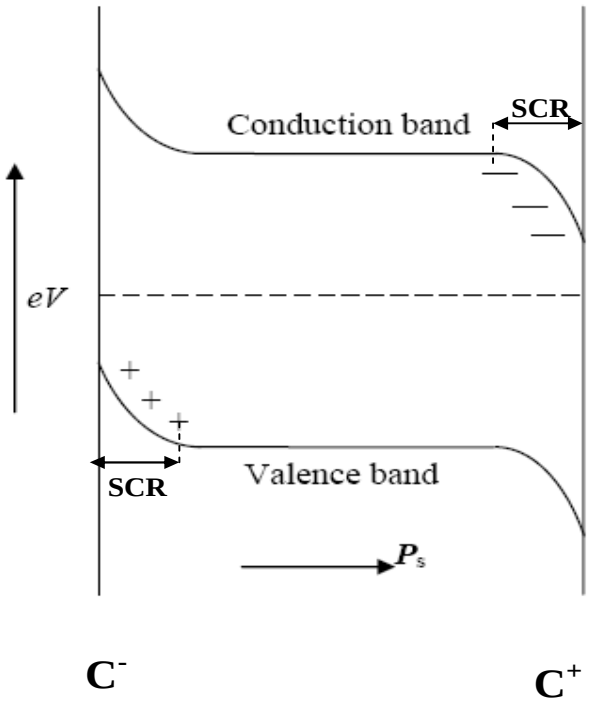

Figure 2.9 Diagram showing bending of energy bands and formation of space charge region (SCR) at the C^+ and C^- domains on the ferroelectric surface. On a C^+ domain the energy bands are bent downwards and on a C^- domain the bands are bent upwards. The arrow represents direction of spontaneous polarisation (P_s).

Surface adsorption on a ferroelectric surface was reported as early as 1958 by the selective deposition of sulphur and PbO on C^- and C^+ domains respectively[25]. Kalinin *et al*. demonstrated the presence of external screening on ferroelectric barium titanate by surface potential measurements[26]. In this case, the sign of surface potential of a domain was opposite to that expected from domain polarity indicating that the polarisation bound charge was completely screened by a charge of opposite sign.

At equilibrium, the polarisation charge (σ_{pol}) is always screened by screening charge (σ_s) of opposite polarity. However, there are four possible situations that can exist on a ferroelectric surface[26]:

1) Completely unscreened surface σ_s=0.

2) Partially screened surface $\sigma_{pol} \geq \sigma_s$.

3) Completely screened surface $\sigma_{pol} = -\sigma_s$.

4) Overscreened surface $\sigma_{pol} \prec -\sigma_s$.

A completely unscreened surface is an unfavourable energy state and can be observed only in vacuum. This is due to the presence of water in all normal circumstances and the associated screening through interactions with the dipoles in the water. Overscreened surfaces may occur and have been observed during bias induced domain switching[27] but are not likely in ambient conditions at equilibrium. In ambient environments such as in air, the ferroelectric surface is partially or completely screened due to the adsorption of water molecules and salts on them. Kalinin *et al.*[26] gave an expression for charge distribution on this type of surface in terms of the uncompensated charge component: $\Delta\sigma = \sigma_{pol} - \sigma_s$.

2.4 Grain boundaries

The term Grain Boundary (GB) can be defined as a plane which separates crystallographically coherent areas in crystalline solids[28]. In ferroelectric materials, the effect of GB is similar in some respects to the surface e.g. if the polarisation in adjacent grain is not parallel then the non-zero divergence of spontaneous polarisation acts as a source for a depolarising field. This depolarising field is compensated by free charge carriers within the bulk leading to the formation of SCR. In semiconducting oxides, the presence of electron and hole traps at interfaces depletes the neighbouring grains of free

electronic carriers leading to the formation of SCR[29]. For n-type semiconducting ceramics, negatively charged GB states are compensated by positively charged donor centres in the bulk close to the grain boundary. This creates a depletion of the negatively charged mobile carriers in a layer of width d_{GB} symmetrically surrounding all grain boundaries, and leads to the formation of depletion layers[30] and upward bending of energy bands. Similarly for p-type semiconductor, downward band bending occurs. Since a GB is surrounded by two grains, Blatter *et al.*[30] modelled it as back-to-back or double Schottky barriers.

Lee *et al.*[31] investigated the effects of grain boundary on the electrical properties of PZT thin films. They found that an area with no grain boundary showed excellent ferroelectric and electrical performance whereas when grain boundaries were included in the measured area severe degradation of polarisation, leakage current, breakdown field and fatigue characteristics was observed. Figure 2.10 shows that both the remnant polarisation and dielectric constant decreased with the increase in length of the grain boundaries. They confirmed that the main source of degradation in PZT thin films is a grain boundary. Kim *et al.*[32] took the research further by investigating the potential distribution on the surface of PZT thin films using Kelvin force microscopy technique. They observed that the GBs have lower surface potential than the area inside the grain and this low potential spreads inside the grain as the elapsed time increases, Figure 2.11.

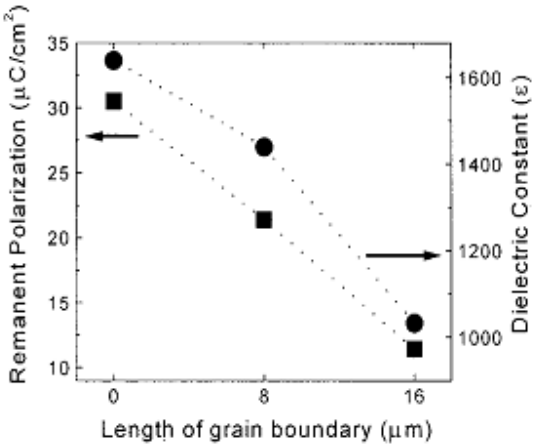

Figure 2.10 Variation of the remnant polarisation and dielectric constant with the length of grain boundaries (Source ref. 31)

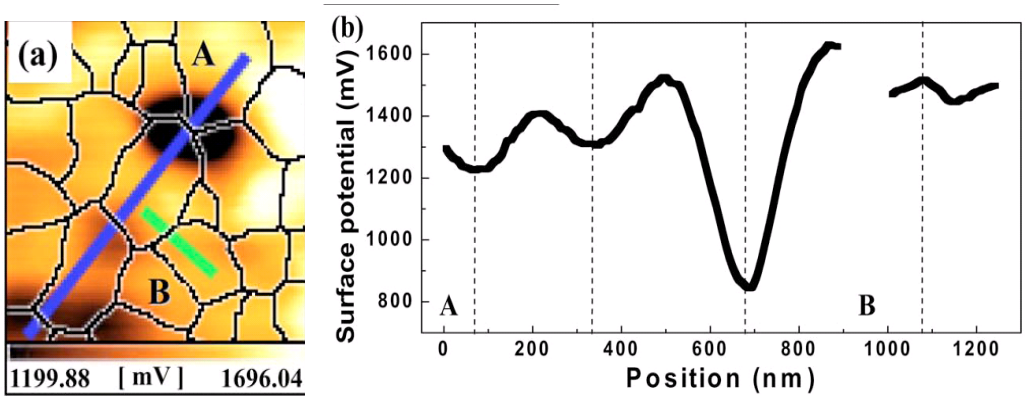

Figure 2.11 (a) Surface potential image of PZT thin film, (b) Surface potential profile obtained from blue line A and green line B. The dotted line shows location of the grain boundaries. (Source ref. 32)

2.5 Double layer

As discussed previously, surface charge on a ferroelectric surface is compensated by two mechanisms, external and internal screening. External screening involves surface adsorption of charged molecules from the environment. In a simple model of the electric double-layer, insertion of a ferroelectric into an ionic solution will attract counter ions from solution to form the electric double-layer. In the mid 18th century, Helmholtz

proposed a model for electric double layer according to which the counter ions bind directly to the surface forming a rigid charge layer called the Helmholtz layer[33]. This Helmholtz layer was limited to thickness of a molecular layer. In 1917, Gouy and Chapman took this research further and proposed a model for diffuse double-layer[33]. They suggested that thermal motion of ions in solution drives the counterions away from the surface leading to a formation of a diffuse layer. Later on, in 1924 Otto Stern[34] put forward a new model for double layer that was a combination of Helmholtz and Gouy-Chapman theories. According to this new theory, the double layer comprises of two parts. First is an inner part, the Stern layer, which is immobile and consists of a layer of tightly bound ions adsorbed to the surface. Secondly an outer part, the diffuse layer also called Gouy-Chapman layer that consists of mobile ions. The potential at the point where Stern layer ends and diffuse layer begins is called zeta potential (ψ_δ). A simple model of Stern layer is shown in Figure 2.12.

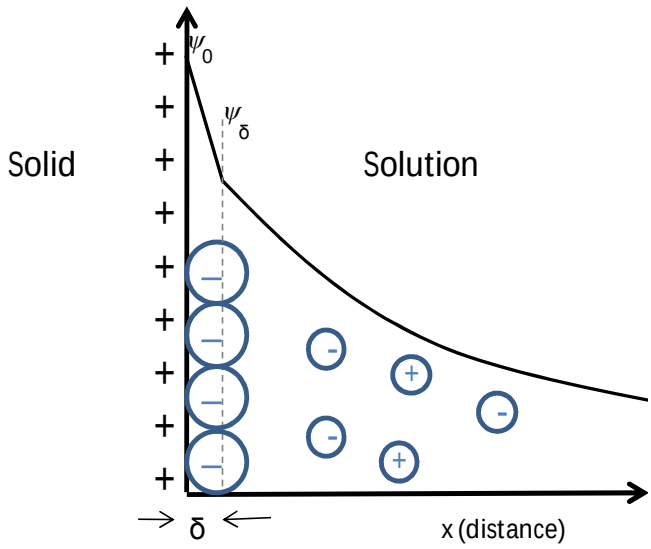

Figure 2.12 A simple model of Stern layer where ψ_0 is potential at the surface of solid and ψ_δ is zeta potential (Source ref. 33).

The positive charge on the solid surface is compensated by negatively charged counterions in the solution; the distance (δ) between the surface and the centres of these counterions marks the Helmholtz plane that separates Stern layer from the Gouy-Chapman layer. In diffuse layer the potential change with respect to charge distribution is given by Poisson-Boltzmann equation as shown in Equation 2.7.

$$\nabla^2\psi = \frac{c_0 e}{\varepsilon\varepsilon_0}\left(e^{\frac{e\psi(x,y,z)}{k_B T}} - e^{-\frac{e\psi(x,y,z)}{k_B T}} \right) \quad \textbf{(Equation 2.7)}$$

Where ψ is potential at a point in solution, c_0 is bulk concentration of ions in the solution, k_B is Boltzmann constant, T is temperature and $\varepsilon, \varepsilon_0$ are relative and vacuum permittivity respectively. The potential decreases exponentially from the ferroelectric surface into solution and the decay length is called the Debye length (λ_D) which is given by Equation 2.8.

$$\lambda_D = \sqrt{\frac{\varepsilon\varepsilon_0 k_B T}{2c_0 e^2}} \quad \textbf{(Equation 2.8)}$$

The Debye length is dependent on the concentration of ions in the solution. The concentration of ions at the surface is large due to the oppositely charged ions attached to it, and therefore the potential decreases rapidly in the Stern layer and then it decreases exponentially in the diffuse or Gouy-Chapman layer.

2.6 Photochemistry at semiconductor-solution interface

In order to understand the photochemistry at a ferroelectric-solution interface, it is necessary to provide a short review of photochemistry on the surface of a semiconductor. The studies on photoelectric or photochemical properties of semiconducting materials

were reported as early as 1929 when Kiedel *et al.*[35] reported that paint containing particles of TiO_2 blistered or discoloured under sunlight. This was then followed by Goodeve and Kitchener's work in 1938 that showed the wavelength dependence of photoactivity of TiO_2[36] and Mashio *et al*. publishing a paper that showed the photoxidation performance of TiO_2[37]. During the oil crisis in the late 1960's and early 1970's, a number of groups picked up on the photostability of semiconductors as a possible means of generating useful energy, either in the form of an electric current or chemical energy. In 1972, Fujishama and Honda[38] showed the use of semiconducting n-type TiO_2 for the decomposition of water using only UV light as the energy input.

When a semiconductor surface is illuminated with light containing photons with energy greater than the bandgap of the material, photoexcited charge carriers called electron-hole pairs are generated in the material[39]. This happens because the incident photon will excite an electron from the valence band to the conduction band leaving a hole behind. These charge carriers are separated by the electric field present in the SCR[40], typically in $< 10^{-12}$ s. On a n-type semiconductor, when the bands are bent upwards as shown in Figure 2.13, upward band bending creates a barrier for the photoexcited electrons to reach the surface. The field in the SCR drives electrons towards the bulk of the semiconductor whereas the photoexcited holes are driven towards the surface, where they can take part in a chemical reaction. When the bands are bent downwards as shown in Figure 2.13, the field in the SCR drives photogenerated holes towards the bulk and the electrons are driven towards the surface where they can take part in a chemical reaction. A surface with electrons is reductive in nature and a surface with holes is oxidative. Band

bending and oxidative/reductive nature of a semiconductor surface is shown in Figure 2.13.

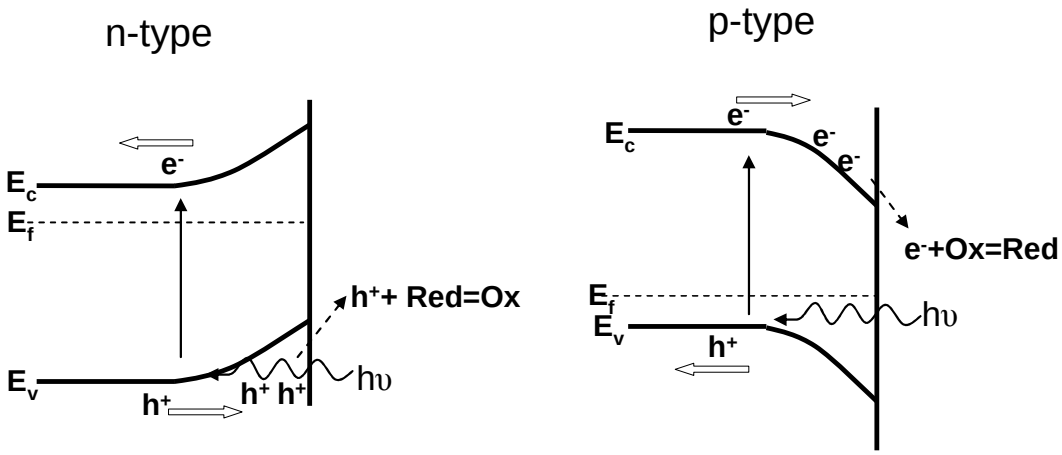

Figure 2.13 Schematic diagram showing band bending in n-type and p-type semiconductors and preferably oxidative and reductive surface respectively. 'Red' and 'Ox' are reduced and oxidised species in solution respectively and h^+ and e^- are holes and electrons respectively.

2.7 Photochemistry at ferroelectric-solution interface

On a ferroelectric surface, the photogenerated charge carriers are driven by the internal depolarisation field resulting in a restructuring of valence and conduction band at the surface[41]. The energy band diagrams of C^- and C^+ surface of a ferroelectric are shown in Figure 2.14.

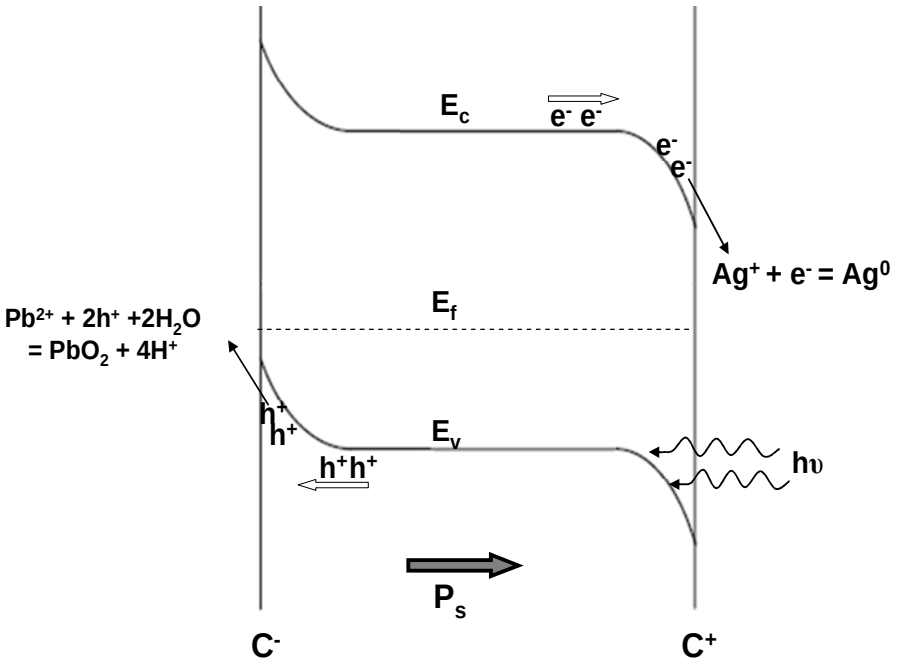

Figure 2.14 Schematic diagram of photoexcited electrons and holes separation on the C^- and C^+ surface of a ferroelectric. Availability of holes on C^- surface makes it oxidative and availability of electrons on C^+ surface makes it reductive. The arrow (P_s) represents the direction of spontaneous polarisation.

Shao *et al.*[42] have proved that photogenerated electron hole pairs contribute to internal screening of polarisation charge by reporting a significant decrease in the surface potential contrast between C^+ and C^- domains in $BaTiO_3$ in the presence of UV light illumination as shown in Figure 2.15; the surface potential recovers after the UV light is switched off.

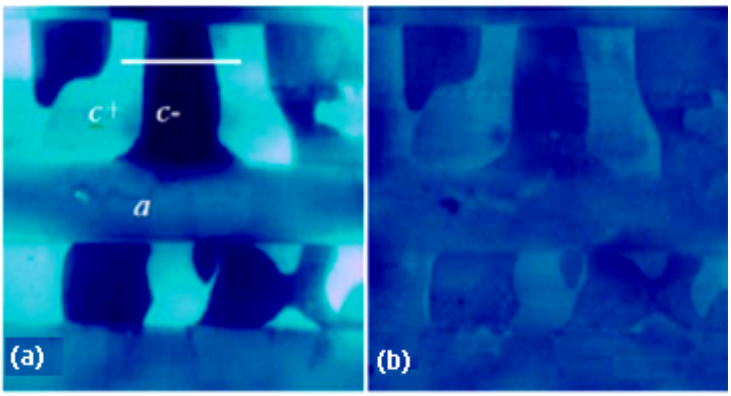

Figure 2.15 (a) The surface potential image of 'a' and 'c' domains with curved domain walls (b) the surface potential image when the UV light is on (Source ref. 42)

The photochemistry of ferroelectric $BaTiO_3$ was first reported in a paper by Nasby and Quinn[43], who showed a pH dependence on flat band potential and that $BaTiO_3$ shows good photostability and photocurrents. In 2000, Giocondi and Rohrer[44] published a paper highlighting the variation in surface photochemistry for $BaTiO_3$. They showed that it was possible to spatially separate photochemical oxidation and reduction reactions on the surface of a ferroelectric material. They demonstrated that in a C^+ domain, due to the availability of photogenerated electrons at the surface, the silver cations from the silver nitrate solution photoreduce to silver metal and in C^- domains where holes are driven to the surface oxidation of lead salts produced PbO_2, as shown in Figure 2.14.

$$Ag^+ + e^- \rightarrow Ag^0$$ **(Equation 2.9)**

$$Pb^{2+} + 2H_2O + 2h^+ \rightarrow PbO_2 + 4H^+$$ **(Equation 2.10)**

This was the first time a relationship between band bending and the domain polarisation of the ferroelectric was established. In 2001, Kalinin *et al.*[45] reported a novel technique called 'ferroelectric lithography' that used the photoreduction reaction to produce metal nanoparticles in predefined locations on the surface of ferroelectric material as shown in

Figure 2.16. Later, Dunn *et al.*[46] showed that it is possible to selectively absorb biological molecules onto the surface of a ferroelectric.

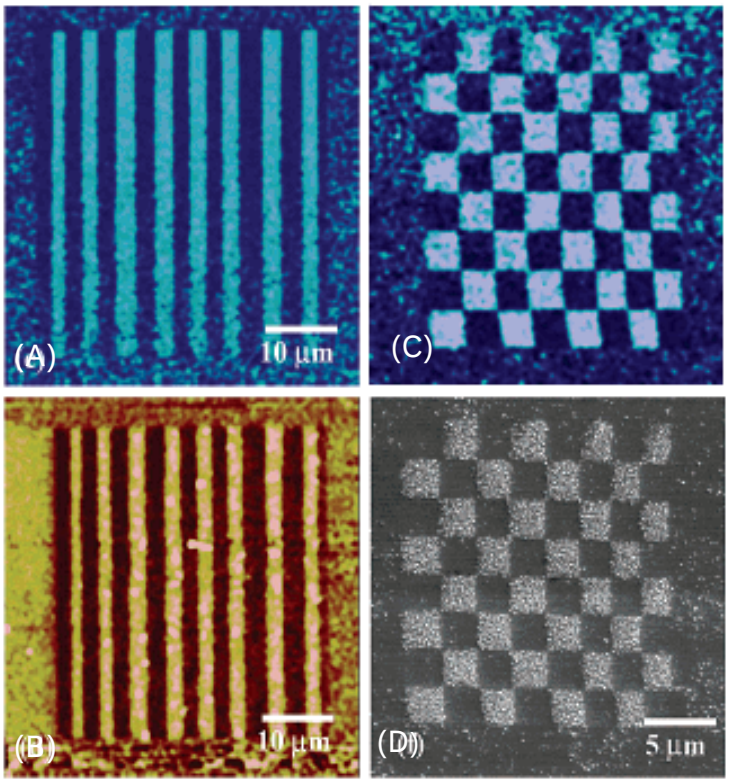

Figure 2.16 PFM image of lines patterned with alternating +10 and -10 V_{dc} (A). Bright areas are positive domains and dark areas are negative domains. An image of the surface topography (B) after deposition of Ag nanoparticles. Note that the metal has deposited only on the positive domains. PFM image of checkerboard domain structure (C) and SEM image of corresponding silver photodeposition pattern (D). (Source Ref. 45)

The development of ferroelectric lithography can be considered as a combination of two phenomena:

1- Controlling the local domain structure in ferroelectric material, through patterning with Piezo Force Microscopy (PFM)[47,48] or electron beam systems[20].

2- Using the photooxidation/photoreduction reactions to direct the assembly of nanoparticles on selected regions of the ferroelectric surface.

Deposition of inert metals e.g. Au, Pd[45], Rh, Pt[21], transition metals e.g. Co, Ni, Fe[49] and multi-elements photodeposition have been demonstrated. Ferroelectric lithography can be utilised to attach molecules with special electrical or optical properties on the surface of a ferroelectric material to form some complex nanostructures[16]. In 2007, Bonnell *et al.*[50] demonstrated ferroelectric lithography on an organic substrate Poly (vinylidene fluoride). In 2006, Hanson *et al.*[51] developed a method for the fabrication of silver nanowires on domain patterned single crystal $LiNbO_3$ where preferential deposition of silver occurred along the 180° domain walls, as shown in Figure 2.17. The selective deposition process was attributed to the combination of non-uniform electric field in the vicinity of the domain wall and the predominant external screening due to the low density of defect states at the surface[52].

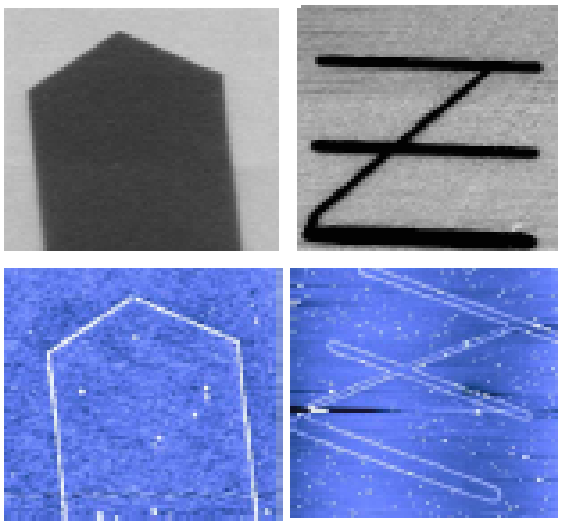

Figure 2.17 PFM images of domain patterns generated in $LiNbO_3$ sample (top), corresponding topographic images of silver nanowires (bottom) (Source ref. 51)

In 2007, Liu *et al.*[53] demonstrated silver nanoparticle deposition on entire C^+ domain of $LiNbO_3$ by a mechanism described as photovoltaic effect as shown in Figure 2.18 (a). Continuous supply of photogenerated electrons to the ferroelectric surface was

emphasised in their work and this was achieved by polishing the samples down to thickness of 800 nm and depositing a back electrode on the sample. Apart from sample thickness photovoltaic effect was also found to be dependent on the intensity of incident UV light.

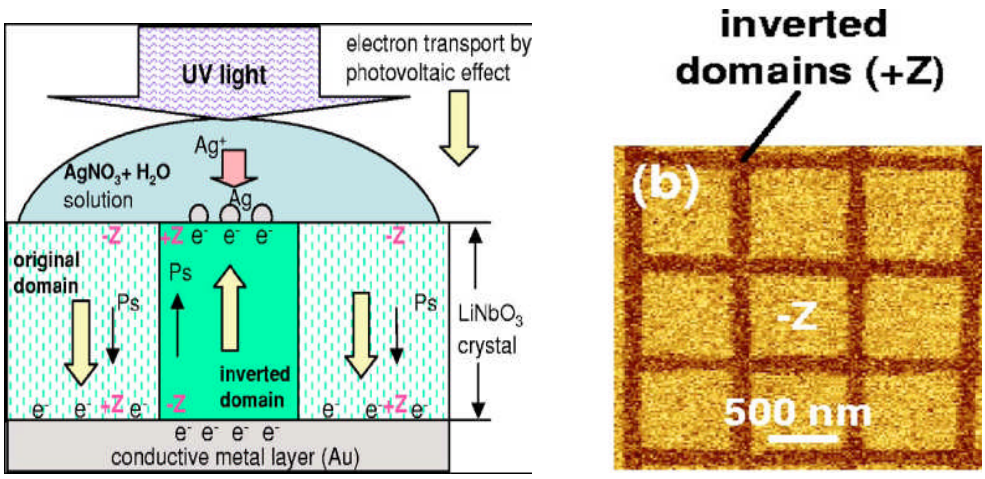

Figure 2.18 (a) Mechanism of selective Ag deposition on the C^+ surfaces of inverted domain patterns. The photovoltaic effect causes photoexcited electrons to move preferentially in the C^+ direction; at the surface they combine with Ag^+ ions in the solution and deposit Ag there. (b) Tapping mode-AFM images of Ag particles deposited on the C^+ surfaces of LN crystals. Ag^+ is not reduced at the C^- surface because of the absence of free electrons. (Source ref 53)

In 2007 Jones *et al.*[54] showed that the deposition of Ag on polycrystalline PZT is also related to the surface defects such as grain boundaries (GB) within the film. The greatest deposition rates were found to occur at GB on the surface. At GBs there exists a local electric field that influences the photochemistry of the surface, Figure 2.19 (left). A combination of band bending at the grain boundaries and a space charge region, causes electron movement towards it creating higher availability of electrons for metal reduction and therefore greater deposition of Ag, Figure 2.19 (right).

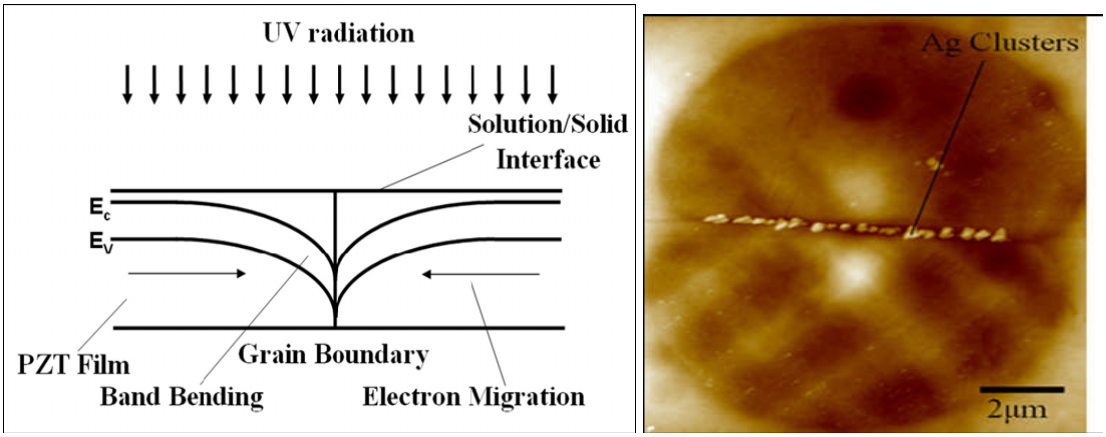

Figure 2.19 Electric field caused by the downward band bending at the grain boundary causes photogenerated electron flow towards it (left), photoreduced silver at grain boundary (right) (Source ref. 54)

In 2005, Lei *et al.*[49] showed dependence of the metal cluster growth on PZT surface on the wavelength of irradiated light and the time of irradiation by comparing the deposited particle size and density, as shown in Figure 2.20. The average size and density of silver particles increased when the time of irradiation increased from 5 minutes to 45 minutes. The size and density of metal particles also increased as the energy of UV light is increased from 3.64eV (340 nm) to 4.13 eV (300 nm) with maxima at 4.13eV. Recent work by Jones *et al.*[55] also shows an increase in cross sectional area and surface density of Ag clusters with an increase in photon energy; deposition started at 4eV and stopped at 5.06eV. The difference between Lei and Jones's work can be due to the difference in measurement techniques. In Lei's work, with the increase in time of irradiation, particle size exhibits monotonic increases of size by a factor of 3 and of density by a factor of 6 over 60 min. Lei's work also determined the dependence of concentration of solution on deposited clusters and found that higher concentration yielded larger particle size and higher density.

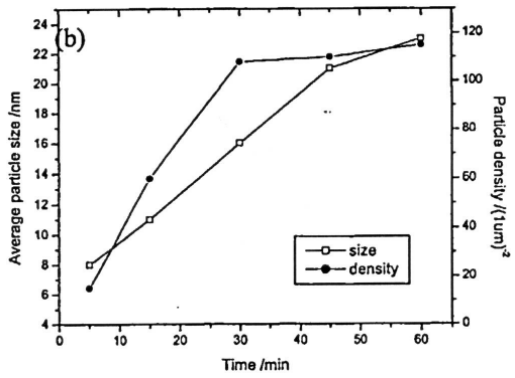

Figure 2.20 Density of the deposited Ag particles and average particle size with respect to irradiation time (Source ref. 49)

A growing theme of work is now to investigate the influence of surface polarisation on chemical adsorption[56,57] and physical adsorption on the ferroelectric surface[58].

Ferroelectric lithography bears a huge potential for assembling and testing functional nanoelectronic devices. Haussmann *et al.*[59] were the first to show electrical performance of single metallic nanowire assembled by ferroelectric lithography by measuring the conductivity of a Pt nanowire and imaging potentiostatic information with sub-micrometer resolution.

2.8 Photovoltaic effect

When a ferroelectric material is illuminated with light of certain photon energies, photo induced charge carriers are created and separated by internal electric field leading to the development of a photovoltage[2]. Such photovoltaic phenomenon in ferroelectric barium titanate crystal was first observed by Chynoweth in 1956[60] and in lithium niobate by Chen in 1969[61]. Weak but steady photocurrents were recorded in each case when under illumination with no external bias. In 1974, Glass *et al.*[62] developed a relationship

between photovoltaic current density J and intensity of incident light (I) given by equation:

$$J = K\alpha I \quad \textbf{(Equation 2.11)}$$

where α is the optical absorption coefficient of the material at a wavelength and K is a constant. Brody later reported greater-than-band-gap photovoltages of several hundred volts per centimetre in poled ceramic $BaTiO_3$ + 5 wt.% $CaTiO_3$, $Pb(Zr_{0.65}, Ti_{0.35})O_3$ and other ferroelectric ceramics [63] which were shown to be linearly proportional to both the sample length and the remnant polarisation and were observed only below the Curie temperature. Ionue *et al.*[64] recorded photovoltages three times larger than the bandgap for Lead Strontium Zirconate Titanate with directed polarisation fields in opposite directions to the photocurrent.

Over the years, there has been some extensive research into factors that may affect photovoltaic output. Kholkin *et al.* studied photocurrents in PZT thin films and found that at low electric fields the photocurrent was sensitive to the ferroelelctric polarisation state[65]. The direction and peak values of photocurrent reflected the polarisation state of the PZT film as shown in Figure 2.21. Kholkin *et al.* further investigated the effect of illumination on ferroelectric properties of PZT thin films and found that piezoelectric coefficient, dielectric permittivity and remnant polarisation decrease under UV illumination[66]. The dependence of photoinduced current on PZT film thickness has been investigated by Qin *et al.* It is found that the photocurrent increases exponentially with the decrease in film thickness and maximum photocurrent is detected in the film of thickness 50-90 nm[67].

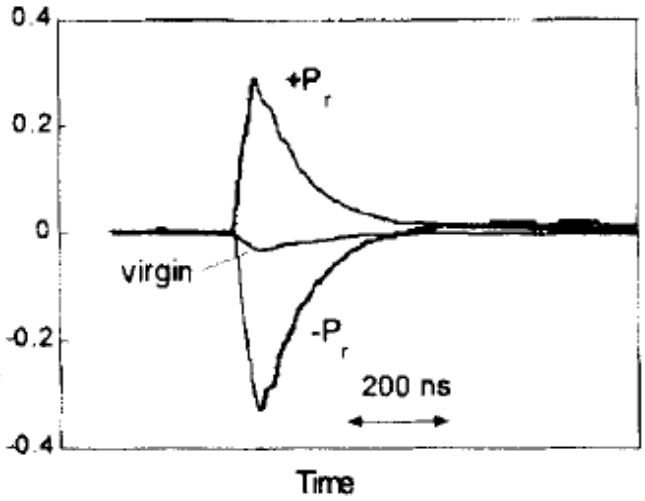

Figure 2.21 Transient photocurrent in PZT (45/55) **film illuminated by *UV* laser pulses *(h=350* nm). The polarisation state of the films is indicated in the Figure. (Source ref. 65)**

2.9 Lead zirconate titanate (PZT)

2.9.1 Phase diagram

The bulk phase diagram of PZT is shown in Figure 2.22.

Above the curie temperature (T_c), the cubic paraelectric phase is stable and the material is non-ferroelectric and upon cooling below the curie temperature the material is ferroelectric. For Ti rich compositions $(0 \le x \le .52)$ the movement of Ti/Zr atom in oxygen octahedra in [001] direction gives rise to tetragonal distortion of unit cell whereas for compositions with lower Ti content $(.52 \le x \le .94)$ the movement of Ti/Zr atom in [111] direction gives rise to rhombohedral distortion in unit cells as shown in Figure 2.23. At x=0.48, a morphotropic phase boundary exists that separates the tetragonal and rhombohedral phase; compositions above x=.94 are antiferroelectric in nature.

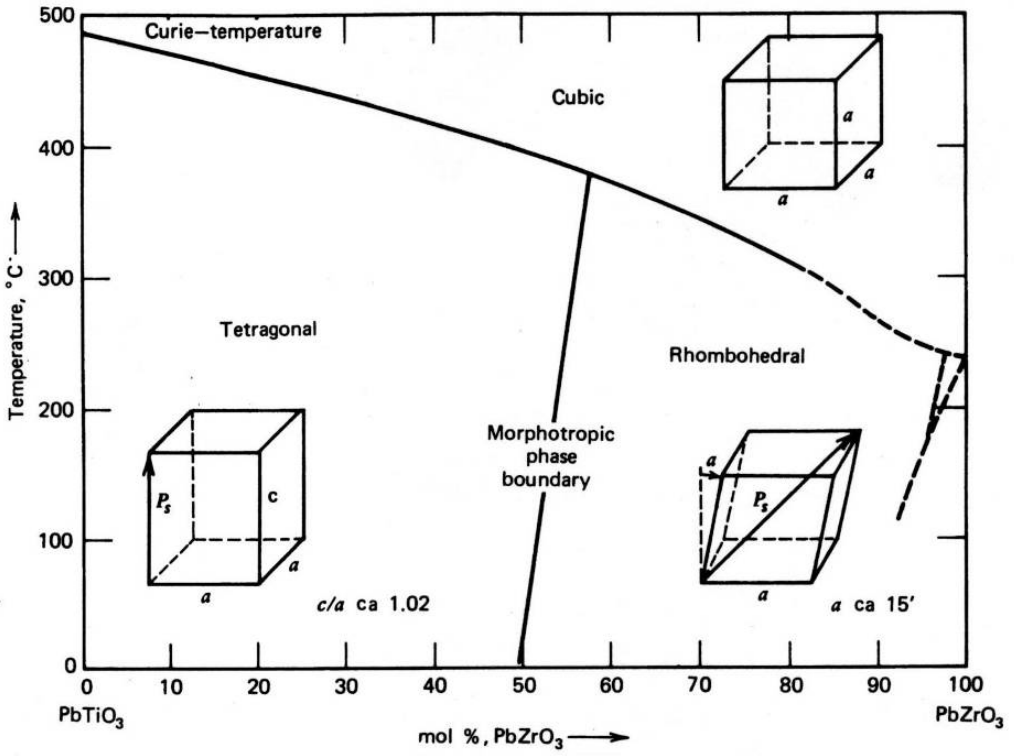

Figure 2.22 The bulk phase diagram of PZT (Source ref. 68)

The compositions used in this research are $PbZr_{0.3}Ti_{0.7}O_3$, $PbZr_{0.52}Ti_{0.48}O_3$ and $PbZr_{0.7}Ti_{0.3}O_3$; the crystallographic structure at room temperature according to bulk phase diagram is tetragonal, coexistence of tetragonal and rhombohedral, and rhombohedral respectively. The polarisation directions in tetragonal PZT lie along the [001] directions with total of 6 equivalent directions passing through each vertex of the oxygen octahedral. In the rhombohedral PZT, the polarisation directions lie along the [111] direction with the total of 8 possible directions passing through the centre of each octahedral phase.

For $T \geq T_c$

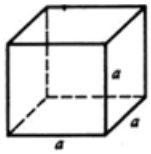

For $T \prec T_c$

For ($0 \leq x \leq .52$) Tetragonal phase

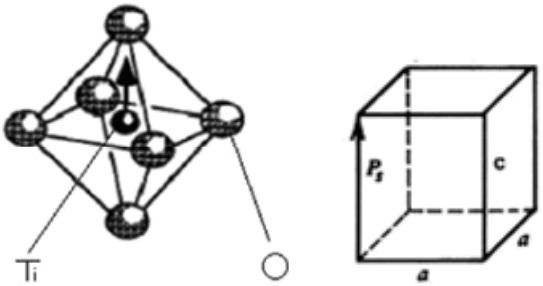

For ($.52 \leq x \leq .94$) Rhombohedral phase

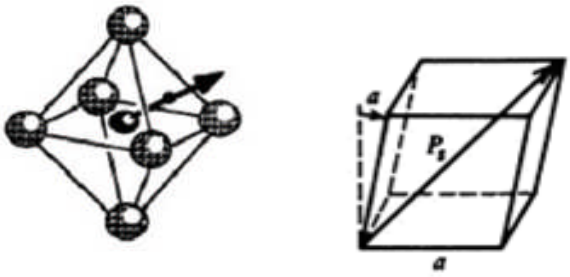

Figure 2.23 Above Curie temperature (T_c) PZT exists in cubic phase and below T_c in tetragonal/rhombohedral phase.

2.9.2 Piezoelectric properties

PZT compositions have substantially higher polarisation than many other ferroelectric materials e.g. $BaTiO_3$. Owing to its high Curie temperature ranging from 250-480º C for various compositions (as compared to 120º C for $BaTiO_3$), the piezoelectric properties are relatively stable over a wider temperature range. According to Jaffe *et al.*[69], compositions close to the morphotropic phase boundary exhibit strong piezoelectric effects because of the increased ease of reorientation during poling. Investigations of piezoelectric

properties of the lead zirconate titanate system show that the electromechanical coupling factor and dielectric constant are highest near the morphotropic phase boundary[70].

2.9.3 Defects

Ferroelectric thin films e.g. PZT show great promise as dynamic and nonvolatile random access memories in microcircuits[71]. In order to obtain a material that can survive applications of the high electric field required for fast switching, understanding the defect chemistry is of paramount importance. Long and Blumenthal[72] were the first to suggest that undoped perovskite titanates have naturally occurring acceptor impurities (cations usually possessing less positive charge than the host cation) e.g. Al^{3+}, Na^{+} and Fe^{3+}, and their concentration are sufficient to dominate the defect chemistry. The integration of the acceptor oxide A_2O_3 in $BaTiO_3$ is written as following reaction[73]:

$$A_2O_3 + 2BaO \rightarrow 2Ba_{Ba} + 2A'_{Ti} + 5O_o + \ddot{V}_o \qquad \textbf{(Equation 2.12)}$$

The above reaction uses the Kroger-Vink notation, the subscript indicates the lattice site occupied by the ion or defect, V is a vacancy, and the superscripts show the charge difference, (´) implies a negative charge and (·) implies a positive charge. Equation 2.12 implies that acceptor impurities are included in the lattice by creating oxygen vacancies. In the case of PZT, the defect scenario is complex due to the presence of two volatile components Pb and O. During crystallisation annealing at high temperatures, PbO volatilises from the film leading to the creation of lead and oxygen vacancies. The defect structure of PZT is discussed in detail in Chapter 4.

2.10 Lithium niobate

Ferroelectric properties in lithium niobate were first discovered by B. Matthias and J. Remeika in 1949[74]. Recently lithium niobate (LN) has been an object of intensive research because of its unique properties; it possesses one of the largest magnitude of spontaneous polarisation, which has a value of $78 \pm 3 \mu C/cm^{-2}$ at room temperature[75] and a high Curie temperature of 1140 ºC. As we have already discussed in previous sections, a polarisation induced surface charge needs to be compensated by internal/external screening. Defects contribute to internal screening and the low concentration of defect states near the LN surface[51] (10^{12} cm^{-2} compared to 10^{14} cm^{-2} for PZT) leads to weak internal screening and therefore the predominant mechanism of screening is external. As a result of weak internal screening, the band bending associated with it (and the space charge region SCR) occurs over a larger length scale as compared to other ferroelectric materials such as PZT which have higher concentration of defects near the surface.

2.10.1 Crystal structure

LN is classified as oxygen octahedral ferroelectrics and has a general formula ABO_3. When cooled below the Curie temperature, Li and Nb cations get displayed along the 'c' axis resulting in the formation of a permanent electric dipole moment also known as the spontaneous polarisation. The displacement of Li and Nb cations is restricted to c axis only and therefore only antiparallel domains can form in LN crystals. The room temperature structure of LN is shown in Figure 2.24. Looking along the c axis inside the oxygen cages, the cations are positioned in the order Nb, vacancy, Li, Nb, vacancy, Li,

Nb…[76] (Figure 2.24); Li atoms move into their nearest oxygen planes and Nb atoms are midway between adjacent oxygen planes.

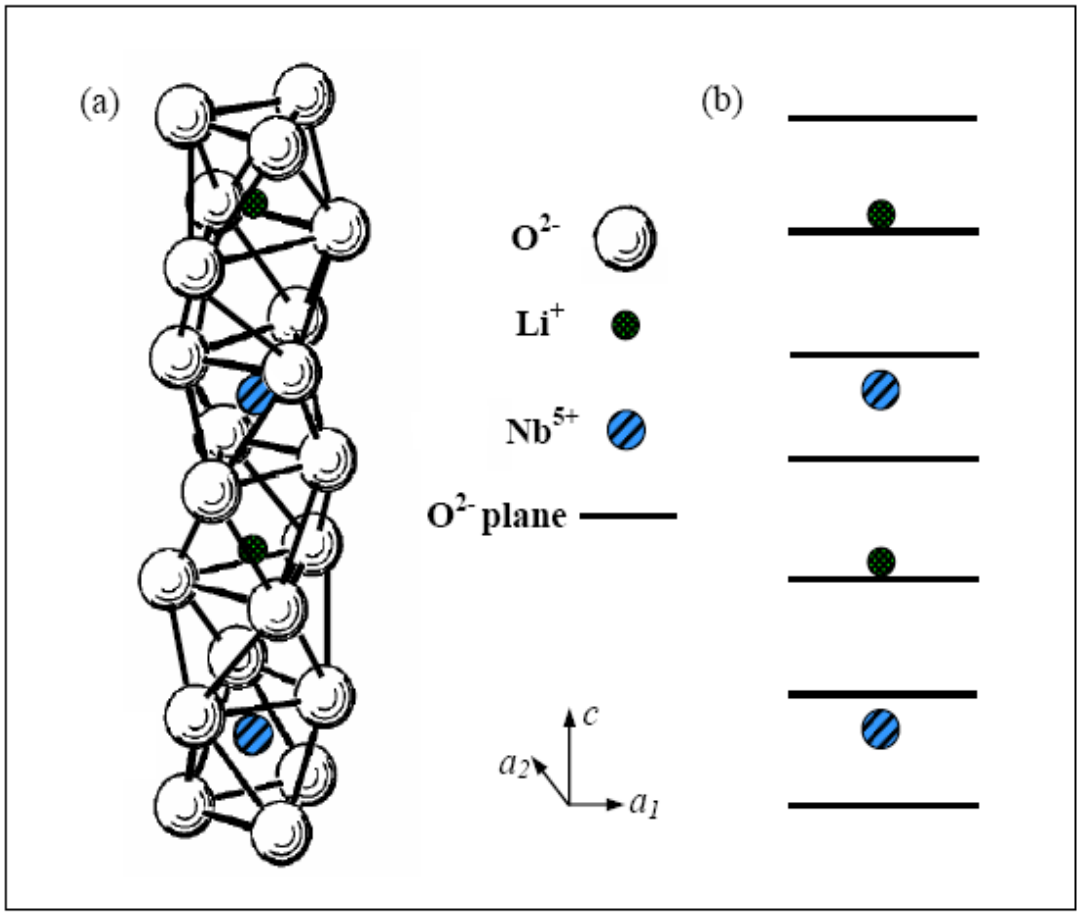

Figure 2.24 Diagram showing (a) crystallographic structure of $LiNbO_3$ and (b) relative positions of ions in $LiNbO_3$ (Source ref. 77)

2.11 Aim and Objectives

As the literature review has demonstrated, in order to control the photochemical deposition process on the surface of ferroelectric materials, the mechanism by which they occur must be thoroughly understood. This knowledge will lead to the feasibility of the process being used as a synthesis tool for functional complex nanostructures and

fabrication of microelectronic circuits and devices. The aim of this research was therefore to investigate the influence of surface characteristics on photochemical reactivity of the ferroelectric material mainly PZT and LN, focusing on the nature and reasons behind the preferential growth of metal nanoparticles. The first part of this research focussed on the photochemical deposition processes occurring on the surface of polycrystalline PZT thin films whereas the second part focussed on single crystal LN surface. The main objectives of this research were as follows:

- Understand the mechanism for the growth of nanoclusters on PZT surface. What are the reasons behind the formation of metal clusters and what are the factors affecting size of metal clusters? Investigate the impact of composition of PZT (Zr/Ti ratio) and the defect concentration in the PZT on its photochemical properties. In addition to this, growth of metal clusters with respect to the size of poled pattern and size of ferroelectric structure was investigated.
- Understand the photoreduction of metal salts on LN surface. Investigate the impact of incident photon energy and intensity on the growth of metal clusters. Accomplish photoreduction of other metals e.g. Al and Mn on LN surface and produce a novel technique for the production of Al nanoparticles. Investigate the impact of doping level of LN on its photochemical properties.

References

[1] P. Curie, J. Curie, *Bull. Soc. Min. de France,* 3, p.90 (1880)

[2] M. E. Lines, and A. M. Glass (eds.), *Principles and Applications of Ferroelectric and Related Material,* Clarendon Press, Oxford (1977)

[3] F. Jona and G. Shirane, *Ferroelectric Crystals,* Dover Publications, New York (1993)

[4] J. Valasek, *Phys. Rev*., 15, 537 (1920)

[5] E. Fatuzzo and W. J. Merz, *Ferroelectricity,* Wiley, New York (1967).

[6] L.M. Eng, *Nanotechnology*, 10, 405-411 (1999)

[7] V M Fridkin, *Ferroelectric Semiconductors*, New York Consultants Bureau (1980)

[8] I. Boerasu, M. I. Vasilevskiy, M. Pereira, M. F. Costa, and M. J. M.Gomes, *Ferroelectrics,* 268, 187 (2002)

[9] W. Heywang, *J. Mat. Sci.,* 6, Number 9, 1214-1224 (1971)

[10] J. F. Scott, *Ferroelectric Memories*, Springer, New York (2000)

[11] I. Boerasu, L. Pintilie, M. Pereira, M. I. Vasilevskyi, M. J. M. Gomes, *J. Appl. Phys.* 93, 4776 (2003)

[12] L. Pintilie, M. Lisca, M. Alexe, *Integ. Ferro.,* 73, 37-48, (2005)

[13] D. J. Wouters, G. J. Willems and H. E. Maes, *Microel. Eng.,* 29, no. 1-4, pp. 249-256(1995)

[14] T. Mihara, H. Watanabe, H. Yoshimori, *Integ. Ferro.,* 1, 269, (1992)

[15] W Shockley, *Phys. Rev*., 56, 317 (1939)

[16] D. Li and D. A. Bonnell, *Ceram. Int.,* 34, Issue 1, Pages 157-164 (2008)

[17] H. Riege, I. Boscolo, J. Handerek, and U. Herleb, *J. Appl. Phys*. 84, 1602–17 (1998)

[18] D. Shur and G. Rosenman, *J. Appl. Phys*. 80, 3445–50 (1996).

[19] W.C. Yang, B. J. Rodriguez, A. Gruverman, and R. J. Nemanich, *J. Phys.: Condens. Matter.*, 17, S1415-S1426 (2005)

[20] D.B. Li, D.R. Strachan, J.H. Ferris, D.A. Bonnell, *J. Mat. Res.*, 21, No. 4, 935 (2006)

[21] S. V. Kalinin, D. A. Bonnell, T. Alvarez, X. Lei, Z. Hu, R. Shao and J. H. Ferris, *Adv. Mater.*, 16, 795–9 (2004)

[22] W. Kanzig, *Phys. Rev*., 98, 549, (1955)

[23] W. J. Merz, *J. Appl. Phys*., 27,938 (1956)

[24] S. Treibwaser, *Phys. Rev*., 118, 100, (1960)

[25] G.L. Pearson and W.L. Feldmann, *J. Phys. Chem. Solids*, 9, 28 (1958)

[26] S. V. Kalinin, D. Bonnell, *Phys. Rev. B* 63, 125411 (2001)

[27] T.Tybell, C. H. Ahn, L. Antognazza and J. M. Trisconne, *Vide: Sci. Tech. Appl*. 289, 551 (1998)

[28] R. Waser and R. Hagenbeck, *Acta Mater.*, 48 797-825 (2000)

[29] R. Krol and H. L. Tuller, *Solid state ionics*, 150, 167-169 (2002)

[30] G. Blatter and F. Grueter, *Phys. Rev., B* 33, 3952 (1986)

[31] J. S. Lee and S. K. Joo, *Appl. Phys. Lett.*, 81, 14, 2602-2604 (2002)

[32] Y. Kim, S. Bühlmann, J. Kim, M. Park, K. No, Y. K. Kim and Hong, S. *Appl. Phys. Lett.*, 91, no. 5, pp. 052906-052909 (2007)

[33] H. J. Butt, K. Graf, M. Kappl, *Physics and chemistry of interfaces*, Chapter 4, Wiley-VCH Verlag GmbH & Co. KGaA, Weinheim (2006)

[34] O. Stern, *Zeitschrift fur Elektrochemie*, 30, 508 (1924)

[35] E. Keidel, *Farben-Zeitung* 34, 1242-1243 (1929)

[36] C. F. Goodeve and J. A. Kitchener, *Trans. Farrady Soc*., 34, 902 (1938)

[37] F. Mashio *et al, Abtr. Book Annu. Meet Chem. Society Japan*, p 223 (1956)

[38] H. Fujishima and K. Honda, *Nature*, 238, 37-38, (1972)

[39] T. Markvart , *How Solar cells work, in Solar cells* 2nd edition , John Wiley and sons, Chichester, 29-34 (2000)

[40] Y. V. Pleskov, Y. Y. Gurevich, *Semiconductor photoelectrochemistry*, Chapter 7 ,1st ed, Consultants Bureau, New York (1986)

[41] S. Dunn, P. M. Jones and D. E. Gallardo, *J. App. Chem. Soc.*, 129, 8724 (2007)

[42] R. Shao, M. P. Nikiforov and D. Bonnell, *Appl. Phys. Lett.*, 89, 112904 (2006)

[43] R. D. Nasby and R. K. Quinn, *Mat. Res. Bull.*, 11, 985 (1976)

[44] G. L. Giocondi and G. S. Rohrer, *Chem. Mater*., 13, 241 (2001)

[45] S.V. Kalinin, D. A. Bonnell, T. Alvarez, X. Lei, J. H. Ferris, S. Dunn and Q. Zhang, *Nanoletters* 2, 589 (2002)

[46] S. Dunn, D. Cullen, E. Garcia, C. Bertoni, R. Carter, D. Howorth and R. W. Whatmore *App. Phys. Lett*., 85, 3537-9, (2004)

[47] S. V. Kalinin and D. A. Bonnell, *Phys. Rev. B*, 65, 125408, (2002)

[48] S. Dunn, C. P. Shaw, Z. Huang and R. W. Whatmore, *Nanotechnology*, 13, 456 (2002)

[49] X. Lei, D. Li, R. Shao and D.A. Bonnell, *J. Mater. Res*., 20, 712, (2005)

[50] C. Rankin, C. H. Chou, D. Conklin, D. A. Bonnell, *ACS Nano*, 1, p. 234 (2007)

[51] J. N. Hanson, B. J. Rodriguez, R. J. Nemanich and A. Gruverman, *Nanotechnology*, 17, 4946-9, 10/14 (2006)

[52] W. C. Yang, B. J. Rodriguez, A. Gruverman, and R. J. Nemanich, *Appl. Phys. Lett.*, 85, 2316 (2004)

[53] X. Liu, K. Kitamura, K. Terabe, H. Hatano and N. Ohashi, *Appl. Phys. Lett.*, 91, 044101 (2007)

[54] P. M. Jones, S. Dunn, *Nanotechnology*, 18, 185702 (2007)

[55] P. M. Jones and S. Dunn, *J. Phys. D: Appl. Phys*. **42,** 065408 (5pp) (2009)

[56] M. H. Zhao, D. A. Bonnell and J. M. Vohs, *Surf. Sci.*, 602, 2849-2855 (2008)

[57] D. B. Li, M. H. Zhao, J. Garra, A. . Kolpak, A. M. Rappe, D. A. Bonnell and J. M. Vohs, *Nature Mater.*, 7, 473-477 (2008)

[58] S. Habicht, R. J. Nemanich and A. Gruverman, *Nanotechnology*, 19, 495303 (2008)

[59] A. Haussmann, P. Milde, C. Erler, and L. M. Eng, *Nano Lett., 9* (2),763–768 (2009)

[60] A.G.Chynoweth , *Phys. Rev.*, **102**, 705 (1956)

[61] F.S.Chen, *J. Appl. Phys.*, **40**, 3389 (1967)

[62] A.M. Glass, D. von Linde and T. J. Negran, *Appl. Phys. Lett.*, **25**, 233 (1974)

[63] P. S. Brody, *Bull. Amer. Phys. Soc.*, **18**, 65 (1973)

[64] Y. Inoue and K. Sato, *J. Chem. Soc., Faraday Trans 1*, **85,** 7, 1765-1774 (1989)

[65] A. L. Kholkin , V. K. Yarmarkin, B. M. Goltsman, J. L. Baptista, *Integ. Ferro.*, 35, 261-268 (2001)

[66] A. L. Kholkin, S. O. Lakovlev, J. L. Baptista, *Appl. Phys. Lett.*, 79, 13 (2001)

[67] M. Qin, K. Yao, Y. Liang, S. Shannigrahi, *J. Appl. Phys.*, 101, 014104 (2007)

[68] C. Z. Rosen, B. V. Hiremath and R. Newnham, *Piezoelectricity* , American Institute of Physics, New York, page 15 (1992)

[69] B. Jaffe, W. Cook and H. Jaffe, *Piezoelectric ceramics,* Academic press, London and New York (1971)

[70] B. Jaffe, R. S. Roth and S. Marzullo, *J. Res. Nat. Bur. Stds*., 55, 239-254 (1955)

[71] J. F. Scott and C. A. Paz de Araujo, *Science*, 246, 1400 (1989)

[72] S. A. Long and R. N. Blumenthal, *J .Am. Ceram. Soc.*, 54, 577-583 (1971)

[73] D. M. Smyth, *Curr. Opin. Solid State Mater. Sci.*, 1,692-697 (1996)

[74] B.T. Matthias and J. P. Remeika, *Phys. Rev.*, 76, 1886 (1949)

[75] S. Ganesamoorthy, M. Nakamura, S. Takekawa, S. Kumaragurubaran, K. Terabe, and K. Kitamura, *Mater. Sci. Eng. B,* 120, 125 (2005)

[76] S. C. Abrahams, W. C. Hamilton A. Sequiera, *J. Phys. Chem. Solids,* 28, 1693 (1967)

[77] D. Xue and K. Kitamura, *Ferroelectrics,* 297:1, 19-27 (2003)

3. Experimental Procedure

3.1 Samples used

In this work, two different ferroelectric materials were used. One was polycrystalline lead zirconate titanate (PZT) thin films and the other was single crystal lithium niobate (LN). The details of samples used are given below:

1. Lead zirconate titanate (PZT)

   Three different compositions of PZT were used in this work:

   1. $Pb(Zr_{0.30}Ti_{0.70})O_3$ or PZT 30/70 on $Pt/Ti/Si/SiO_2$
   2. $Pb(Zr_{0.52}Ti_{0.48})O_3$ or PZT 52/48 on $Pt/Ti/Si/SiO_2$
   3. $Pb(Zr_{0.70}Ti_{0.30})O_3$ or PZT 70/30 on $Pt/Ti/Si/SiO_2$

   The preparation of PZT samples is discussed in detail in section 3.2.

2. Lithium niobate (LN)

   We have used two samples of LN sample for our study:

   1. Single crystal congruent lithium niobate
   2. Single crystal 5% MgO-doped lithium niobate

   The LN crystals were obtained from MTI Corporation. They were z-cut and exhibit a hexagonal structure below the Curie temperature of 1160ºC with polarisation along the 'c' axis. Crystals have been poled to present either C^+ or C^- faces.

3.2 PZT sample preparation

3.2.1 Substrate preparation

Si wafers with a layer of silicon oxide at the top were used as substrates. Physical vapour deposition (PVD) sputtering technique was utilised to deposit a bottom electrode of Pt on Si/ SiO_2 substrate. For the bottom electrode, the Si wafer was

placed inside the Nordiko sputterer and a 5 nm thick layer of Ti was sputtered, followed by a 100 nm thick Pt layer. This process resulted in deposition of Pt films with [111] orientation. Ti layer was sputtered to improve the adhesion between Pt and SiO_2, and in the absence of Ti layer the Pt electrode would peel off[1].

3.2.2 PZT film deposition

Ferroelectric PZT thin films were prepared using the sol-gel technique. Ready prepared PZT sols of PZT 30/70, PZT 52/48 and PZT 70/30 composition each of 0.4 M concentration were deposited on the prepared platinised Si wafer via the spin-coating technique. The substrate was placed inside the Cookson G3-8 spin coater, several drops of PZT sol that was filtered using a 0.2 μm filter were placed on it, and the sol was then spin coated. The standard deposition settings are given in Table 3.1.

Table 3.1 Settings for Cookson G3-8 spin coater

Spin speed	3000 RPM
Acceleration time	3 sec
De-acceleration time	3 sec
Spin time	30 sec

The settings in Table 3.1 resulted in deposition of PZT film of thickness 70 nm. The processing of PZT films was done according to previously published work[2,3]. Immediately after spin coating, the films were transferred to hot plate for drying and then were finally annealed at high temperature. The drying and annealing temperature for PZT 30/70, 52/48 and 70/30 are given in Table 3.2.

Table 3.2 Drying and annealing temperatures for PZT of different compositions

PZT	Drying (Hotplate)	Annealing (Hotplate)
30/70	200 ºC for 30 sec	540ºC for 10 min
52/48	300 ºC for 30 sec	600ºC for 10 min
70/30	315 ºC for 30 sec	630ºC for 10 min

When a PZT thin film is spun onto the prepared substrate and dried, the sol transforms into a non-ferroelectric pyrochlore phase, and upon further heat treatment the nucleation of ferroelectric perovskite phase from the pyrochlore phase occurs[4]. As determined from this work, the films with higher Zr/Ti ratios require a higher crystallisation temperature. For thicker films, the same process of coating, drying and annealing was repeated until the final thickness was reached.

3.3 Conventional chamber furnace

The annealing of PZT thin films was performed in a conventional chamber furnace (Carbolite ELF 11/6B). The temperatures and reaction times for experimental work ranged from 100 – 700 °C and 5 min to 2 hrs, respectively. Samples were loaded into the furnace while cold, and the required parameters were entered via a programmable electronic control unit. The ramp rate used for the annealing experiments was 3 °C/min. Once the desired temperature was reached the timer would start, the ramp rate for cooling was also 3 °C/min.

3.4 X-ray diffraction (XRD)

The prepared PZT samples were examined using a Siemens D5005 X-ray Diffractometer (XRD) to determine their degree of crystallinity and crystallographic orientation. The degree of crystallinity of PZT is examined by detection of pyrochlore peak at around $2\theta = 29.8°$.[5] When the PZT thin films were scanned in 2θ range of 20º to 60º, a diffraction pattern was obtained which consists of all peaks with high intensities. Upon comparing the obtained pattern with JCPDS (Joint Committee for Powder Diffraction Standards) file (file no. 33-0784), the information on crystallinity and orientation of PZT was obtained.

3.5 Poling

3.5.1 Atomic Force Microscopy (AFM)

Poling of ferroelectric PZT thin films was done using a DI Dimension 3000 Atomic Force Microscope (AFM) in Piezoresponse Force Microscopy (PFM) mode. The cantilever used was SCM-PIT model from 'Veeco'; it was made up of Antimony doped Si and was PtIr coated. Poling was done by connecting a DC supply of 12 volts (an electric field of 170 $KVmm^{-1}$) across the conductive cantilever tip and the bottom electrode. The bottom electrode of PZT thin film was obtained by scratching a corner of PZT film and connecting a wire to the base electrode using silver dag. The largest area that can be poled using a PFM is 100 ×100 μm and the smallest poled region was 400 ×400 nm in size. Positive voltage was applied to the cantilever tip to pole a negative (C^-) domain and negative voltage was applied to the tip to pole a positive (C^+) domain.

Imaging of domain structure was done using PFM. Firstly, the PZT sample was fixed firmly on the base plate of AFM using a double sided Carbon tape. An AC

modulation voltage of 3 V_{pk-pk} was applied across the cantilever tip and the bottom electrode of the sample at a frequency of 18 kHz. Images of domain map and topography of the sample are saved as *.tif files. A schematic of experimental set-up of Piezoresponse Force Microscopy is shown in Figure 3.1. A typical poled pattern on PZT surface is shown in Figure 3.2. Bright areas in the image are C^+ domains, dark areas are C^- domains and the surrounding region is an unpoled area.

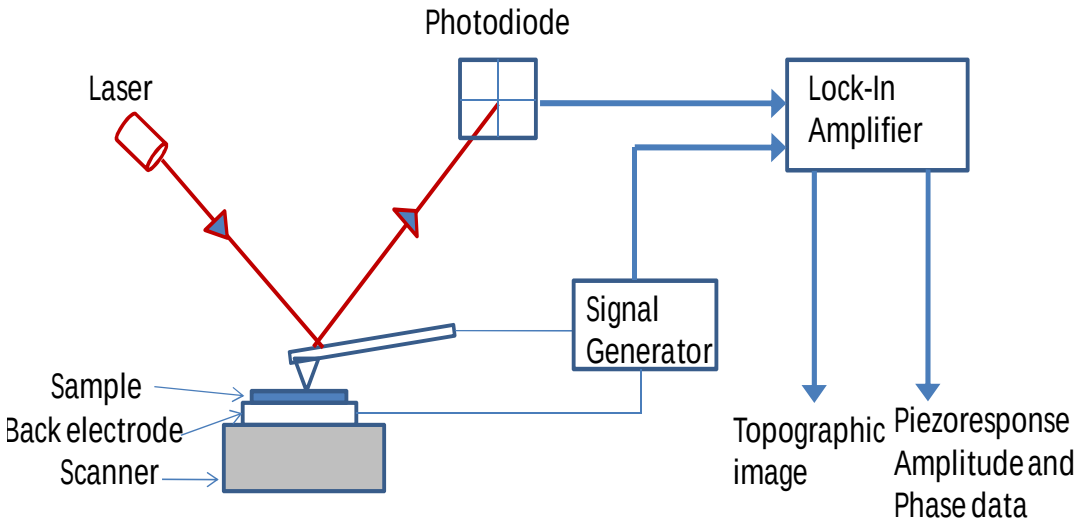

Figure 3.1 A generalised experimental setup of PFM

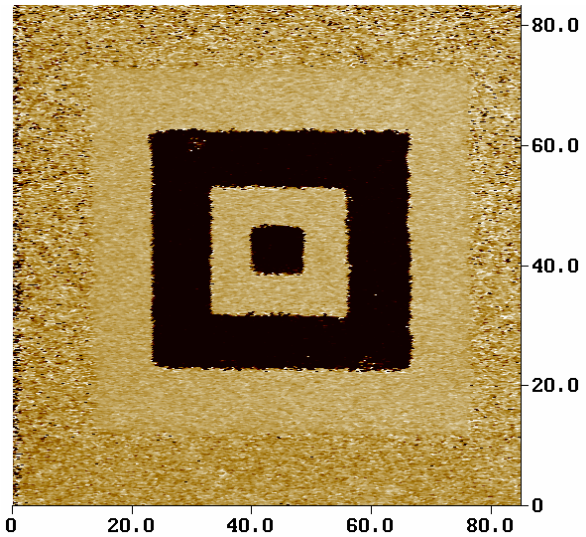

Figure 3.2 A PFM image of a typical poled pattern on PZT surface. Bright areas in the image are C^+ domains and dark areas are C^- domains, the surrounding region is an unpoled area.

3.5.2 Corona poling

Bigger areas up to the size of 5×5 mm were poled using corona poling method. The PZT sample was placed firmly on the base plate such that the region to be poled was directly underneath the sharp needle. The distance between the tip of the needle and the sample was 3 cm. For poling a high voltage supply of 6 kV was applied between the needle and the ground plate for one minute. For C^- domains, the needle was connected to a +6 kV and the base plate was grounded, whereas for C^+ domains the needle was connected to -6 kV and the base plate was grounded.

3.6 Piezometer system

The polarity of LN crystals was determined by using a 'TakeControl' Piezometer system. The sample under investigation was clamped between the jaws of the force head unit. An oscillating force of 0.1N is applied to the sample. The display panel shows the d_{33} readings in the units of 10^{-12} C/N. The polarity of the lower electrode of the sample was displayed as the polarity of the reading.

3.7 Metal salt solutions

Salt solutions of different metals were prepared for experiments. The selection of silver, gold, aluminium and manganese salt solutions was done in this work because these salts can be photoreduced on a PZT or LN surface to produce respective metal nanoparticles. It is known that for a metal to photoreduce on a semiconductor surface, the reduction potential of the metal has to be within the band gap of the material when plotted on a Normal Hydrogen Electrode scale[6], as shown in Figure 3.3. Details of salts used in experimental work are given in Table 3.3.

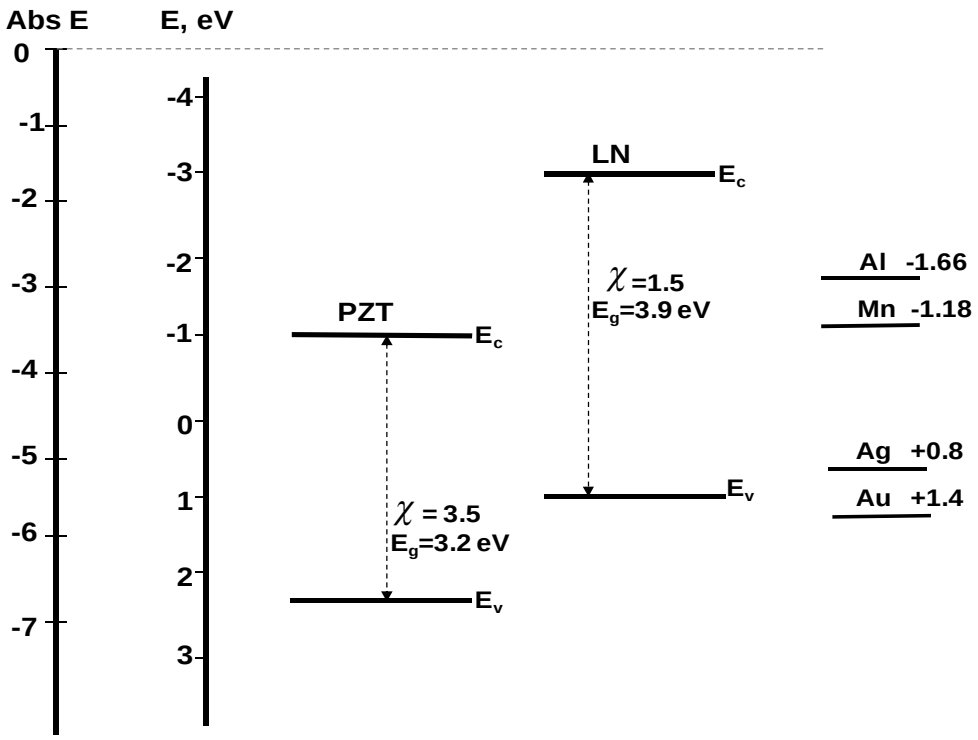

Figure 3.3 Band edges of PZT and LN are mapped with respect to the Normal Hydrogen Electrode (E). The reduction potential of Al, Mn, Ag and Au metals are also plotted against E.

Table 3.3 Salts used in experimental work, their formula and supplier's details

Salt	**Formula**	**Supplier**
Silver nitrate	$AgNO_3$	Sigma-Aldrich, 99.99%
Hydrogen tetrachlourate trihydrate	$AuCl_3.ClH.3H_2O$	Sigma-Aldrich, 99.00%
Aluminium(III) chloride	$AlCl_3$	Sigma-Aldrich, 99.00%
Manganese(II) nitrate hydrate	$Mn(NO_3)_2 . H_2O$	Aldrich, 98.00%

In order to make a 0.01M $AgNO_3$ solution 17$\pm$3 mg of $AgNO_3$ salt was dissolved in 10ml of de-ionised water. Gold chloride solution of concentration 0.001 M was prepared by mixing 3.93$\pm$3 mg of $AuCl_3.ClH.3H_2O$ salt with 10 ml of de-ionised

water. For a 0.01M aluminium and manganese salts, 13.3±3mg of Aluminium chloride and 17.9±3mg of Manganese nitrate was added to 10 ml of water. The prepared salt solutions were filtered using a 0.2µm filter to discard any impurities in the solution.

3.8 UV Irradiation

Irradiation with ultraviolet light was carried out in a UV exposure unit. The unit consisted of a Honle UVASPOT®UV lamp and the sample was placed directly underneath the lamp at a distance of about 10 cm. Upon exposure to the UV lamp, the Unit base could get heated, which in turn can raise the temperature of the sample. An electric fan was fitted to the unit base to control the temperature. According to maufacturer's specifications, intensity incident at the sample surfaces during exposure was at an average of 21 mW. The details of two UV lamps used in experiments are as follows:

1) H lamp: This lamp is an undoped Hg lamp manufactured by Honle. The spectrum of 'H' lamp between the wavelengths 200-400 nm (6.2-3.1 eV) is given in Figure 3.4.
2) F lamp: This is Fe doped Hg bulb manufactured by Honle. The spectrum of 'F' lamp between the wavelengths 200-400 nm (6.2-3.1 eV) is given in Figure 3.5.

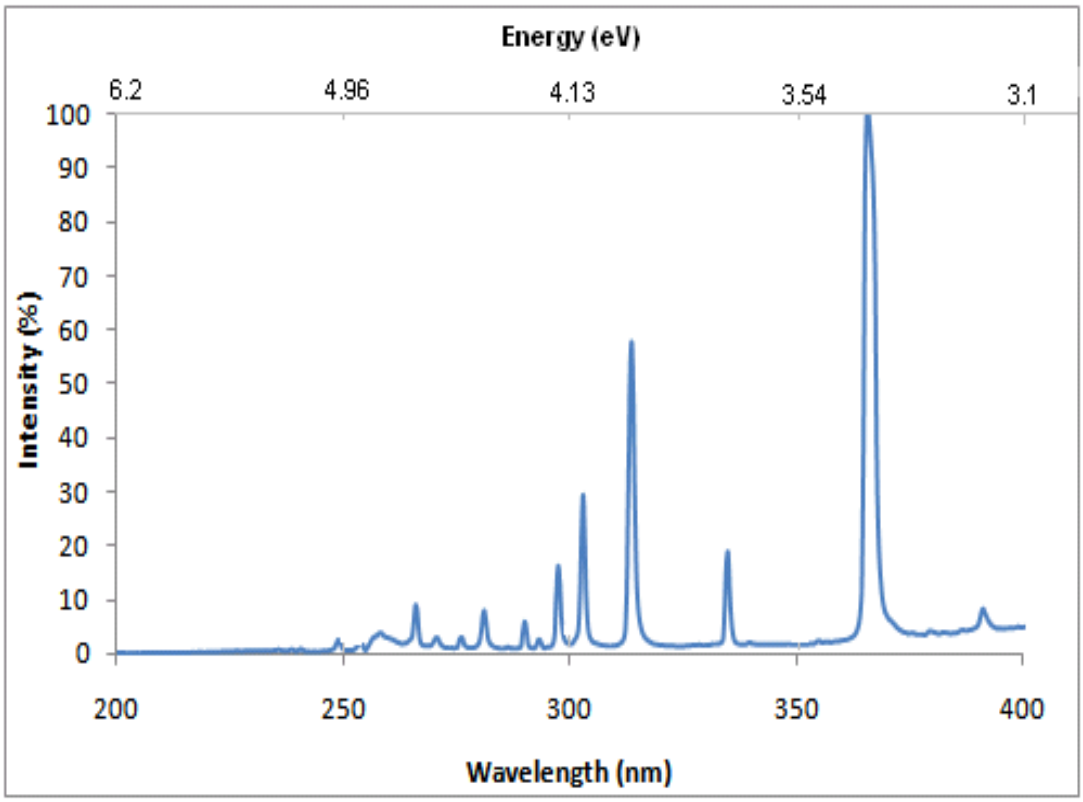

Figure 3.4 Spectrum of 'H' Lamp between the wavelength 200-400 nm (energy 6.2-3.1 eV).

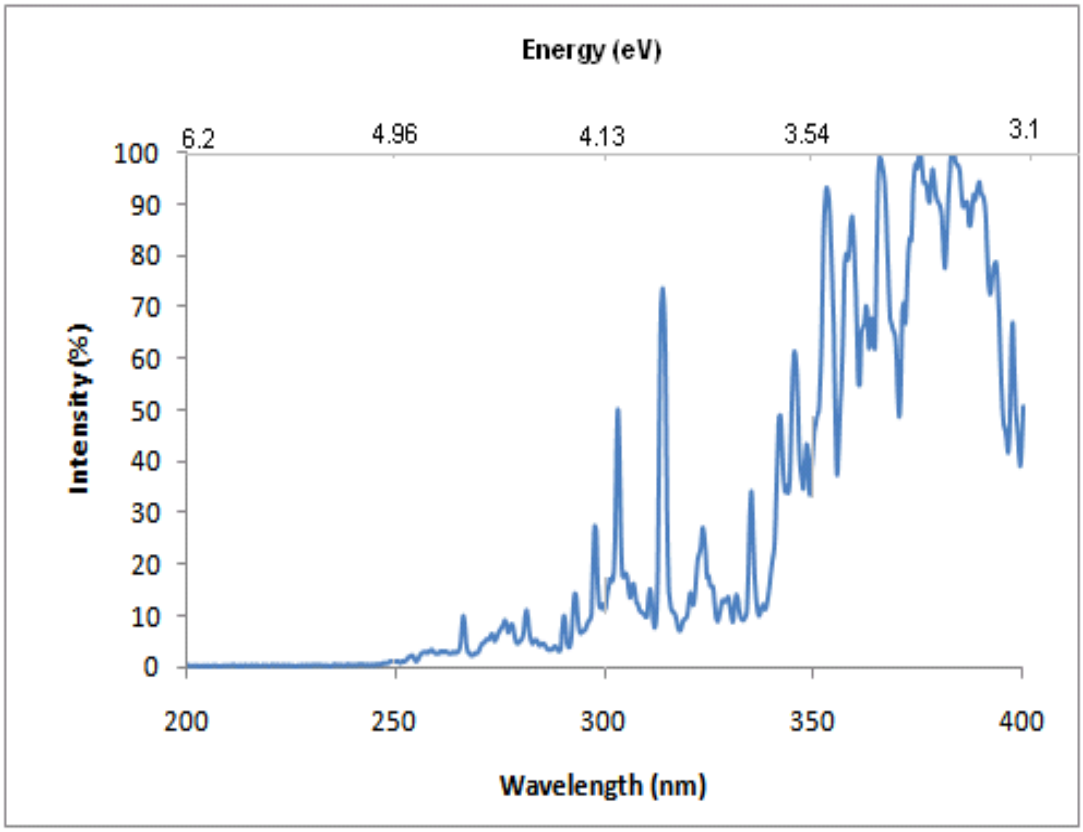

Figure 3.5 Spectrum of 'F' lamp between the wavelength 200-400 nm (energy 6.2-3.1 eV).

3.9 Scanning electron microscope (SEM) and Energy Dispersive X-Ray (EDX) Analysis

After UV experiments, metal deposition on the samples was analysed using a scanning electron microscope (SEM) Phillips XL30 SFEG in secondary electron detector (SE) mode. The energy of incident beam was selected between 15-20 kV, and the contrast and resolution in SEM images was adjusted. The chemical composition analysis of samples was done using the Phillips XL30 SFEG equipped with EDX detection system. The quantitative analysis was performed using the software INCA™.

References

[1] G.M. Chow, L. K. Kurihara. *Nanostructured materials, processing, properties and potential applications,* William Andrew Publishing, Norwich, (2002)

[2] Q. Zhang and R. W. Whatmore, *J. Phys. D: Appl. Phys.*, 34, 2296-2301 (2001)

[3] J. M. Marshall, S. Corkovic, Q. Zhang, R. W. Whatmore, C. Chima-Oreke, W. L. Roberts, A. J. Bushby and M. J. Reece, *Integ. Ferro.*, 80, 77-85 (2006)

[4]S. Dunn , Q. Zhang and R. W. Whatmore , *Integ. Ferro.*, 46, 1, 87-94 (2002)

[5] K. G. Brooks, I. M. Reaney, R. Klissurska, Y. Huang, L. Bursill, N. Setter, *J. Mater. Res.*, 9, 10, 2540 (1994)

[6] P. M. Jones, D. E. Gallardo and S. Dunn, *Chem. Mater.* 20, 5901–5906 (2008)

4. Selective metal deposition on domain patterned lead zirconate titanate

Ferroelectric materials possess a unique property of sustaining spontaneous polarisation below the Curie temperature and this constitutes the basis of their wide technological applicability[1]. Kalinin *et al.*[2] proposed a novel application of ferroelectrics to facilitate the growth of self assembling nanostructures on predefined locations on a ferroelectric surface. Since then, there has been an increase in the interest in the use of ferroelectric materials in photochemistry. PZT has gained special interest in this area due to its unique properties; it possesses a low magnitude of coercive field and it is therefore easy to pattern a domain structure on PZT, and it possesses a spontaneous polarisation of 20 ± 3 $\mu C/cm^2$. In this chapter, the photoreduction of silver on domain patterned PZT is demonstrated. The impact of annealing the PZT thin films on the photochemical properties is investigated. The impact of Zr/Ti ratio in PZT and the impact of size of poled pattern on deposition of silver are verified. It is shown that it is possible to photoreduce gold in the form of spherical and triangular nanoplates.

4.1 Photoreduction of silver salt solution on domain patterned PZT

4.1.1 Experimental Procedure

A 70 nm thick film of PZT (30/70) was prepared with a final annealing temperature of 540°C. XRD was performed on the PZT sample to check the crystallographic orientation of the film. Hysteresis loop measurements were done on the PZT film using an RT66A. Topology of the film was studied using an AFM and an area on the

film was poled using PFM. After poling a pattern on the PZT surface in the form of squares, a drop of freshly made silver nitrate salt solution which was filtered using a 0.2 μ m filter was placed over the poled area. The poled pattern dipped in silver nitrate solution was exposed to 'H' lamp for 20 minutes. Finally, the Ag deposition on the PZT surface was analysed using SEM and EDX.

4.1.2 Results and discussion

The XRD plot shown in Figure 4.1 depicts that the PZT film exhibits good [111] orientation and confirms the absence of any pyrochlore phase.

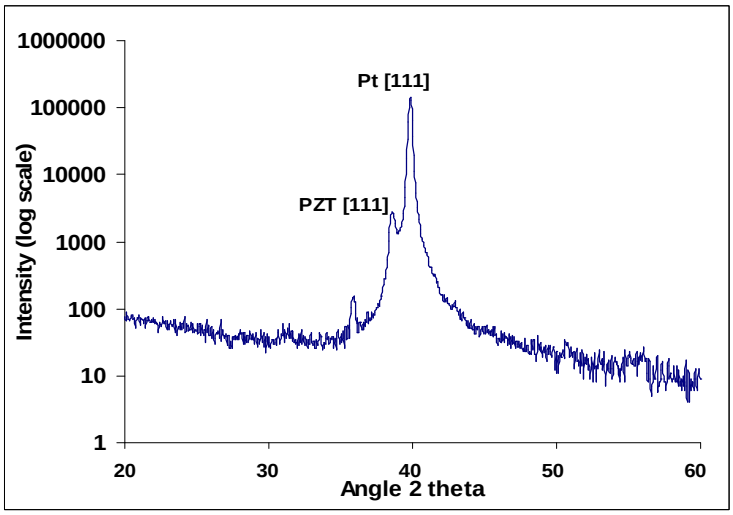

Figure 4.1 XRD plot for PZT (30/70) film showing orientation in [111] direction.

The PZT film exhibited good ferroelectric properties as determined by hysteresis loop measurements. The hysteresis loop for the film is shown in Figure 4.2. The film possesses an average remnant polarisation of 20 ± 3 $\mu C/cm^2$. Figure 4.3 (a) shows an AFM study of the topology of the PZT film and depicts that the film is composed of fine grains of about 70-100 nm in size (as determined by the particle analysis software in AFM). A PFM image of the poled pattern is shown in Figure 4.3 (b). In the PFM image bright squares are C^+ domains, dark squares are C^- domains and the surrounding region is an unpoled area showing the random orientation of the

produced film. A 3-D topographic image of poled pattern in Figure 4.3(c) shows that domain polarization overwhelms any other crystal structural factors.

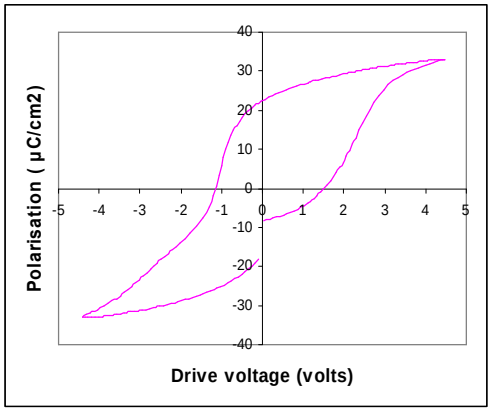

Figure 4.2 Hysteresis loop for 70 nm thick PZT (30/70) film.

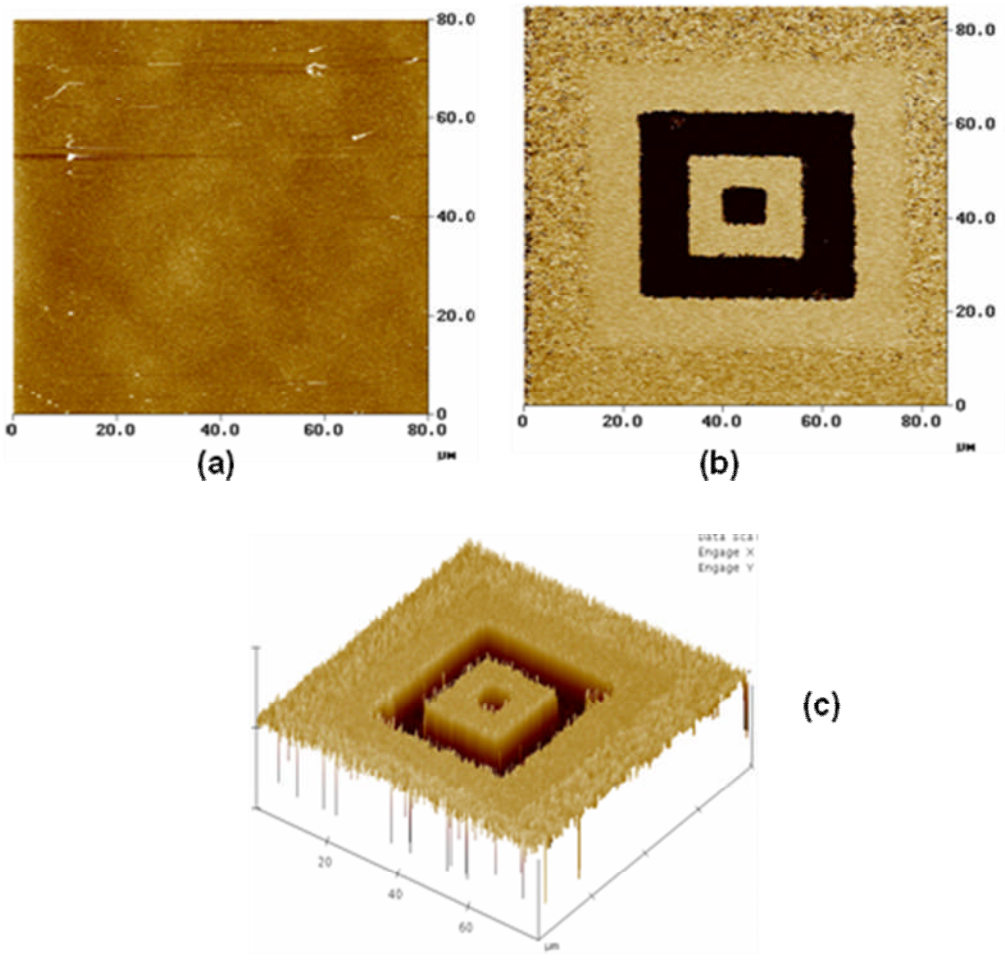

Figure 4.3 (a) Topology of the sample as seen by AFM (b) PFM image of poled pattern, brighter squares in the picture are C^+ domains and the dark squares are C^- domains, surrounding region

is an unpoled area. (c) 3-D topographic image of poled pattern showing that domain polarisation overcomes any other crystal structural features. The scale bar shows the length in µm.

An SEM image of the poled pattern after silver deposition is shown in Figure 4.4 (a). Irradiation with both 'H' and 'F' lamp gave metal deposition only on C^+ domains and no deposition occurred on C^- domains. Figure 4.4 (b) shows a clear demarcation in Ag deposition on C^+ and C^- domains.

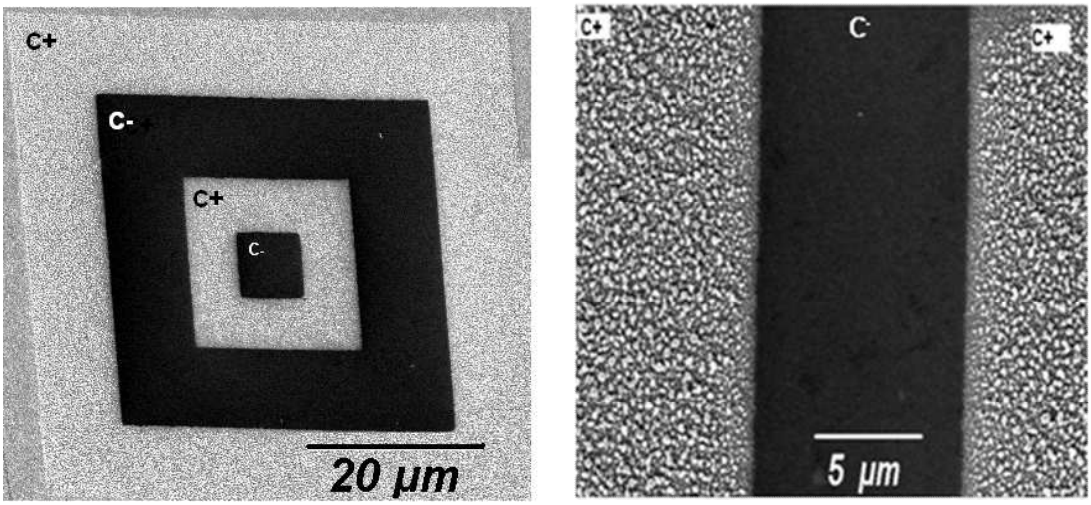

(a) **(b)**

Figure 4.4 (a) SEM image of the poled pattern after silver deposition. Silver is deposited on C^+ domains and no deposition occurred on C^- domains, (b) a magnified SEM image showing clear demarcation between C^+ and C^- domains.

When a PZT thin film is exposed to UV light with energy greater than the band gap of PZT (i.e. > 3.2 eV[3]), electrons in the valence band are excited to the conduction band leading to the creation of electron hole pairs[4] in both the surface layer and the bulk of the film[5]. These charge carriers are established in the domains and are separated by internal electric field in the SCR[6] in less than 10^{-12} s. In the positively polarised (C^+) domains, electrons are forced to migrate towards the surface[7] and in negatively polarised (C^-) domains electrons move away from the surface and towards the bulk. On C^+ domains the available electrons (e^-) can react with silver cations (Ag^+) and get reduced to metal (Ag) as shown in Equation 4.1. On the C^- domain, no silver

deposition occurs because of the unavailability of electrons at the surface. Due to the presence of holes the surface of C^- domain acts as oxidative in nature. The most probable oxidation reaction occurring on the C^- surface is oxidation of water, as shown in Equation 4.2.

$$Ag^+ + e^- \rightarrow Ag^0 \quad \textbf{(Equation 4.1)}$$

$$H_2O + h^+ \rightarrow \frac{1}{2}O_2 + 2H^+ \quad \textbf{(Equation 4.2)}$$

EDX analysis of poled pattern was done to verify the presence and absence of silver on C^+ and C^- domains respectively. The poled pattern is shown in Figure 4.5 (a) and the EDX spectrums are shown in Figure 4.5 (b) and (c). This confirms the presence of Ag on C^+ domains (Spectrum 2) and absence of Ag on C^- domains (Spectrum 1).

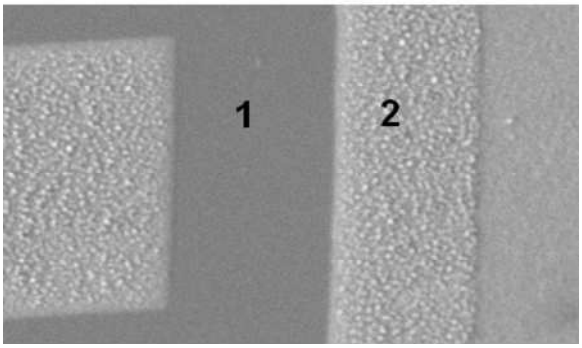

(a)

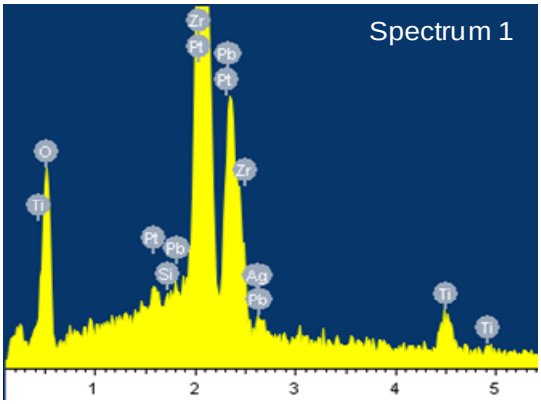

(b)

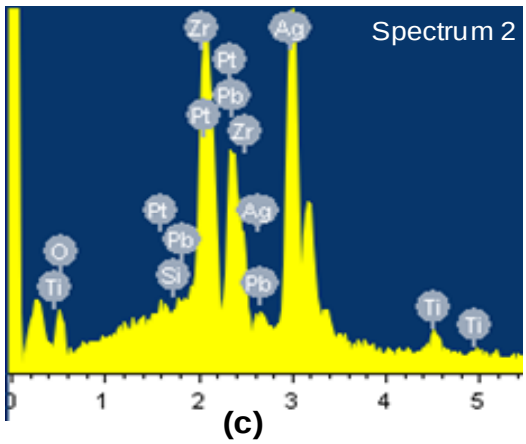

(c)

Figure 4.5 (a) SEM image depicting spectrum 1, 2 where 1 is C^- domain and 2 is C^+ domain; (b) EDX spectrum of area 1 showing absence of Ag peak at 2.9 eV, hence confirming the absence of

Ag on C^- domain; (c) EDX spectrum of area 2 showing a strong peak of Ag at 2.9 eV, hence confirming the presence of Ag on C^+ domain.

There is an interesting aspect to the growth of silver on C^+ domain. On the surface of the C^+ domain, the negatively charged counter ions will form a Stern or double layer due to standard Helmholtz theory. Although the mechanism of screening in PZT is predominantly internal, there will still be a thin layer of nitrate ions $(NO_3)^-$ adsorbed on the surface of C^+ domain and as a result of this the Ag^+ ions will not be intimately attached to the surface as shown in Figure 4.6 (right). On the surface of C^- domain Ag^+ ions would be forming a Stern layer as shown in Figure 4.6 (left).

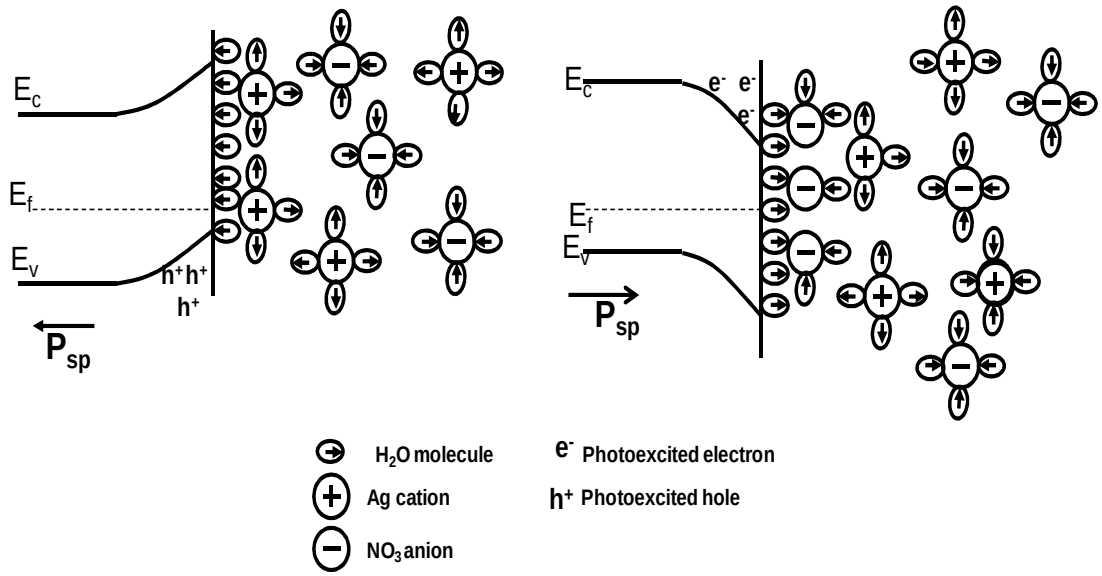

Figure 4.6 Surface of C^- (left) and C^+ (right) domain of PZT dipped in silver nitrate solution. The arrow (P_{sp}) shows direction of spontaneous polarisation.

For the photoexcited electron in the conduction band of the PZT to interact with the Ag^+ in solution, it must tunnel from the PZT surface through the screening layer of adsorbed anions to reach the cation Ag^+. This tunnelling of electrons from the PZT can occur at discrete locations where the Stern layer has been disrupted due to discontinuity in the local electric field. Therefore, free electrons are available at these locations and they tunnel through the disturbed Stern layer and perform chemical reaction. Hanson *et al.*[8] found that the nucleation points for silver growth on a LN

crystal were domain boundaries and Jones *et al.*[9] found that silver growth started at grain boundaries on a PZT surface. Figure 4.7(a) shows that silver growth nucleates at discrete locations on the surface that are indicative of a disruption of the Stern layer due to a surface defect or electric field in the substrate. As shown in Figure 4.7(a), the grain boundaries seem to be void of any silver. This is in contrast to the results observed by Jones *et al.* where preferential deposition was occurring at grain boundaries.

Under the continuous supply of UV light, the silver clusters start to grow bigger and continue to grow up to a point where the entire surface is covered with silver and there is no scope for UV light to reach the PZT surface and generate fresh electron-hole pairs. At this stage optimum growth of silver has occurred and further exposure to UV light will not enhance any further deposition. Figure 4.7(b) shows the coverage of entire C^+ domain when UV light is irradiated for 25 minutes.

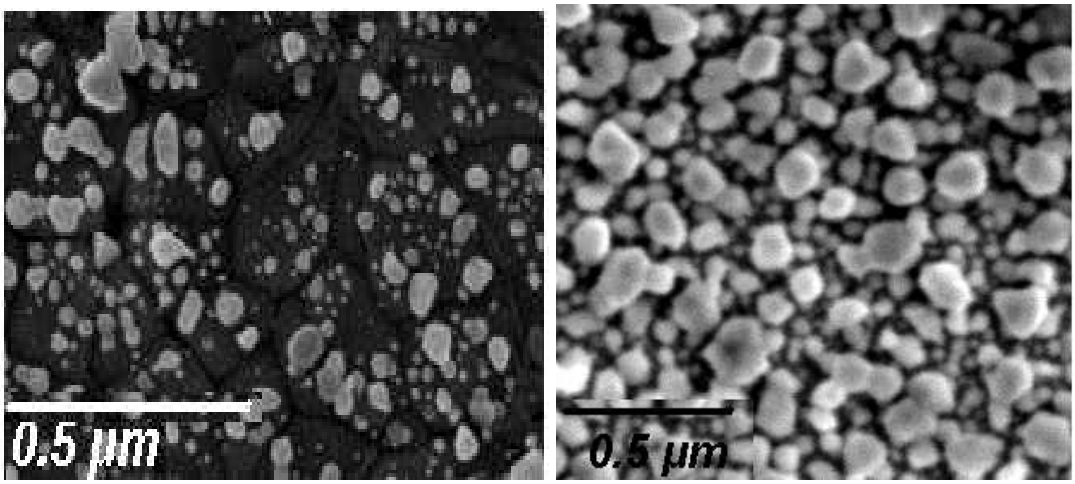

(a) **(b)**

Figure 4.7 (a) SEM image showing pattern of silver deposition in discrete particles when exposed to UV light for 10 minutes and (b) when UV light is irradiated for longer, the whole C^+ domain is covered with photoreduced silver.

The deposited silver was mechanically removed by rubbing a bud dipped in acetone and IPA on the surface. The poled pattern was made clear of silver, and SEM analysis

confirmed the absence of silver over the poled pattern. The silver deposition experiments were then repeated on the poled area and again selective deposition on C^+ domains was observed. This process of removing silver from the surface and depositing silver again was repeated eight times and excellent reproducibility was obtained in each case. Therefore, PZT is a very good material for performing ferroelectric lithography because of its mechanical stability and rigidity that allows the reuse of the same substrate for many deposition test series. In addition to this, the domain structures generated by PFM on PZT show a good long-term stability; no noticeable changes were observed over more than a year.

4.2 Impact of defect concentration on the photochemical deposition of silver onto PZT thin films

4.2.1 Introduction

Ferroelectric thin films have potential to be used as memory (FeRAM) in microcircuits and PZT has long been the leading material considered for ferroelectric memories.[10] An example of a real commercially available memory is the Samsung lead zirconate titanate based 4 Mbit 1T-1C ferroelectric memory[10]. In order to optimise the performance of PZT based devices, a good knowledge of its defect chemistry is required. In this section, the impact of annealing and increasing the defect concentration in PZT thin films on the photochemistry of PZT was investigated. It was found that the density of defects in PZT has an affect on the photochemical reactivity at its surface through an interaction with the band structure that arises from the development of new trap and defect states. Silver deposition experiments on the C^+ and C^- domain of PZT (30/70) thin films were performed at samples annealed at a variety of temperatures from 530 - 690°C. The impact of

annealing was shown to alter the defect concentration of the PZT as demonstrated by an increase in the deposition of silver on the surface. When the PZT samples were annealed in air at temperatures ranging from 530-690°C, the silver deposition on C^+ domains increased by more than 150% and the size of deposited silver clusters increased by about four times.

Synthesis of size and shape controlled noble metal particles has gained considerable attention in the last few years because the optical, electrical and catalytic properties of noble metal nanoparticles are dependent on their size, shape, composition and crystallinity[11]. The method developed in this section enables synthesis of silver particles of desired size ranging from 50 nm to 400 nm. In addition to this, by tracking the change in the photochemical reactivity of PZT with respect to the defects, a handle for understanding the impact of trap and defect states on the electrical performance of the PZT is also generated, for example in an FeRAM device.

4.2.2 Experimental procedure

A 70nm thick film of PZT (30/70) (final annealing temperature 540ºC) was cut into pieces and each PZT sample was annealed separately at 590º C, 640º C and 690º C for 60 minutes in a furnace. The furnace was set to reach up to the desired temperature and stay at that temperature for 60 minutes and then it cooled at the rate of 3º C per minute. The samples were poled using the PFM and then exposed to 'H' lamp for 20 minutes each. The metal nanoparticle deposition process was carried out on all the PZT samples. In PZT thin films, the central area of the sample may have different properties from the edge; therefore central region of the film was always used for experiments. Finally, SFEG Scanning Electron Microscope (SEM) analysis (high resolution mode and beam energy 10 keV) was done on all the samples to analyse the

size and shape of deposited silver particles. Energy Dispersive X-ray (EDAX) analysis (Beam energy 15 keV) was carried out on all the samples to evaluate the percentage deposition of silver. The EDAX software was first calibrated using a standard Co sample. An area of size approximately 10 μm × 10 μm was selected on all the samples and quantitative analysis was done individually on all the PZT samples. Energy spectra corresponding to elements present in the observed PZT sample were obtained. A table showing the percentage of each element present in the PZT sample was also obtained.

4.2.3 Results and discussion

As determined by XRD the PZT 30/70 films exhibited a [111] orientation. The XRD also shows an absence of any intermediate pyrochlore phase in the samples. The XRD patterns for all samples after annealing are compared, shown in Figure 4.8, and no significant change was found in the XRD pattern with respect to annealing temperature. This implies that annealing at different temperatures has no effect on crystallinity of the PZT thin film because it was already very well crystallised at 540ºC and the absence of any pyrochlore phase confirms this.

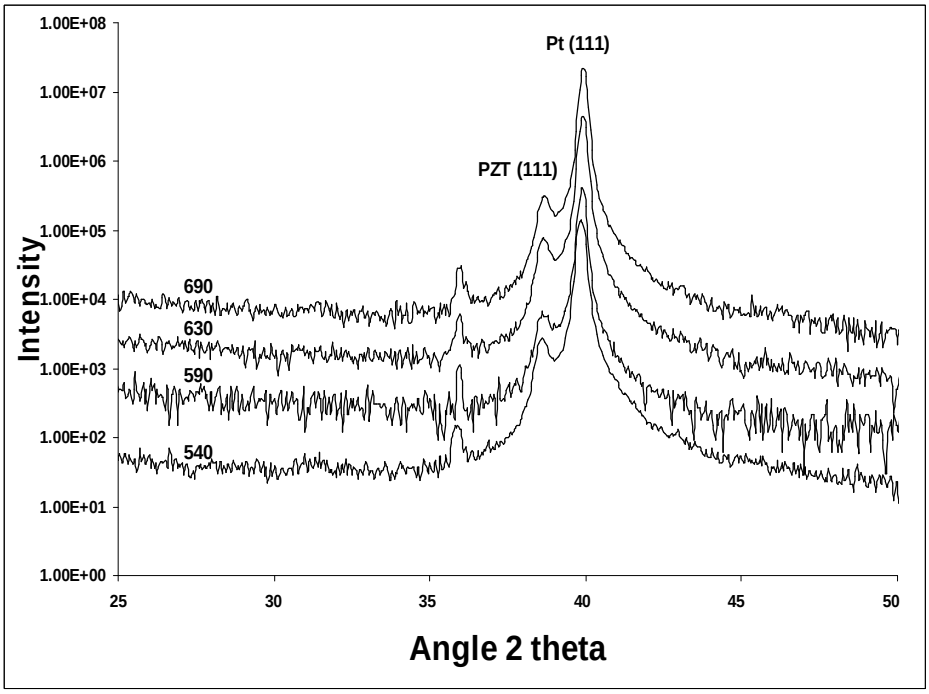

Figure 4.8 A comparison of XRD patterns for PZT samples annealed at temperatures 540º C, 590º C, 630º C and 690º C. X-axis is the scan angle in 2 theta degree and Y axis represents intensity in counts.

Before poling, the PZT was investigated using PFM and showed discrete grains with a random orientation across the surface, as expected. PFM was then used to write positive (C^+) and negative (C^-) domain patterns in the form of squares. On all the PZT samples upon irradiation, silver deposition occurred only on C^+ domains and no deposition was observed on C^- domains.

According to Scott *et al.*[12], the density of defects on the surface of PZT films is high (10^{14} cm^{-2}) as compared to other ferroelectric materials e.g. $LiNbO_3$ (10^{12} cm^{-2})[13]. This is due to the high temperature required for crystallisation of PZT films that induces defects into the PZT. The band gap of PZT material has been reported to range from 3.2-3.7 eV[14]. According to Kalinin *et al.*[2], energy above 4.5 eV is required for the photoreduction of Ag on the surface of PZT; the increase in irradiation over and above the band gap is described as a feature of the interaction between the flux of photons and PZT.

Examination of PZT samples annealed at different temperatures under the SEM clearly showed that the deposition of Ag increased as the temperature of annealing increased from 540º C to 690º C. Using the EDX analysis, a table showing percentage of all the elements present in PZT samples annealed at different temperatures was obtained. The percentage of error in each case was approximately ± 0.6%. These experiments were repeated for a variety of PZT samples and the range of percentage, as determined using EDX, of Ag deposited on the samples was plotted in a graph, as shown in Figure 4.9. A clear trend can be seen - with the increase in temperature of annealing the amount of deposited Ag increases significantly.

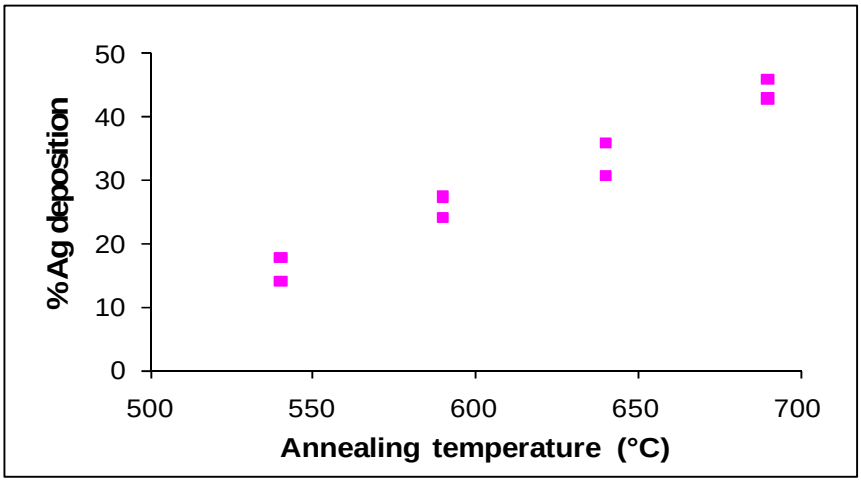

Figure 4.9 Percentage deposition of silver on PZT surface plotted with respect to annealing temperature. There is a clear trend that with the increase in temperature of annealing the amount of deposited silver increases. The two points in the plot show the range in which the percentage deposition of silver was observed at a particular temperature.

The particle size of silver clusters deposited also increases with the increase in annealing temperatures, as shown in Figure 4.10. The average size of silver particles at 540 ºC was 80-120 nm which increased to 350-400 nm on samples annealed at 690 ºC. As there have been no changes to the PZT other than the anneal temperature, this increase in the amount and size of deposited Ag must be due to the changes associated with the high temperature anneal. It is known that PbO can volatise from the surface

of PZT and excess PbO is added to the starting material to accommodate loss during processing.

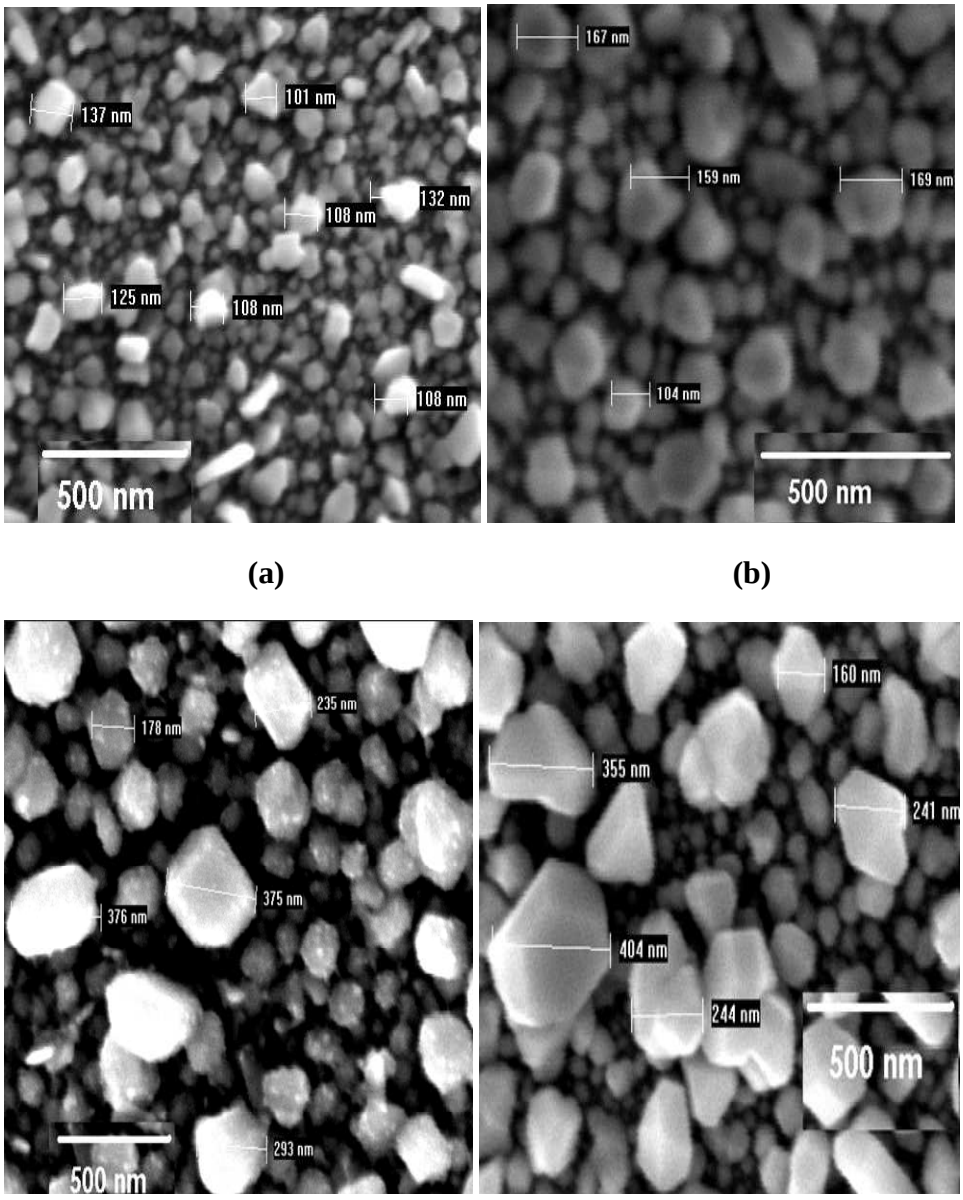

Figure 4.10 SEM images after silver deposition on samples annealed at 540º C (a), 590º C (b), 630º C (c) and 690º C (d). The samples were exposed to UV light for 25 minutes. With the increase in temperature of annealing of PZT sample the size of deposited silver particles on C^+ domains increases significantly.

It is believed that the observed increase in Ag deposition on the PZT surface is due to an increase in the lattice defect concentration, due to the volatisation of components

(PbO) in the PZT during annealing. It is also possible that thermal cycling could have altered the band gap due to a loss of PbO, making the system non-stoichiometric with respect to lead. However, this affect was discounted as band gap measurements for the annealed samples using spectroscopic ellipsometry technique showed no change in the band gap for the materials in the as produced or annealed states. The absorption coefficient (α) of a material is related to the band gap energy (E_g) by the relation given in Equation 4.3[15].

$$(\alpha E)^{1/2} = A.(E - E_g) \quad \textbf{(Equation 4.3)}$$

$$\alpha = \frac{4\pi\kappa}{\lambda} \quad \textbf{(Equation 4.4)}$$

Where E is energy of incident photon, λ is wavelength of incident photon, A is a constant, k is extinction coefficient of the material. Figure 4.11depicts a plot of $(\alpha E)^{1/2}$ versus E, and the band gap value can be determined by extrapolating the linear portion of the plot to $(\alpha E)^{1/2} = 0$.

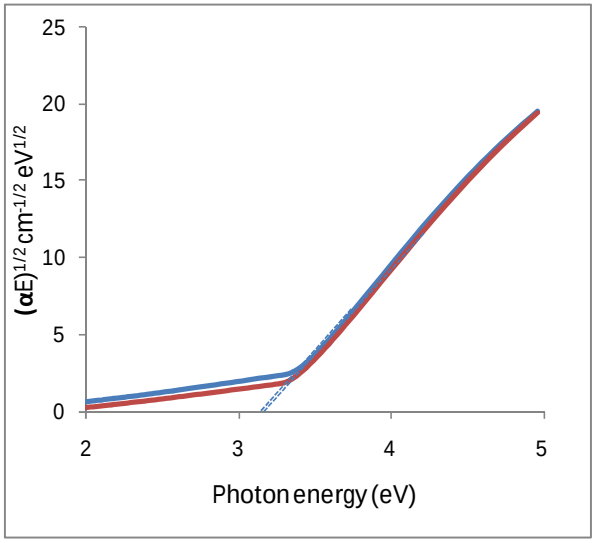

Figure 4.11 Plot of absorption $(\alpha E)^{1/2}$ versus photon energy (E) for PZT (30/70) films annealed at 540° C (blue) and 690° C (red). No change in absorption curve shows that the band gap of the two samples has not changed.

The value of indirect band gap as determined from the plot is approximately 3.17 eV and this value is in agreement with the previous band gap values of PZT reported in literature[14]. As determined from Figure 4.11, there is no change in the band gap of PZT after annealing at 690ºC.

Therefore, other factors that could be affecting the band structure and hence the photochemical deposition of silver on the surface were considered. According to defect chemistry a non-doped PZT film is a p-type semiconductor[12] since the naturally occurring impurities found in the material are acceptor impurities, such as Al^{3+}, Na^{+} and Fe^{3+}. In order to maintain charge neutrality, these acceptor type impurities are integrated by the creation of oxygen vacancies. The oxygen will diffuse out as neutral atom (O_2) leaving behind oxygen vacancies and two electrons[16] (Equation 4.5).

$$O_o = \tfrac{1}{2} O_2 + V_o^{\cdot\cdot} + 2e' \quad \textbf{(Equation 4.5)}$$

PZT also contains two volatile components Pb and O. During crystallisation annealing at high temperatures, PbO volatilises from the film leading to the creation of lead vacancies (V_{Pb}'') and oxygen vacancies ($V_o^{\cdot\cdot}$). These vacancies are mainly at the surface due to the low mobility of lead through the lattice. When annealing under an oxidative atmosphere some oxygen is absorbed into lattice (Equation 4.6)[16].

$$\tfrac{1}{2} O_2 + V_o^{\cdot\cdot} = O_o + 2h^{\cdot} \quad \textbf{(Equation 4.6)}$$

Two holes are produced in this process which are trapped on the doubly negatively charged lead vacant sites, caused by the evaporation of lead, leading to the formation of singly negatively charged complexes as shown in Equation 4.7[17]. $V_o^{\cdot\cdot}$ and $(V_{Pb}^{2+})''$ can also combine to form electrostatically bound complexes as shown in Equation 4.8.

$$(V_{Pb}^{2+})'' + h^{\cdot} = [(V_{Pb}^{2+})'' h^{\cdot}]' \quad \textbf{(Equation 4.7)}$$

$$V_o^{\cdot\cdot} + (V_{Pb}^{2+})'' = (V_o^{\cdot\cdot} V_{Pb}'') \quad \textbf{(Equation 4.8)}$$

Therefore, the system has (acceptor-hole), (lead vacancy-hole), (lead vacancy-oxygen vacancy) complexes in the system and some mobile un-associated oxygen vacancies. Defect chemistry investigations of titanates also show that oxygen vacancies are the dominant defects[17].

Ayguavives *et al.*[18] studied the oxygen diffusion in PZT thin films annealed at various temperatures by ^{18}O depth profiling technique. They deposited PZT films with ^{18}O and then annealed the whole structure with $^{16}O_2$. Thus, studying the amount of ^{18}O left after annealing gave the information about oxygen loss. It was found that a strong depletion of oxygen occurs after annealing and this loss increases with the increase in annealing temperature as shown in Figure 4.12.

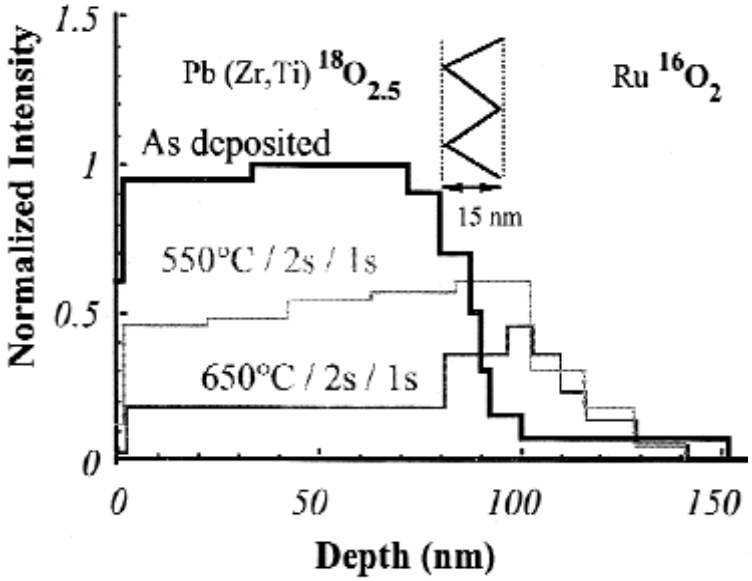

Figure 4.12 The lines denote the experimentally measured excitation curve of $^{18}O_2$ from a PZT sample deposited in a reactive Ar/$^{18}O_2$ atmosphere and annealed at 550 and 650 °C in $^{16}O_2$. (Source ref. 18)

However it was seen that some oxygen is gained during the annealing process (according to Equation 4.6) but the final amount of O content in films decreases with the increase in temperature of annealing[18]. It was found that the steady-state leakage current density of PZT film annealed at 550 ˚C increased by a factor of 10^3 when

annealed at 650 ˚C, as shown in Figure 4.13. This increase in conductivity of film was attributed to the increase in oxygen vacancies and other defect states.

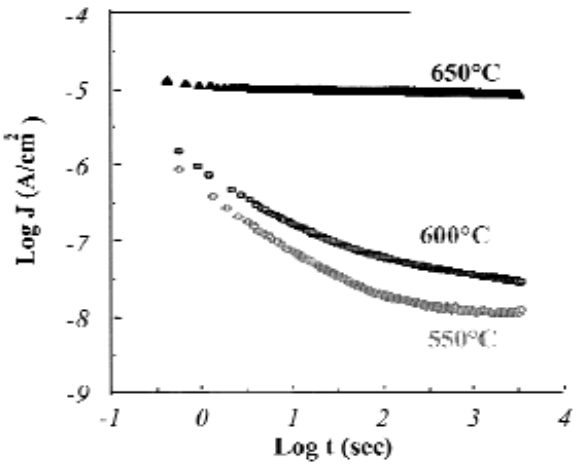

Figure 4.13 Diagram of leakage current density versus time of PZT thin films annealed at 550, 600, and 650 °C under oxygen atmosphere. (Source ref. 18).

Therefore, as the PZT samples are annealed at increasingly higher temperatures, more PbO evaporates from the surface leading to an increase in Pb and O vacancies. EDX analysis of the PZT samples was undertaken which reveals the percentage composition of different elements in the PZT. The relative percentage of Pb present in all the samples is plotted in Figure 4.14, which confirms the loss in the percentage of Pb with respect to annealing temperatures.

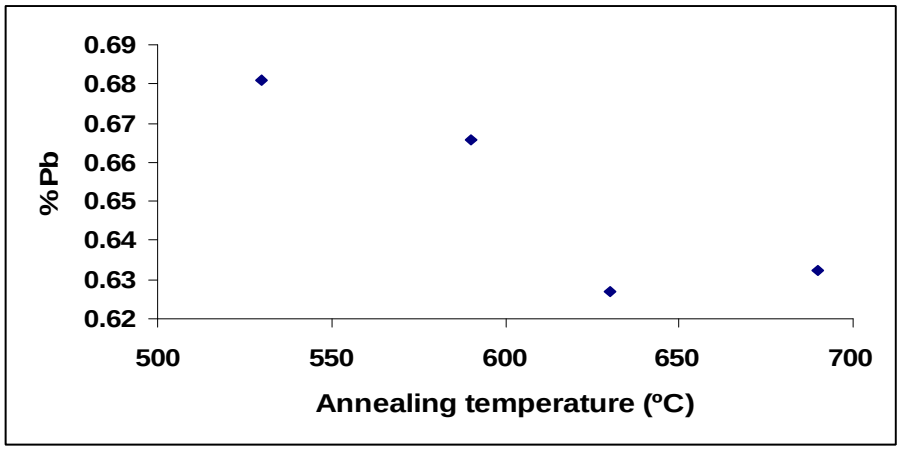

Figure 4.14 Percentage of Pb with respect to annealing temperatures of samples

Although the total loss of Pb from the entire film is about 7% but as PbO evaporates from the surface, therefore most of Pb loss occurs on the surface of PZT film leaving majority of unit cells on the surface defected.

It has been observed experimentally by Robertson and Warren that, oxygen vacancies are positively charged and they produce shallow levels in the band gap which act as donors[19]. Oxygen vacancies introduce shallow level surface states inside the band gap[20], as shown in Figure 4.15. These surface states can act as electron traps during UV irradiation.

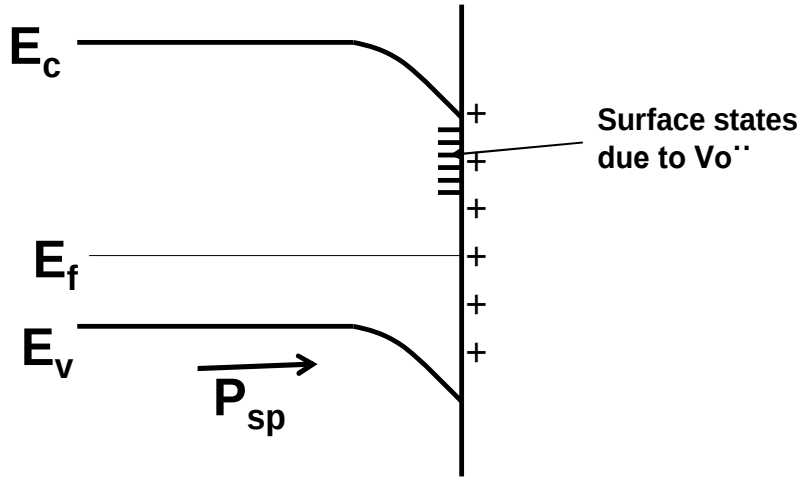

Figure 4.15 Trap levels on a C^+ domain introduced due to defects induced on the PZT surface mainly oxygen vacancies. E_v is the top of the valence band associated with oxygen 2p orbitals and E_c is the bottom of conduction band associated with titanium 3d orbitals. P_{sp} represents the direction of spontaneous polarisation.

The increase in defect concentration mainly oxygen vacancy concentration with respect to annealing temperature increases shallow level traps in the system, as shown in Figure 4.15. Upon UV irradiation photogenerated electrons get trapped in these shallow levels which have the effect of decreasing the energy required for activation of the electron to energy where it can perform chemistry and also increasing the lifetime of available electrons in the system. On a C^+ domain, these electrons are easily available for the photoreduction of Ag^+ to Ag^0. Therefore, with the increase in

shallow trap levels, more electrons are trapped that can participate in photoreduction reaction and therefore the rate of silver reduction reaction is higher. This results in an increase in silver deposition on the surface of C^+ domain. The higher flux of available electrons for photo reactions leads to the generation of particles of larger size and that is why a significant increase in the size of silver clusters on the C^+ domain can be seen. The average size of silver particles increased by about four times from 80-100 nm at 540 ºC to 350-400 nm on samples annealed at 690 ºC. In addition to this, the amount of photoreduced silver increased by more than 150% when the temperature of annealing increased from 540-690 ºC. On a C^- domain the negative polarisation charge at the surface and the direction of internal field does not allow the photoexcited electrons to reach the surface and participate in chemical reaction. That is the reason why no photoreduced silver was seen on the surface of negative domains.

The band structure at the surface of PZT is also changing due to the variations in annealing at higher temperatures. As discussed earlier that defects and free charge carriers contribute to internal screening and form the SCR at the surface. According to Xiao *et al.*[21], the width of SCR is inversely proportional to the effective space charge density (ρ) and is given by relation:

$$W \propto \sqrt{\frac{1}{\rho}} \quad \textbf{(Equation 4.9)}$$

An expression for ρ in a semiconductor can be given as

$$\rho = e\left(N_D{}^+ - N_A{}^- + p - n\right) \quad \textbf{(Equation 4.10)}$$

Where $N_D{}^+$ is the ionised donor density, $N_A{}^-$ is the ionised acceptor density, p is the hole concentration in the valence band, n is the electron concentration in the conduction band and e is electronic charge.

According to Equation 4.9, an increase in the defect concentration mainly oxygen vacancies will increase the space charge density eventually leading to a decrease in the width of SCR and a change in band structure at the surface. Despite the reduction in width of the SCR, it is sufficiently large to enable effective separation of photogenerated holes and electrons. SEM images of photoreduced silver on samples annealed at different temperatures are indication that the charge separation is not reduced but is enhanced considerably.

4.2.4 Conclusion

The influence of annealing PZT on the photochemical properties at the surface is shown. When the PZT samples were annealed in air at temperatures ranging from 540-690 °C, the silver deposition increased by more than 150%. This increase in photoreduced silver on the PZT surface is attributed to an increase in the defect concentration in the near surface region. This leads to a change in band structure at the surface due to the development of new trap and defect states.

4.3 Impact of Zr/Ti ratio in PZT on the photoreduction of silver

Many studies on the structural, electrical[22] and optical[23] properties of PZT films of different compositions have been reported but very limited information exists on the photochemical properties of different composition of PZT. The compositions used in this research are $PbZr_{0.3}Ti_{0.7}O_{3,}$ $PbZr_{0.52}Ti_{0.48}O_3$ and $PbZr_{0.7}Ti_{0.3}O_{3;}$ the crystallographic structure at room temperature according to the bulk phase diagram is tetragonal, coexistence of tetragonal and rhombohedral (morphotropic phase boundary) and rhombohedral respectively. The photochemical properties of PZT thin films of different compositions are investigated by carrying out the silver deposition

experiments using two UV lamps of different intensities. The nature and reasons behind the preferential growth of silver on patterned PZT are examined. Therefore, by tracking the change in the silver deposition a handle for understanding the impact of Zr/Ti ratio in the PZT on the photochemical reactivity at the surface is generated. The difference in deposition pattern is attributed to the difference in width of space charge region in the PZT samples of different compositions that impacts the band bending at the surface and the band gap of the samples.

4.3.1 Samples used

A 70 nm thick film of PZT (30/70) on $Pt/Ti/Si/SiO_2$, a 70 nm thick film of PZT (52/48) on $Pt/Ti/Si/SiO_2$ and a 70 nm thick film of PZT (70/30) on $Pt/Ti/Si/SiO_2$.

4.3.2 Experimental procedure

PZT films, with the Zr/Ti ratio of 30/70, 52/48 and 70/30 were prepared. Ready prepared sols[24] of the three compositions were used and the sample was processed according to previously published work[25] and gave PZT films that were 70 nm thick. Film orientation was determined using XRD measurement and the grain structure of PZT films was examined using TM-AFM. After poling the samples using PFM, they were dipped in silver nitrate solution and irradiated with a UV lamp for 20 minutes. Two UV lamps namely ‘H’ lamp and ‘F’ lamp were used in experiments; full spectrum of lamps is presented on page 53 (Figures 3.4 and 3.5). The samples were imaged using SEM and analysed using EDX technique. The experiments were repeated on five different PZT samples of each composition and same results were obtained on all samples of a composition.

4.3.3 Results and discussion

The growth of PZT films is nucleation controlled and the orientation of PZT films is based on the substrate used. A Platinum layer on silicon oxide has a preferred (111) orientation, and therefore the PZT thin films showed (111) orientation on platinum substrate[26]. However, grains of other orientation such as (100), (110) are also sometimes observed. XRD patterns of PZT (30/70), PZT (52/48) and PZT (70/30) are shown in Figure 4.16.

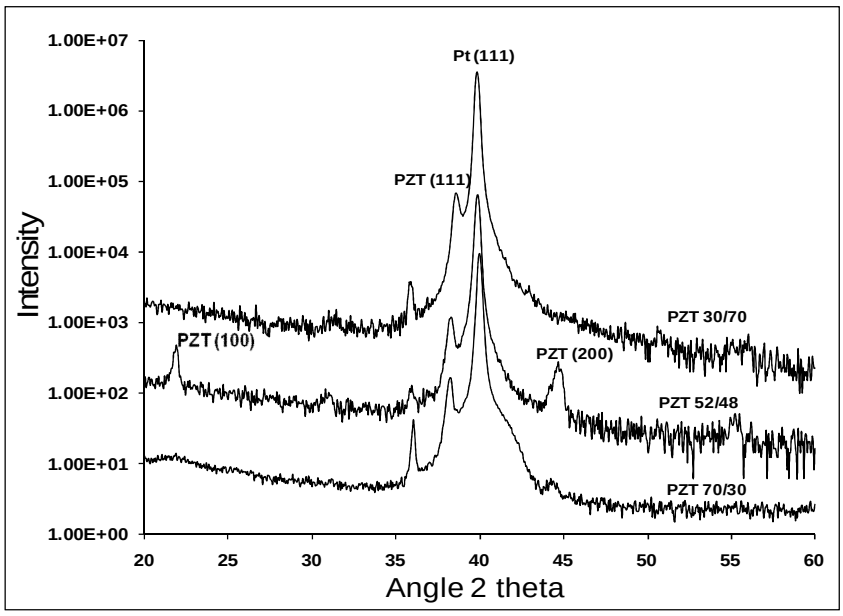

Figure 4.16 XRD patterns of PZT (30/70), PZT (52/48) and PZT (70/30).

The preferred orientation in all three films is calculated using the intensities of the (111), (100) and (110) peaks and the following equation:

$$I_{(xyz)} = \frac{I_{(xyz)}}{I_{(111)} + I_{(100)} + I_{(110)}} \qquad \textbf{(Equation 4.11)}$$

Upon comparison of relative intensities it was found that PZT (30/70) and PZT (70/30) are highly (111) oriented, whereas in PZT (52/48) about 30% of the crystals are (100) orientated and 70% are (111) orientated. The PZT samples have discrete grains with a random orientation across the surface before poling. As shown in Figure 4.17, the grain size in PZT 52/48 and PZT 70/30 is larger than the grain size in PZT

30/70; this is because the grain sizes of PZT films strongly depend on the composition ratio via different nucleation/growth energies. The films with high Ti content have smaller nucleation energy and therefore smaller size of the grains[27].

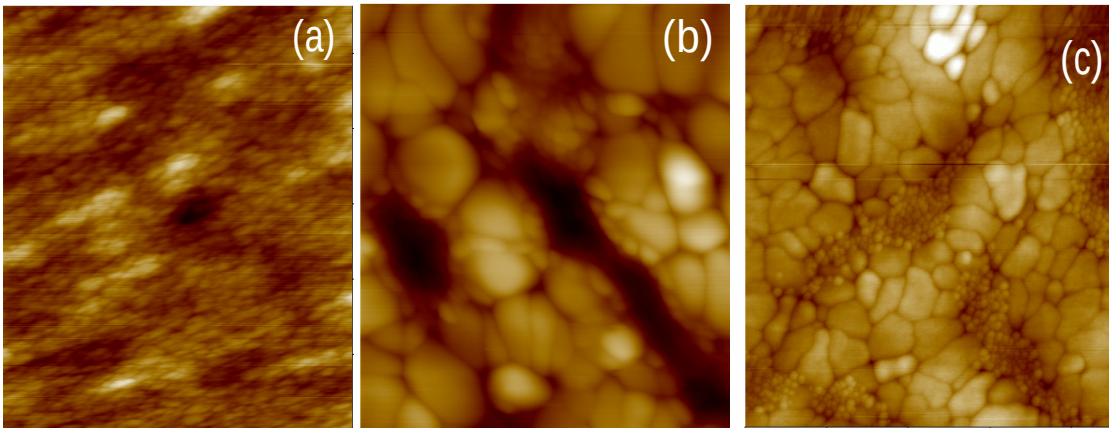

Figure 4.17 AFM image showing grain structure of (a) PZT 30/70, (b) PZT 52/48 and (c) PZT 70/30 thin films each of thickness 70 nm. The area covered in each image is 1.25 × 1.25 µm. The grain size in PZT 30/70 is much smaller than in PZT 52/48 and PZT 70/30.

4.3.4 Silver deposition on PZT 30/70 and PZT 52/48 using 'F' and 'H' lamp.

The SEM images of photodeposited silver on C^+ and C^- patterned PZT are shown in Figure 4.18.

Upon irradiation with the 'F' lamp both PZT 52/48 and PZT 30/70 showed deposition of silver only on C^+ domains and no deposition on C^- domains. However, when the 'H' lamp was used to irradiate the surface, silver deposition occurred on both C^+ domains and C^- domains of PZT 52/48; the size of silver particles on C^- domains is smaller and deposition is less dense compared to the C^+ domain. On the surface of PZT 30/70, only C^+ domains were covered in silver.

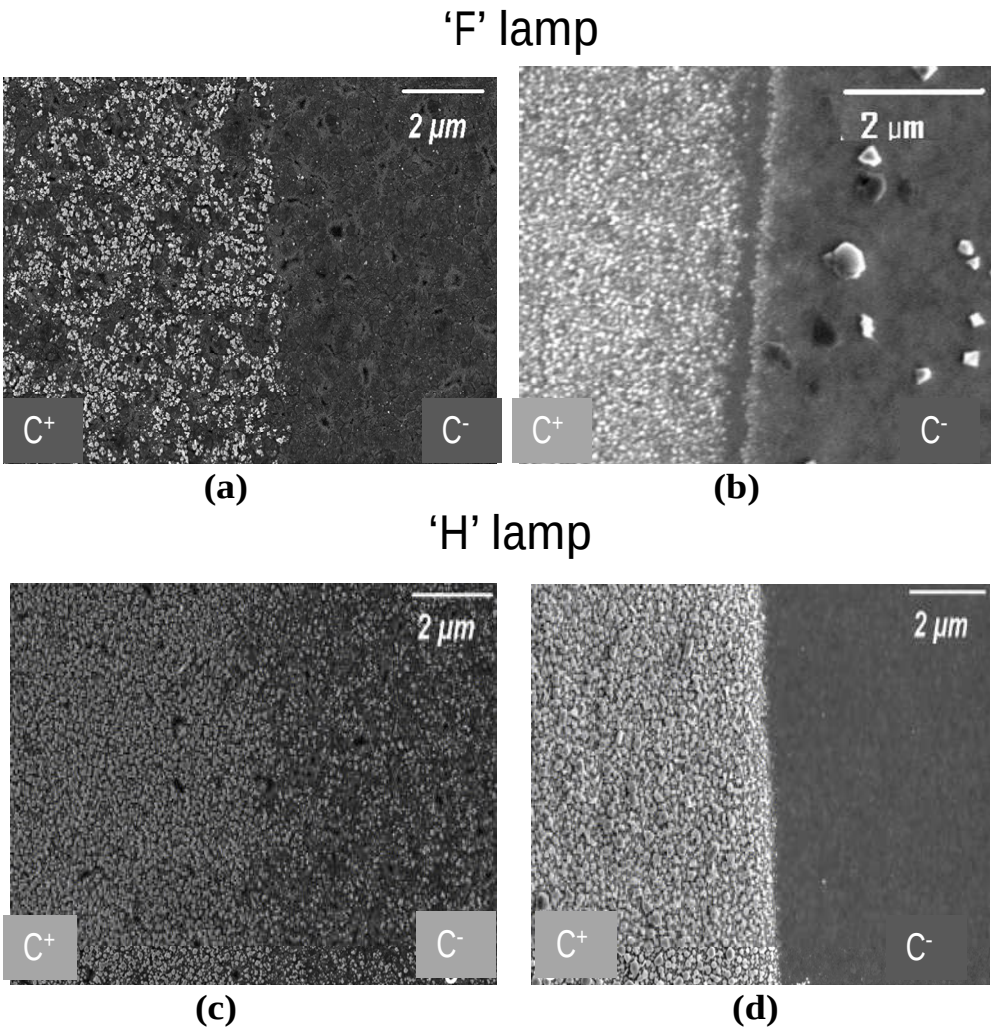

Figure 4.18 SEM images of silver deposition on (a) PZT (52/48) upon irradiation with 'F' lamp (b) PZT (30/70) upon irradiation with 'F' lamp (c) PZT (52/48) upon irradiation with 'H' lamp (d) PZT (30/70) upon irradiation with 'H' lamp

The photoreduction of silver on C^+ domain of PZT 30/70, following the band gap theory and strong band bending near the surface, has already been discussed in section 4.1. Preferential deposition of metal on the surface of a ferroelectric is found to be dependent not only on the polarization of the domain underlying the surface[28] but also on the surface defects such as grain boundaries[9], domain boundaries[8] and defects within the film. The energy of UV irradiation also influences the band structure and space charge layer at the surface; upon illumination with high energy, restructuring of bands at the surface and narrowing of space charge region has also been reported[29].

According to investigations by Pintilie *et al.*[30], on a set of $Pb(Zr_xTi_{1-x})O_3$ samples with different Zr/Ti ratios, the variation in the width of space charge layer at the surface is dependent on a number of factors including saturation polarisation (P_s), hole concentration p(T) and effective space-charge density in the depleted layer (N_{eff}) of the sample. P_s for PZT 55/45 and 30/70 is reported to be 31.1 μC/cm^2 and 16 μC/cm^2 respectively and the hole concentration is reported to be 2.2 ×10^{17} and 22×10^{17} cm^{-3} respectively. The thickness of the SCR is calculated to be 12.1 and 22.6 nm for PZT 55/45 and 30/70 respectively. Since PZT 55/45 and 52/48 both have nearly same composition, therefore it can be said that the width of SCR in both the samples would be roughly same. Hence, the SCR in PZT 52/48 is roughly half of the same in PZT 30/70. According to the above data, the band structure at the surface can be represented as shown in Figure 4.19. The position of the Fermi level is drawn towards the valence band in the above diagram because according to defect chemistry a non doped PZT film is a p-type of semiconductor[12].

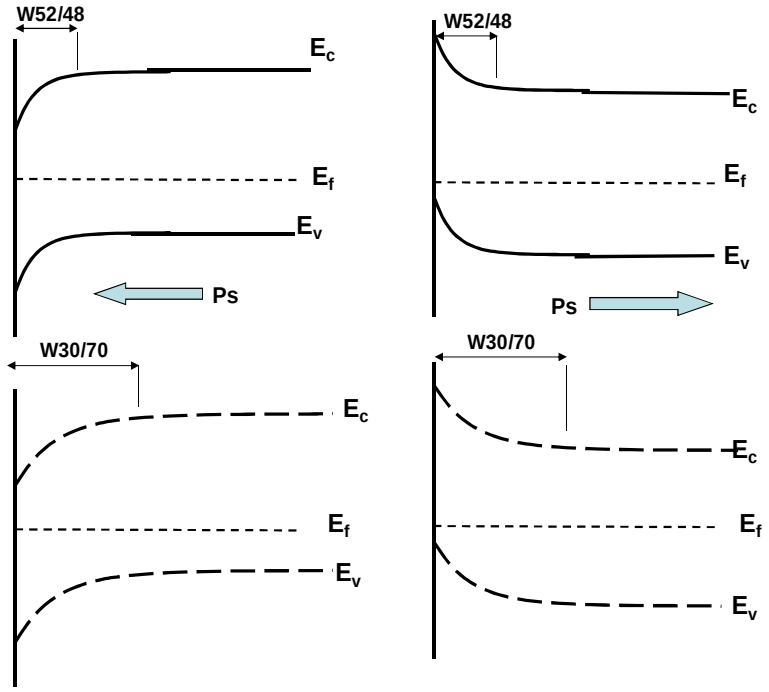

Figure 4.19 Band structure of PZT 52/48 (solid lines), and PZT 30/70 (dashed lines) on a C^+ and C^- domain where E_c is the conduction band, E_v is the valence band, E_f is the fermi level. P_s arrow

represents the direction of spontaneous polarisation. The W52/48 and W30/70 arrows represent the width of the SCR in both the samples.

When the surface of PZT (52/48) is irradiated with low energy 'F' lamp, reduction of silver occurs on the C^+ domains due to the availability of photoexcited electrons at the surface. The grains in the 52/48 sample are bigger in size (150-200 nm) as compared to 30/70 sample (grain size 70-100 nm), and therefore there are less nucleation points available on 52/48 sample for the growth of nanoparticles. This means that the deposited silver should be less dense and with bigger particle size as compared to PZT 30/70 sample which has smaller grains. SEM analysis shows that the silver deposition on the C^+ domain of 52/48 sample was less dense and with smaller particle size compared to the same on 30/70 sample. This can be attributed to the difference in the band gap of the two samples. The optical band gap energy of the PZT thin films is a composition dependent parameter and has been found to decrease with an increase in Ti content[31]. The band gap energy of PZT 52/48 is found to be higher than PZT 30/70[31]. Due to the higher band gap energy of PZT 52/48 sample, there is a reduced flux of photons capable of generating electron-hole pairs. This results in fewer photoexcited electrons available for chemical reaction. No silver deposition was seen on the C^- domains because the electric field in the SCR moved the photoelectrons away from the surface and the width of the SCR was large enough to prevent the electrons from penetrating it and reaching the surface.

When the 'H' lamp was used to irradiate the surface, an increased flux of photoexcited electron-hole pairs were generated; an increased availability of electrons in the conduction band for photoreduction leads to a significant increase in silver nanoparticle deposition on the surface of PZT 52/48 and PZT 30/70, Figure 4.18. The photogenerated electron-hole pairs also contribute to internal screening at the surface

resulting in a reduction in the width of SCR, eventually leading to a change in band structure at the surface[29], as shown in Figure 4.20.

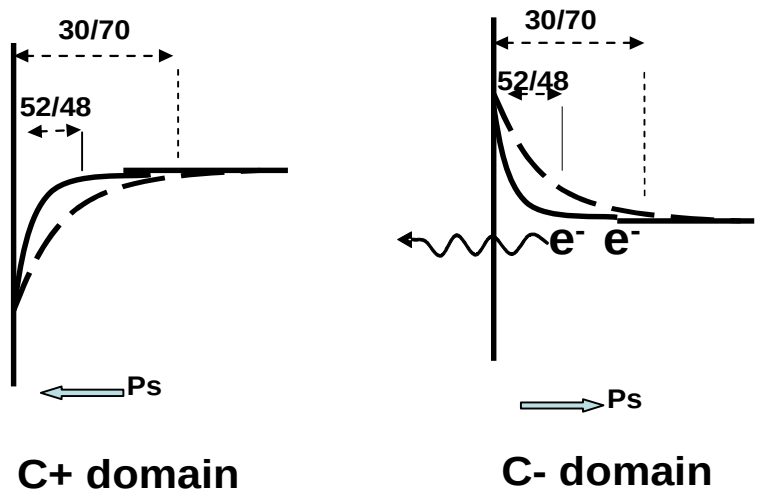

Figure 4.20 Change in band structure of PZT 30/70 and PZT 52/48 upon irradiation with high energy 'H' lamp. The arrows represent the reduced width of SCR on the surface of PZT and the wavy arrow represents electron tunnelling through the SCR on C^- domain of PZT 52/48.

This reduction in the width of SCR has a major impact on the photochemical reactivity of a surface. When the barrier, represented by the space charge region, is sufficiently narrow, tunnelling of electrons can occur at the semiconductor-electrolyte interface[32]. On a C^- domain, the shape of the space charge layer prevents efficient mobility of the electron into the solution and there is an energy barrier to the movement of the electron. But with the reduction in the width of SCR, electrons can tunnel across the SCR to react with cations present in solution, as shown in Figure 4.20. The variation in penetrability of the electrons across the potential barrier with respect to the width of SCR is given in Equation 4.12. In PZT 52/48, the width of SCR is relatively less (50% to that on a 30/70 sample) and is further reduced upon exposure to high energy UV lamp. In order to penetrate across the SCR, the photoexcited electrons have to travel a smaller distance (half the distance as compared

to PZT 30/70). As a result, the probability of photoexcited electrons tunnelling across the negatively charged surface and getting photoreduced to produce Ag^0 is increased.

The penetrability T of a barrier of height E and width w can be calculated approximately by[33]:

$$T = e^{-2\alpha w} \qquad \textbf{(Equation 4.12)}$$

$$\alpha = \frac{1}{\hbar}\sqrt{2mE} \qquad \textbf{(Equation 4.23)}$$

Where $\hbar$ is the Quantum of angular momentum = 1.05×10^{-34} kg-m^2/sec, m is the electron mass = 9.1×10^{-31} kg, w is the width of SCR and is 12.1 and 22.6 nm for 52/48 and 30/70 respectively.

The potential barrier E for PZT (52/48) and PZT (30/70) is 1.09eV and 1.37eV respectively. According to Equations 4.12 and 4.13, the penetrability across the C^- domain of PZT 52/48 ($T_{52/48}$) and PZT 30/70 ($T_{30/70}$) is:

$$T_{52/48} = 4.17\times10^{-57} \text{ and}$$

$$T_{30/70} = 8.65\times10^{-119}$$

This means that the probability of electrons penetrating across the SCR of PZT (52/48) is significantly higher than that across the SCR of PZT (30/70). Also, upon irradiation with higher energy photons, for every 1 nm decrease in the SCR of both the samples, the penetrability increases by a factor of 10^5 and 10^6 in PZT 52/48 and 30/70 respectively. In a PZT 52/48 sample, the high penetrability across the SCR due to the reduction in the width of SCR results in deposition of silver on both C^+ and C^- domains. However, due to the negative polarisation charge present on the surface of the C^- domain and the electric field associated with this polarisation charge, the actual number of electrons tunnelling across the potential barrier is greatly reduced. As a result of this, the amount of photoreduced silver present on C^- domain is significantly less as compared to that on the C^+ domain in PZT 52/48.

4.3.5 Silver deposition on PZT 70/30

The C^+ and C^- patterned PZT 70/30 surface was immersed in silver nitrate solution and placed inside the UV box fitted with the 'H' lamp and irradiated for 20 min. The SEM image of photo deposited silver is shown in Figure 4.21. Silver deposition is observed on both C^+ and C^- domains.

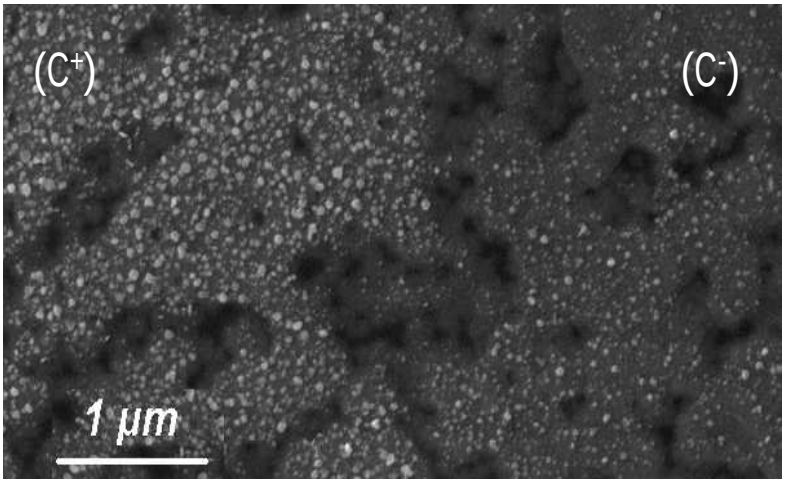

Figure 4.21 SEM image showing silver deposition on both C^+ and C^- domains of PZT 70/30.

On a C^+ domain, due to downward band bending, electrons are forced to migrate towards the surface[7] where they react with silver cations and are reduced to metal. On the C^- domain, silver deposition could again be due to the change in band structure upon irradiation with high energy lamp, as discussed in section 4.3.1. The photogenerated electron-hole pairs contribute to internal screening at the surface and reduce the width of SCR. On the C^- domain, with the reduction in the width of SCR, electrons can tunnel across the SCR and react with silver cations in solution. Upon comparing the amount of photoreduced silver on all three PZT compositions keeping the other factors e.g. salt solution concentration and UV exposure time constant, it was found that the amount of deposited silver on PZT 70/30 surface is less than on PZT 52/48 and 30/70. This could again be due to the increase in the band gap of PZT thin films with the increase in Zr content[31]. Therefore, it can be said that PZT 30/70

thin films are most efficient in reducing metal from metal cations in the solution as compared to other compositions.

4.3.6 Conclusion

The photochemistry of PZT thin films of different compositions was investigated and it was found that a variation in the Zr/Ti ratio has an influence on the photochemical reactivity of the material. The influence of semiconducting properties of PZT on the photochemical/physical properties was also shown. The variation in the space charge region at the surface, the band gap of the two samples, and the energy of incident irradiation were found to have an influence on the photochemistry at the surface.

4.4 Impact of size of poled pattern on metal growth

4.4.1 Experiments

A 70 nm thick film of PZT 30/70 was made and the film orientation was determined using XRD measurement. Patterns of size ranging from 1×1 μm to 80×80 μm were poled using the PFM and larger areas (>100×100 μm) were poled using corona poling. The C^+ poled patterns of smaller dimensions 2 μm ×250 nm, 2 μm ×400 nm, 3 μm ×100 nm were poled using PFM. After poling the samples were dipped in silver nitrate solution, irradiated with 'H' lamp for 20 minutes, and finally imaged using SEM.

4.4.2 Results and discussion

Silver deposition was carried out on C^+ poled patterns of sizes 1×1 μm, 80×80 μm and 5 ×5 mm. The SEM images of silver deposition on 1×1 μm and 5 ×5 mm poled patterns are shown in Figure 4.22.

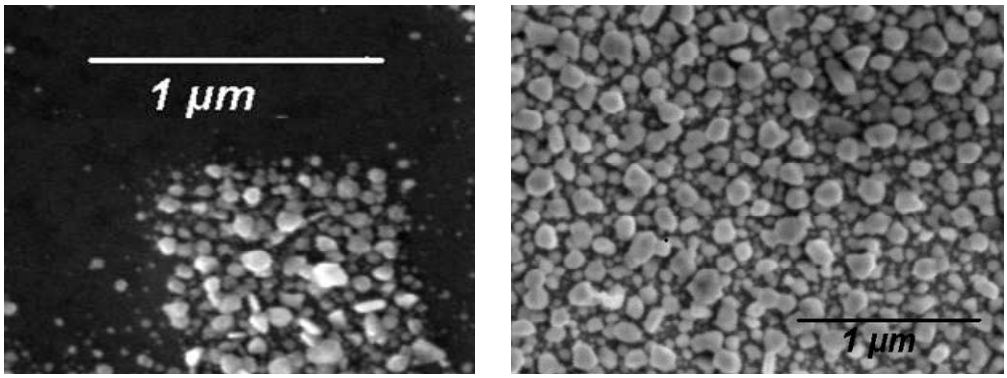

Figure 4.22 SEM image of photoreduced silver on C^+ pattern of sizes (a) 1×1 µm (b) 5 ×5 mm

The pattern of silver deposition, along with particle size and density, were analysed on all the three poled areas using the SEM. No correlation between size and density of photoreduced silver and size of poled pattern was found. In all the cases, silver deposited as discrete particles and covered the entire C^+ domain leaving the C^- domain clear. The same experiments were done on C^+ poled patterns of smaller dimensions; 2 µm lines of width 400 nm and 250 nm were poled on the same PZT surface and silver deposition was carried out on them. SEM image of silver deposition is shown in Figure 4.23(a) and (b). On the 400 nm wide C^+ pattern, the size of silver particles ranges from 10 nm to 105 nm, whereas on the 250 nm wide C^+ pattern the size of silver particles ranges from 10 nm to 45 nm. Therefore, the size of silver particles on 400 nm wide C^+ domain was observed to be bigger (more than double) than that on 250 nm wide domain. This phenomenon is better visualised by the AFM image that shows the formation of a silver nanowire on PZT surface, Figure 4.24.

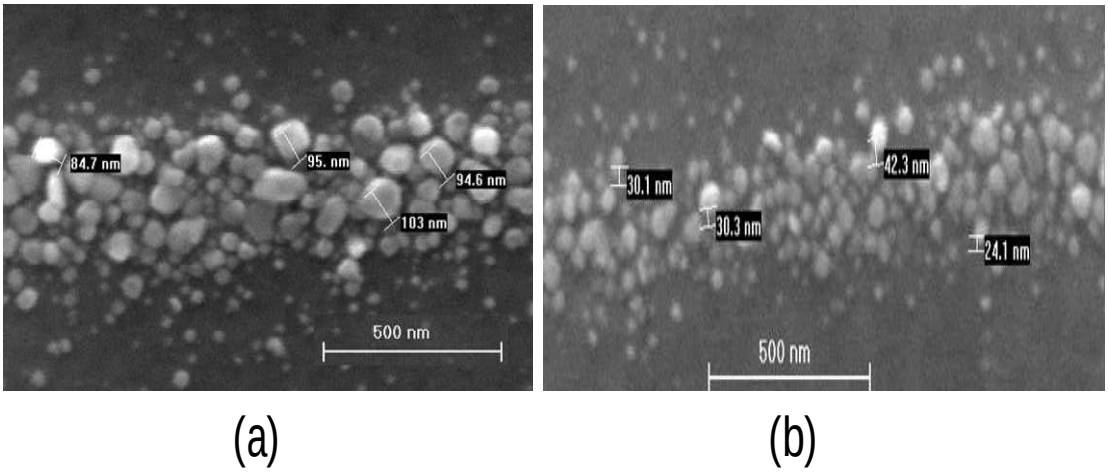

Figure 4.23 SEM image of silver deposition on C^+ domain of width approximately (a) 400 nm and (b) 250 nm. The size of silver particles ranges from (a) 10 nm to105 nm and (b) 10 nm to 45 nm.

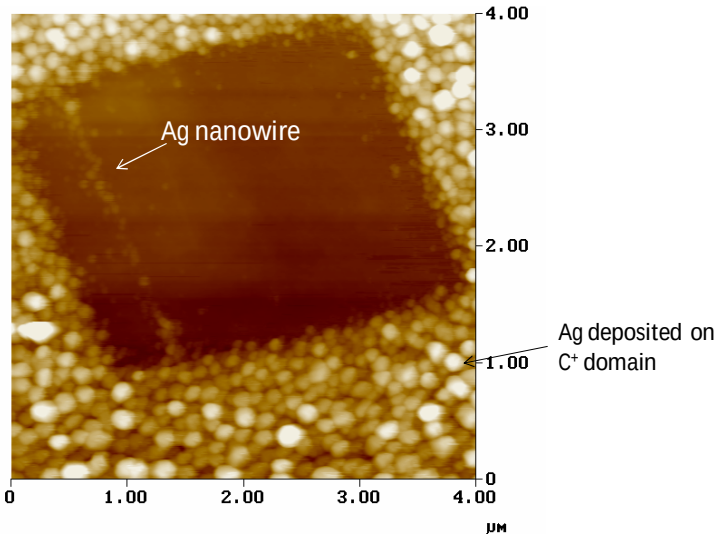

Figure 4.24 AFM image showing formation of silver nanowire on C^+ domain of PZT surface. The dark area in the image is C^- domain and the surrounding area covered with silver particles is C^+ domain.

On a PZT surface, a C^+ domain of 5 × 5 µm was poled and inside this area a C^- domain of 3× 3 µm was poled. Furthermore, inside the 3× 3 µm C^- domain, a C^+ domain of 3 µm ×100 nm was poled. Silver deposition was carried out on the poled pattern and the sample was analysed under the SEM. Silver deposition was observed on the outside C^+ domain and a nanowire of silver was formed on the 3 µm ×100 nm C^+ domain. In Figure 4.24, the AFM image shows that the size of silver nanoparticles

on the 100 nm wide pattern is much smaller than the silver deposited on the surrounding C^+ area. It is observed that in the case of smaller domains (smaller than 1 μm) the size of deposited silver particles and amount of photoreduced silver decreases as the size of domain decreases. With the decrease in pattern size, the flux of photogenerated electron-hole pairs is reduced, leading to a lower number of electrons available for photochemistry. In addition to this, for thin domains the inhomogeneous distribution of the electric field in the vicinity of the domain wall[8] and interfaces[9] plays an important role. The electric field leads to the depletion of mobile electrons from the surrounding region and electrons migrate to the side boundaries due to the space charge region and strong band bending, as shown in Figure 4.25 (left). As a result less number of electrons will be able to reach the surface for photochemistry, (Figure 4.25 (right)) thereby reducing the amount of photoreduced silver on the surface.

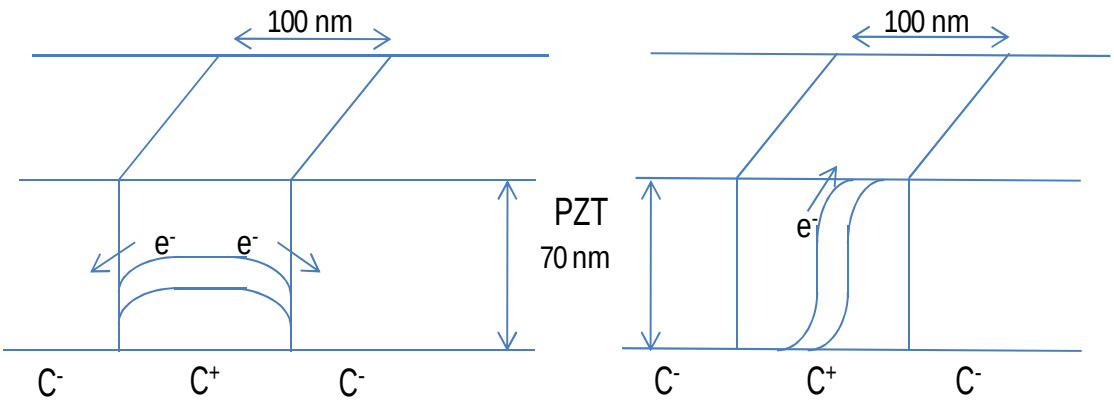

Figure 4.25 Diagram showing SCR and electron migration in side boundaries of thin domains (left) depicting SCR and electron migration at the top surface (right).

The same phenomenon is insignificant on domains of larger size because, despite the charge carrier migration to side boundaries, there still will be a great flux of photo carriers reaching the surface for photochemistry.

4.5 Gold nanoplates formation

4.5.1 Experimental procedure

Two 70nm thick films of PZT (30/70) were prepared and patterns were poled on the two films in the form of squares of C^+ and C^- domains using the PFM. Fresh 0.001 and 0.0001 M gold chloride solutions were prepared and filtered using a 0.2 μ m filter. The PZT samples were placed in Petri-dishes containing different gold chloride solutions and were exposed to 'H' lamp for 45 minutes. After irradiation, the PZT samples were taken out of the salt solution, rinsed with de-ionised water and blow dry with nitrogen. The samples were then analysed for gold deposition under the SEM and TM-AFM.

4.5.2. Results and discussion

A SEM image of the PZT surface following gold deposition using a 1×10^{-3} M $HAuCl_4$ solution is shown in Figure 4.26(a). Deposition of Au particles has occurred randomly over the PZT surface irrespective of C^+ and C^- domains. The gold particles were in different sizes ranging from few hundred nanometers to about 4 μm. As seen in the SEM image in Figure 4.26, there are spherical gold particles that are few hundred nanometers in size and there are some triangular and hexagonal nanoplates with edge length approximately 4 μm and 2 μm respectively. We are calling them nanoplates because the thickness of these plates is about 80 ± 10 nm (as determined by AFM). EDX analysis of these plates and clusters show a high percentage of gold in them and therefore the possibility that these triangular and hexagonal shaped particles are made of impurities is ruled out.

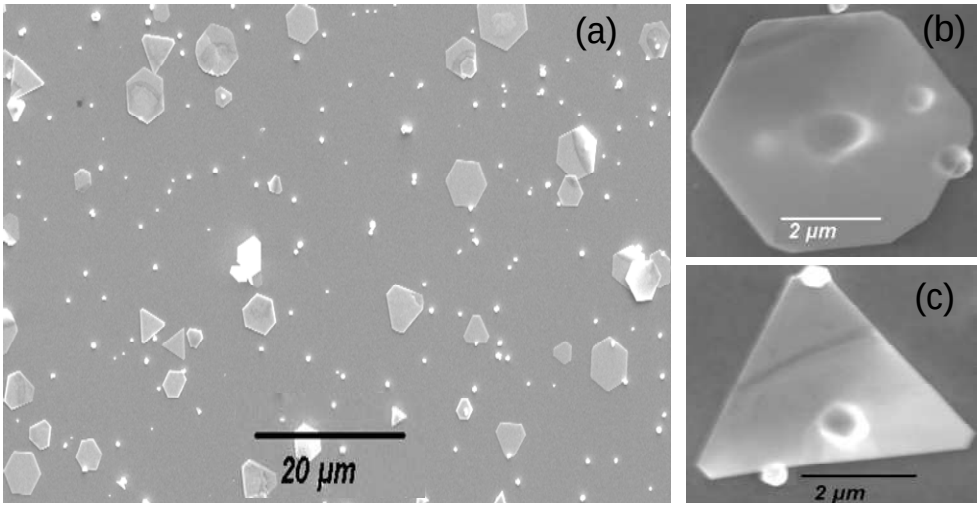

Figure 4.26 SEM image of (a) gold deposition using a 1×10^{-3} M $HAuCl_4$ solution; the photoreduced gold is spherical, triangular and hexagonal in shape and is independent of the polarity of underlying domain (b) triangular and hexagonal nanoplates have edge length approximately 4 µm and 2 µm respectively and thickness of roughly 80 nm.

There are several studies reporting the formation of triangular and hexagonal nanoplates and nanowires by reduction of gold[34, 35] from gold chloride solution. In all of these studies, a reducing agent was added to the gold chloride solution to facilitate the reduction reaction but in our work a solution of $HAuCl_4$ and de-ionised water was used for reaction.

The formation of triangular and hexagonal nanoplates from the solution of $HAuCl_4$ salt and de-ionised water on a ferroelectric surface was first reported by Kalinin *et al.*[36] in 2002. Hanson *et al.*[37] also reported the formation of similar gold structures on ferroelectric lithium tantalate but the mechanism of formation of gold structures was not suggested. In both the above studies, the deposition of gold was independent of polarisation of underlying domain.

The observed pattern of gold deposition is in-line with the results seen by research groups before[36, 37]. On the PZT surface, photoreduced gold was not selectively depositing on any domain and the entire surface was covered with particles of

different shapes and sizes. The mechanism of formation of clusters, and triangular and hexagonal nanoplates of gold could be the same as discussed in section 4.1. Irradiation with UV light greater than the band-gap of PZT leads to the formation of electron-hole pairs. These photogenerated electrons are reacting with gold cations in the solution leading to the deposition of metallic gold on the surface.

In order to further investigate the mechanism behind gold deposition, the same experiment was performed on a piece of glass slide instead of PZT. A drop of gold chloride solution was placed on a glass slide and it was irradiated with UV light for the same amount of time. SEM analysis showed that similar triangular and hexagonal gold plates were formed on the glass slide. Therefore, the theory proposed by previous studies about the formation of these gold plates on ferroelectric surface can not be true. It is proposed that the gold nanoplates are forming at the air-water interface through the reduction of $HAuCl_4$ in the presence of ultraviolet light and then settling down on the surface of PZT. This explanation is further supported by the work by Chen *et al.*[38] in which they produced gold nanoplates by reducing $HAuCl_4$ in the presence of UV light, and found that the reaction was dependent on the photogenerated electrons from the Teflon dish in which the reaction was performed.

The same experiments were performed with solutions of 1×10^{-4} M, 1×10^{-3} M, 1×10^{-2} M concentrations. It was found that when lower concentration of gold chloride solution was used spherical nanoparticles were predominantly formed and few triangular, hexagonal nanoplates were formed. As the molar concentration of solution is increased, more triangular, hexagonal plates are formed reducing the amount of spherical gold particles. Our results are in agreement with the work done by Ibano *et al.*[39], who have shown the dependence of concentration of gold salt solution on the deposition of gold.

4.6 Metal deposition around PZT islands created using focused-ion–beam technique

Recently, there has been an increasing interest in the study of size effects in ferroelectric thin films. Researchers have been trying to investigate the smallest size at which a ferroelectric structure can possess switchable remnant polarisation[40]. The purpose of this study was to investigate the smallest size of ferroelectric island or structure at which it can perform photochemistry. A top-down approach was used in this process; focused-ion-beam method was used to structure small islands of PZT on a dense PZT thin film.

4.6.1 Experimental procedure

A 70 nm thick film of PZT (30/70) was made and processed using the same technique described in previous sections. Film orientation was determined using XRD measurement. Islands of size ranging from 300×300 nm to 2×2 μm were fabricated via focussed ion beam milling. The PZT structures were then cleaned using Acetone and Iso-Proponal Alcohol, and finally rinsed with de-ionised water and blow dry with N_2. The samples were dipped in silver nitrate solution, irradiated with 'H' lamp for 20 minutes, and finally were imaged using SFEG and analysed using EDX.

4.6.2 Results and discussion

A typical AFM image of fibbed islands on PZT surface is shown in Figure 4.27. The four PZT islands shown in the AFM image are roughly 2×2 μm in size and their height is approximately 100 nm.

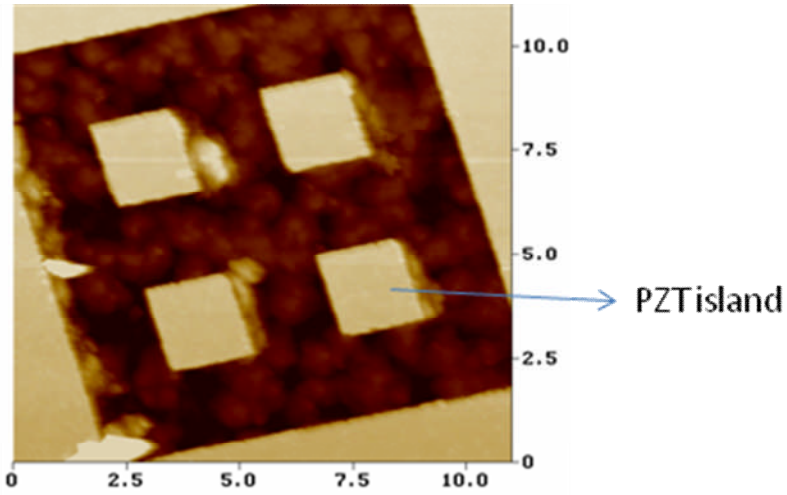

Figure 4.27 A typical AFM image of the fibbed structures on PZT. The scale bar is in µm.

SEM image after silver deposition is shown in Figure 4.28(a), which shows that no silver is deposited on islands and the surrounding region of milled area, whereas normal silver deposition has occurred on PZT surface away from the milled region. A magnified image of one of the islands is shown in Figure 4.28(b) which emphasises the absence of any feature of deposited silver on the surface.

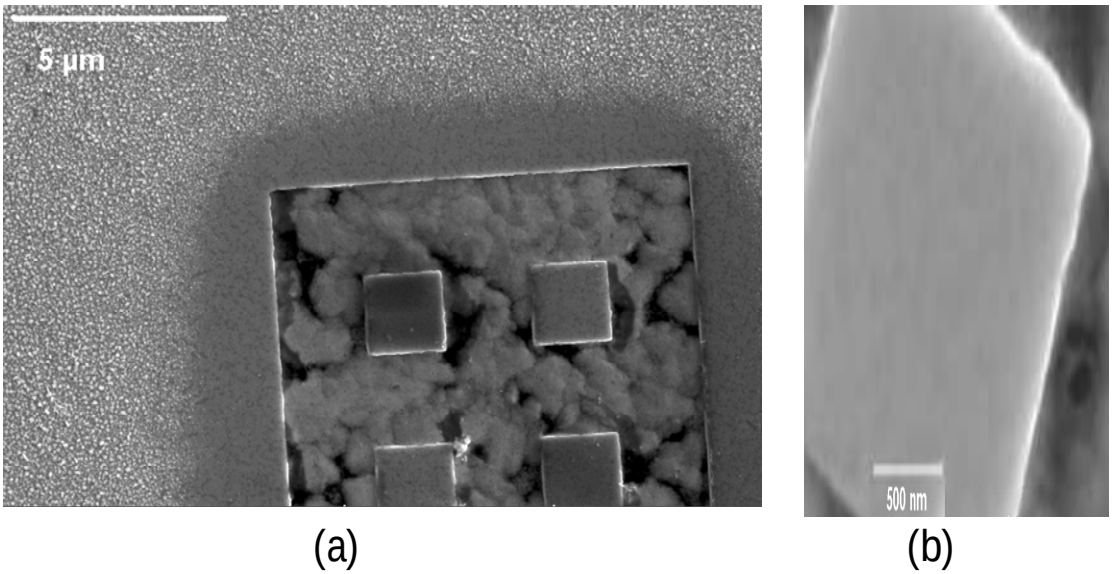

Figure 4.28 (a) SEM image of fibbed structure after silver deposition. There is no silver deposition on the PZT islands and the surrounding region of milled area whereas normal silver deposition has occurred on PZT surface away from the milled region (b) A magnified image of one of the caps; note the absence of any feature of deposited silver on the surface

EDX analysis did not show any trace of silver on the islands and the surrounding milled region. The reason for no silver deposition on fibbed PZT islands could be the damage of PZT area exposed to high energy Ga^+ focused ion beam during milling. Stanishevsky *et al.*[41] have reported that exposure of a PZT material to 50 kV Ga^+ ion beam significantly changes the composition of surface layer. The surface layer was found to be composed of up to 50% Ga, and oxygen and lead composition was severely reduced. Due to the modification of surface layer, the actual amount of ferroelectric material in the fabricated PZT structure is greatly reduced. The patterned PZT islands have been found to exhibit either strongly distorted hysteresis loops or no ferroelectric properties[42]. Recovery of ferroelectricity in some portion of the damaged layer after annealing in O_2 at 600 ºC has been reported[41]. The PZT sample with fibbed structures was further annealed in O_2 atmosphere at 600 ºC for 2 hours and Ag deposition experiments were performed on them. Annealing also did not change the situation and no trace of photoreduced silver was found on the islands and surrounding region.

Therefore, it can be said that with the top-down approach it is difficult to investigate the impact of size effects on the photochemistry of a material because of the effects induced during processing. The bottom-up approach can be a better option because it does not need processing of the material.

References

[1] M. E. Lines and A. M. Glass, *Principles and Applications of Ferroelectric and Related Material*, Clarendon Press, Oxford (1977)

[2] S. V. Kalinin, D. A. Bonnell, T. Alvarez, X. Lei, Z. Hu, R. Shao and J. H. Ferris *Adv. Mater.*, 16, 795-799 (2004)

[3] S. K. Pandey, A. R. James, R. Raman, S. N. Chatterjee, A. Goyal, C. P. Goel, *Phys. B* 369, 135-142 (2005)

[4] T. Markvart 2000 , *How Solar cells work, in Solar cells* 2nd edition , John Wiley and sons, Chichester, 29-34, (2000)

[5] X. Y. Zhu, *Annu. Rev. Phys. Chem.*, 45, 113(1994)

[6] Y. V. Pleskov and Y. Y. Gurevich, *Semiconductor photoelectrochemistry* 1st ed, Consultants Bureau, New York (1986)

[7] S. V. Kalinin and D. A. Bonnell, *Nanoscale Phenomenon in Ferroelectric Thin Films*, Kluwer Academic Publishers, Dordrecht (2004)

[8] J. N. Hanson, B. J. Rodriguez, R. J. Nemanich and A. Gruverman, *Nanotechnology*, 17, 4946-9, 10-14(2006)

[9] P. M. Jones and S. Dunn, *Nanotechnology*, 18, 185702 (2007)

[10] M. Dawber, K.M. Rabe and J.F. Scott, *Rev. Mod. Phys*., 77, 1083 - 1130 (2005)

[11] S. Yugang and X. Younan , *Science*, 298, 5601, 2176 – 2179 (2002)

[12] J. F. Scott, *Ferroelectric Memories*, Springer, New York (2000)

[13] W. Yang, B. J. Rodriguez, A. Gruverman and R. J. Nemanich, *Appl. Phys. Lett*., 85, 2316-2318 (2004)

[14] I. Boerasu, L. Pintilie, M. Pereira, M. I. Vasilevskiy and M. Gomes, *J. Appl. Phys*., 93, 4776-4783 (2003)

[15] J. C. Tauc, *Amorphous and Liquid Semiconductor,* Plenum Press, New York, p. 159 (1974)

[16] D. M. Smyth, *Curr. Opin. Solid State Mater. Sci.,* 1, 692-697 (1996)

[17] S. Agrawwal and R. Ramesh, *Annu. Rev. Mater. Sci.,* 28, 463-499 (1998)

[18] F. Ayguavives, A. Agius, B. Kim and I. Vickridge, *J. Mater. Res.,* 16, 3005-3008 (2001)

[19] J. Robertson and W. L.Warren, *Proceedings of the 1994 MRS Fall Meeting*, 123-128 (1995)

[20] F Chen *et al., J. Phys.: Condens. Matter.,* 17 L467–L475 (2005)

[21] Y. Xiao, *The influence of oxygen vacancies on domain patterns in ferroelectric perovskites,* PhD thesis, California Institute of Technology, California (2004)

[22] Y. Xu, *Ferroelectric Materials and their Applications,* Amsterdam, Elsevier Science Pub Co. (1991)

[23] S. Trolier-McKinstry, J. Chen, K. Vedam and R. E. Newnham, *J. Am. Ceram. Soc*., 78, 1907-1913 (1995)

[24] Q. Zhang and R. W. Whatmore, *J. Phys. D: Appl. Phys*., 34, 2296-2301 (2001)

[25] J. M. Marshall, S. Corkovic, Q. Zhang, R. W. Whatmore, C. Chima-Oreke, W. L. Roberts, A. J. Bushby and M. J. Reece, *Integ. Ferr.,* 80, 77-85 (2006)

[26] S. Dunn and R. W. Whatmore, *J. Eur. Ceram. Soc.,* 22, 825-833 (2002)

[27] K. Matsuura, K. Takai, T. Tamura, H. Ashida and S. Otani, *IEICE Trans. Electron*. E81-C, 528-536 (1998)

[28] J. L. Giocondi and G. S. Rohrer, *Chem. Mater*., 13, 241-242, (2001)

[29] S. Dunn, P. M. Jones and D. E. Gallardo, *J. Am. Chem. Soc.,* 129, 8724-8728 (2007)

[30] L. Pintilie, I. Boerasu, M. J. M. Gomes, T. Zhao, R. Ramesh and M. Alexe, *J. Appl. Phys.*, 98, 124104-124112 (2005)

[31] S. Yang, D. Mo and X. Tang, *J. Mater. Sci*., 37, 3841-3845 (2002)

[32] J. Ulstrup, *Surf. Sci.*, 101, 564-582 (1980)

[33] A. P. French and E. F. Taylor, *An Introduction to Quantum Physics*, Anonymous London, Chapman & Hall (1995)

[34] X. Sun and Y. Luoa, *Mater. Lett.*, 60, 24, 2988-2990 (2006)

[35] D. Li, J. McCann, M. Gratt and Y. Xia, *Chem. Phys. Lett.*, 394, 387–391(2004)

[36] S.V. Kalinin, D. A. Bonnell, T. Alvarez, X. Lei, J. H. Ferris, S. Dunn, Q. Zhang, *Nanoletters*, 2, 589 (2002)

[37] J Hanson, *Domain Patterned Ferroelectric Surfaces for Selective Deposition via Photochemical Reaction*, PhD thesis, North Carolina State University (2007)

[38] H. Chen, J. Jia, and S. Dong, *Nanotechnology* 18, 245601 (2007).

[39] D. Ibano, Y. Yokota and T. Tominaga, *Chem. Lett.*, 32, 574 (2003)

[40] A. Roelofs and T. Schneller, K. Szot and R. Waser, *Appl. Phys. Lett.*, 81, 27 (2002)

[41] A. Stanishevsky, B. Nagaraj, J. MeIngailis, R. Ramesh, L. Khriachtchev and E. McDaniel, *J. Appl. Phys*., 92, 3275 (2002)

[42] A. Stanishevsky, S. Agrawwal, A. S. Prakash and R. Ramesh, *J. Vac. Sci. Technol. B* 16, 3899 (1998)

5. Metal reduction and molecular adsorption on ferroelectric lithium niobate

There has been a growing interest in the study of the photophysics and photochemical interactions of ferroelectric materials since the late 1990's. Gioncondi and Rohrer[1] demonstrated that it was possible to spatially separate the reduction and oxidation processes on the surface of a ferroelectric. This was resolved by examining the influence of the internal dipole of a poled ferroelectric on the space charge layer and has led to a number of publications highlighting the influence of semiconductor physics on the surface photochemistry of ferroelectric systems[2,3]. Lithium niobate (LN) has gained considerable interest in this area because of its unique properties; it possesses a high magnitude of spontaneous polarisation at room temperature, which is of the value of $78 \pm 3 \mu C/cm^{-2}$, a high Curie temperature of 1140 ºC and due to the location of its conduction band (E_c) and valence band (E_v) with respect to Normal Hydrogen Electrode (NHE).

In this chapter, photochemical and photoelectric cation reduction on LN surface is demonstrated. The impact of composition of LN and energy and intensity of the incident photon on the photochemical reactivity of LN are investigated. It is shown that it is possible to photoreduce Al and Mn salts into respective metals onto the C^+ domain of LN. Selective adsorption of molecules of opposite charge on LN surface is also demonstrated.

5.1 Photochemical and photoelectric cation reduction on $LiNbO_3$

Silver cation reduction on C^+ and C^- domains of LN by photochemical and photoelectric process is demonstrated in this section. The reduction of the photoelectric threshold for C^- domain of LN, due to the polar nature of the crystal, allows high energy UV irradiation to produce free electrons that can participate in photochemical reduction of silver nitrate on the surface. This is in addition to the previously understood phenomenon of domain directed photophysics, where influences on space charge layer due to the internal dipole of a ferroelectric determine the carrier at the surface. It is shown that the interaction of photoelectric and domain dependent influences can be observed in LN due to the low electron affinity between 1.1-1.5 eV.

5.1.1 Experimental procedure

The sample used in this work was a single crystal congruent $LiNbO_3$ (LN) that has been poled to present either C^+ or C^- faces. A sample of size $0.25cm^2$ was dipped in freshly made silver salt solution and was placed directly underneath the 'H' lamp, this gives an irradiation from 200nm to the band gap energy of the $LiNbO_3$ at *ca* 320nm[5]. After illumination, the sample was rinsed with de-ionised water, blow dry with nitrogen, and adhered to a glass slide using double sided Carbon tape. The samples were then immediately analysed using an AFM in tapping mode (TM-AFM) to investigate the LN surface before and after irradiation with the UV.

5.1.2 Results and discussion

A TM-AFM topographic image of LN surface before irradiation is shown in Figure 5.1, the image shows that the surface of LN was smooth and no surface features

within a z-scale of 3 nm were observed. Figure 5.2 (left) shows the coverage of silver nanoparticles as deposited on the C^+ domain of the LN. A magnified AFM image of silver nanoparticles is shown in Figure 5.2 (right). The average size of Ag nanoparticles is 7 nm (as determined by the 'Particle Analysis' function in AFM software). EDX of LN surface is shown in Figure 5.3; Presence of Ag peak at 2.6 and 2.9 eV confirms the presence of Ag on the surface.

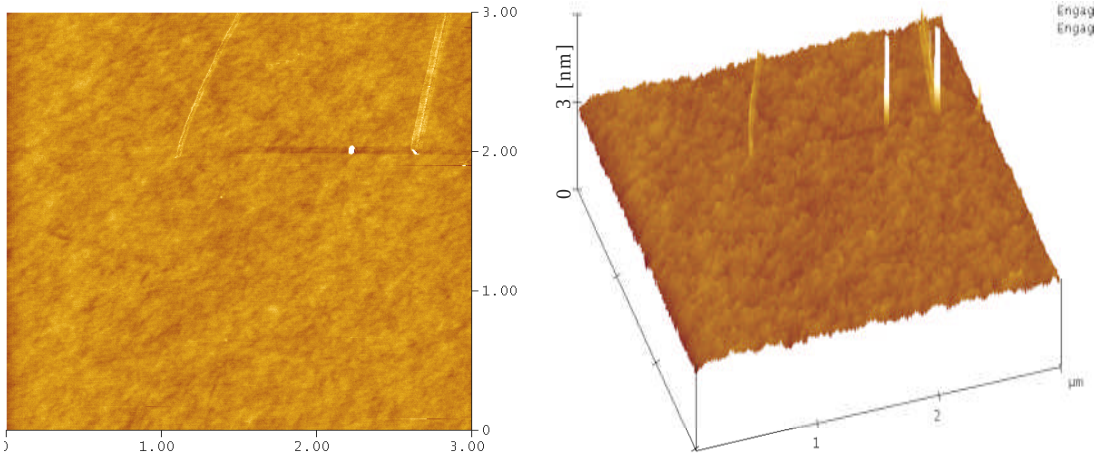

Figure 5.1 TM-AFM topographic image (left) and 3-D image (right) of the surface before experiments, shows no surface features within a z scale of 3 nm.

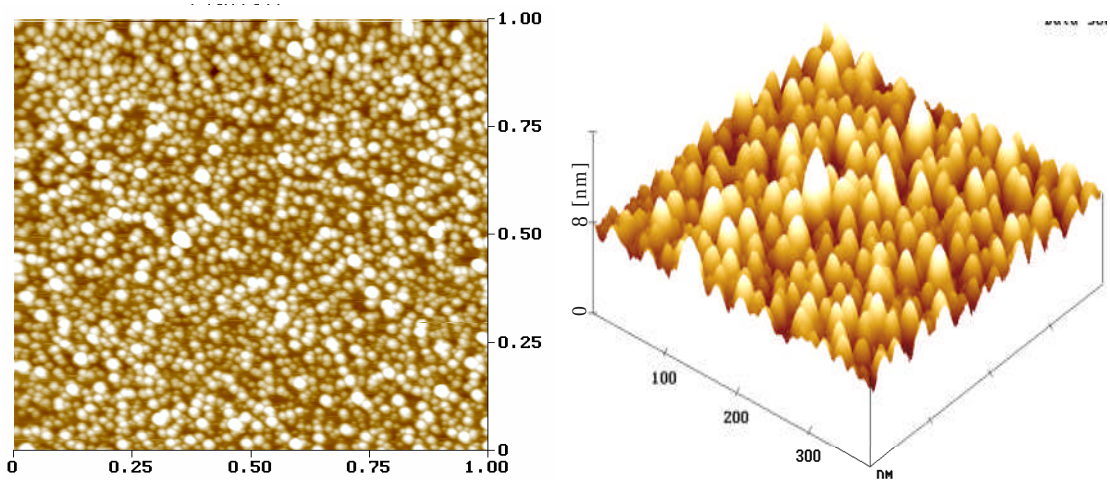

Figure 5.2 TM-AFM topographic image (left) of C^+ domain showing silver deposition in an area of 1×1µm. The 3-D image (right) of C^+ domain is magnified image covering an area 350×350 nm.

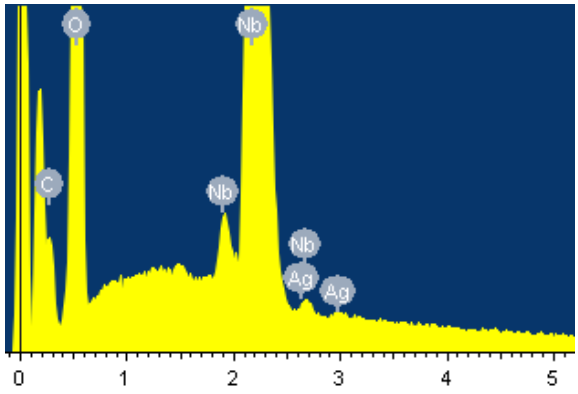

Figure 5. 3 ESEM-EDX of lithium niobate surface containing silver. Note the presence of silver peaks at 2.6 and 2.9 eV.

The same experiment was performed on the C^- face of the LN crystal, the results of which are shown in Figure 5.4. TM-AFM image of C^- surface shows the presence of photoreduced silver. This result is different from the previously reported studies where deposition occurred on the positive surfaces of the domains and domain boundaries. The size and distribution of the clusters on C^- domain is identical to the initial stages of metal cluster deposition on C^+ domain. EDX analysis of C^- domains confirms the presence of Ag.

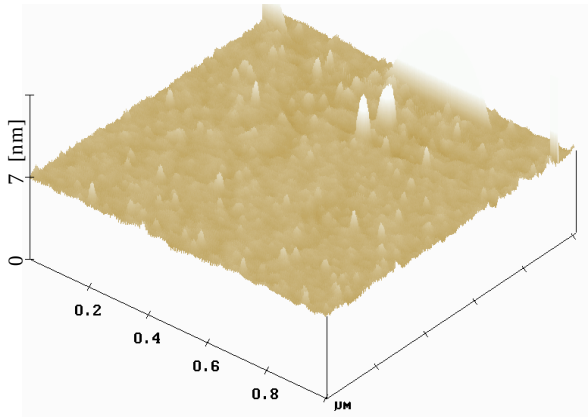

Figure 5.4 Surface of C^- domain of $LiNbO_3$ showing evidence of production of silver nanoparticles.

As already discussed in section 4.1, on the surface of C^+ domain, due to the downward band bending, electrons are driven to the surface making the surface reductive, while on the surface of C^- domain, due to the upward band bending, holes are driven to the surface making the surface oxidative. On the C^+ domain, the

deposition of silver nanoparticles is due to the downward band bending at the surface, leading to an availability of electrons for photoreduction of silver[3]. The pattern of silver deposition in discrete particles is due to the localisation of free electrons at the surface defects or sub-surface defects. This is demonstrated in Figure 5.5, where a localised nanowire has formed. The surface of the crystal was epi-polished and prior to deposition no topographical features were seen. It is likely that the feature of the nanowire has formed due to a sub-surface defect during polishing[4].

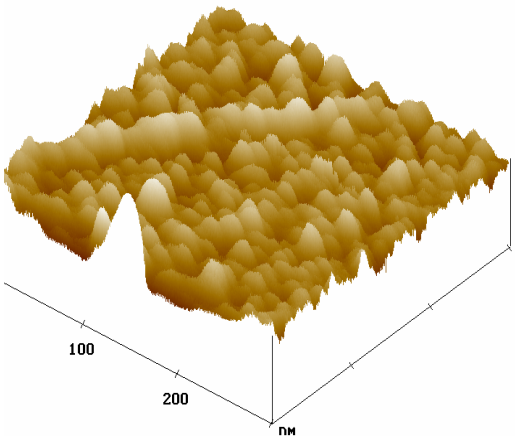

Figure 5.5 AFM image showing formation of localised nanowire at a subsurface defect.

In the vicinity of ferroelectric surface, the polarisation induced surface charge needs to be compensated by internal and or external screening. Defects contribute to internal screening and the low concentration of defect states near the LN surface (10^{12} cm^{-2})[5] leads to weak internal screening. Therefore, on a LN surface the predominant mechanism of screening is external[10], as shown in Figure 5.6. As a result of weak internal screening, the band bending associated with it (and the SCR) occurs over a larger length scale[6] and the electric field in the SCR is weak (as compared to PZT). As a result of this, the separation of electron-hole pairs is less efficient and the electron flux reaching the surface is low. This results in lesser amount of photoreduced silver on the surface with average size of nanoparticles ranging from 7-20 nm as compared to PZT where size of silver particles is between 80-250 nm. On

the surface of PZT, a high number of defects (10^{14} cm^{-2})[7] allow complete internal screening and strong band bending resulting in an efficient separation of electron-hole pairs and a higher flux of electrons reaching the surface. This leads to a higher deposition of silver on PZT surface than LN.

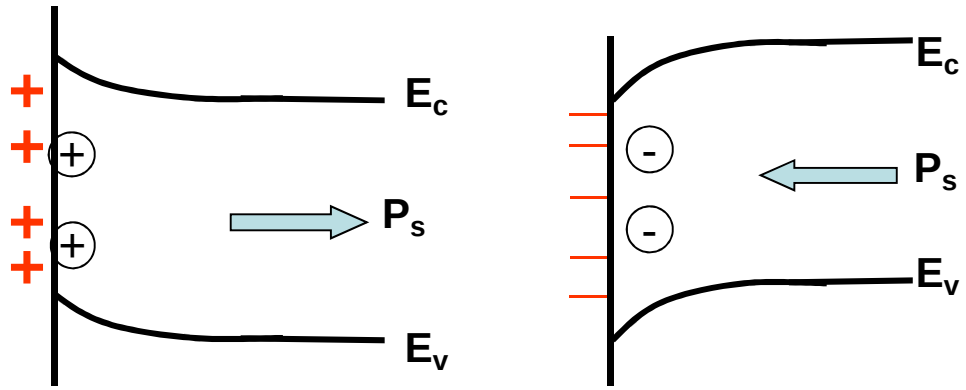

Figure 5.6 Band diagram and screening mechanisms for LN. The predominant mechanism of screening in LN is external. ⊕, ⊖ are internal screening charges, + − are external screening charges and arrow represents the direction of spontaneous polarisation.

In 2004, Yang *et al.*[8] demonstrated that on a LN surface the screening of the polarisation charges by adsorption of charged molecules or ions on the surface will give rise to an additional surface dipole resulting in a variation in the electron affinity, as shown in Figure 5.7. On the C^- surface, the electron affinity (χ) decreases by $\Delta\chi$ =0.8 eV, whereas on a C^+ surface the electron affinity increases by the same amount. As a result of decreased electron affinity, the photothreshold of C^- surface reduces to 4.6 eV (experimentally observed by Yang *et al.* using UV-photoelectron emission microscopy), whereas the same for C^+ surface is 6.2 eV.

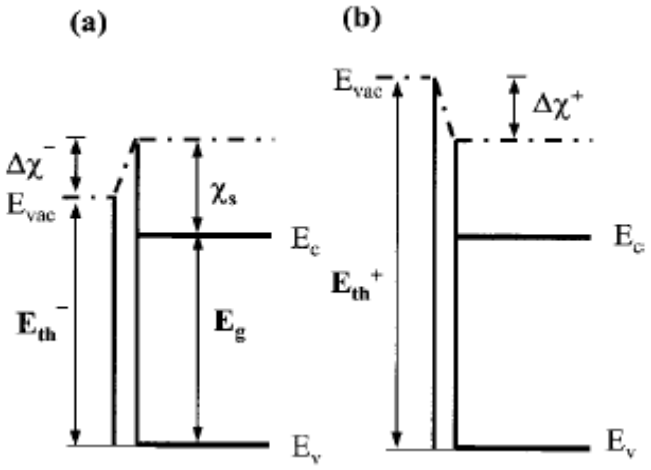

Figure 5.7 Energy-band diagrams of adsorbate-covered (a) C^- domain (b) C^+ domain of LN. χ_s, E_g ,E_{th}, and $\Delta\chi$ are surface electron affinity, band gap, photothreshold, and change in electron affinity due to surface adsorption respectively. (Source ref. 5)

On the C^- face of the LN crystal, although the space charge layer of the sample would inhibit electron reaching the surface, there has still been reduction of silver cations to silver metal clusters. The size and distribution of the clusters is identical to the initial stages of metal cluster deposition, where photogenerated carriers are responsible. Dunn *et al.*[9] have already demonstrated that it is possible to alter the space charge layer of a semiconductor by using high energy super band gap irradiation. However, in the case of LN, this would not be expected as the high remnant polarisation (P_r) and low defect density in LN generate a large space charge region.

It is believed that the silver being deposited on the C^- domains of LN is being produced as a result of the photoelectric effect. If it is accepted that the electron affinity is between 1.1 and 1.5eV and the band gap (E_g) is 3.9eV[8], the photoelectrically generated photons will be able to interact with the Ag^+ that are bound to the C^- surface when photons above *ca* 4.6eV are incident on the surface. It is known that photons of this wavelength are capable of penetrating the silver nitrate solution[2]. Figure 5.8 shows a proposed mechanism for deposition of silver

nanoparticles through reduction of silver cations on the surface of a C^+ and C^- domain of LN.

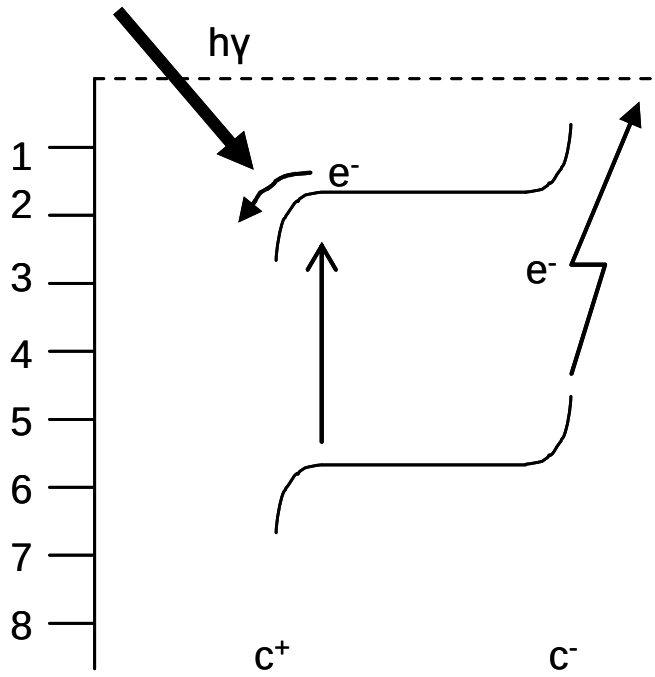

Figure 5.8 Proposed schematic for photoreduction of silver cations over C^+ domain and photoelectric reduction of silver cations over C^- domain. Here E_g is 3.9eV and X_s is 1.5eV.

The interesting questions that arise from the studies on LN, that have been undertaken so far, relate to the subtle differences seen in the work undertaken. Two different broad observations have been published – one shows photo assisted deposition on domain boundaries by Hanson *et al.*[10] and the other shows deposition across the bulk of a poled domain by Liu *et al.*[11]. The differences in the results presented in these reports are in the energy of irradiation and power of the source used. In cases where a high power and therefore higher flux of photons is generated, a complete domain decoration according to domain dependent coverage is observed[11]. When a lower power output is used, only domain boundaries are sites of nucleation[10].

The use of photoelectric effect to reduce metal cations on the C^- domains of LN has been demonstrated. The effect is shown to be dependent on the location of valence band with respect to the vacuum level and degree of band bending caused by the

external dipole and mechanism of screening polarisation charge. Using the arguments presented above, it should be possible to see evidence of the photoelectric effect producing metal nanoparticles on other ferroelectric systems.

5.2 Impact of doping of lithium niobate on silver photoreduction

Lithium niobate crystals used in this research are grown by Czochralski (CZ) technique and are deficient in lithium (Li/[Li+Nb]~0.485)[12]. Deficiency of lithium leads to a good concentration of intrinsic defects which include niobium antisites and vacancies. These defects can affect electrical, optical and thermal properties of LN crystals. The impact of doping of LN with 5% MgO on its defect structure and photochemical properties is investigated in this section. A comparative analysis of silver deposition on undoped LN and 5% MgO doped LN is presented.

5.2.1 Experimental procedure

The samples used in this work are LN crystals doped with 5% MgO, and undoped LN. Prior to deposition, the samples were cleaned with acetone and iso-propynol alcohol (IPA). C^+ face of undoped and 5% MgO doped LN was dipped in 0.01 M silver nitrate salt solution and irradiated with 'H' lamp for 15 minutes. After irradiation, the samples were rinsed with deionised water and blown dry with nitrogen and were fixed on a glass slide with a double sided Carbon tape. TM-AFM analysis was done on both the samples, followed by ESEM-EDX analysis.

5.2.2 Results and discussion

Before irradiation, the TM-AFM topographic image of the surface showed no surface features within a z-scale of 3 nm. After irradiation, the topographic images of the

undoped LN sample and MgO doped LN sample are shown in Figure 5.9 (a) and (b) respectively. The z-scale for both images is 20 nm. ESEM-EDX analysis of both the samples was done to evaluate the percentage of Ag deposited on both samples. The software for ESEM-EDX was first calibrated using a standard Co sample and then analysis was performed.

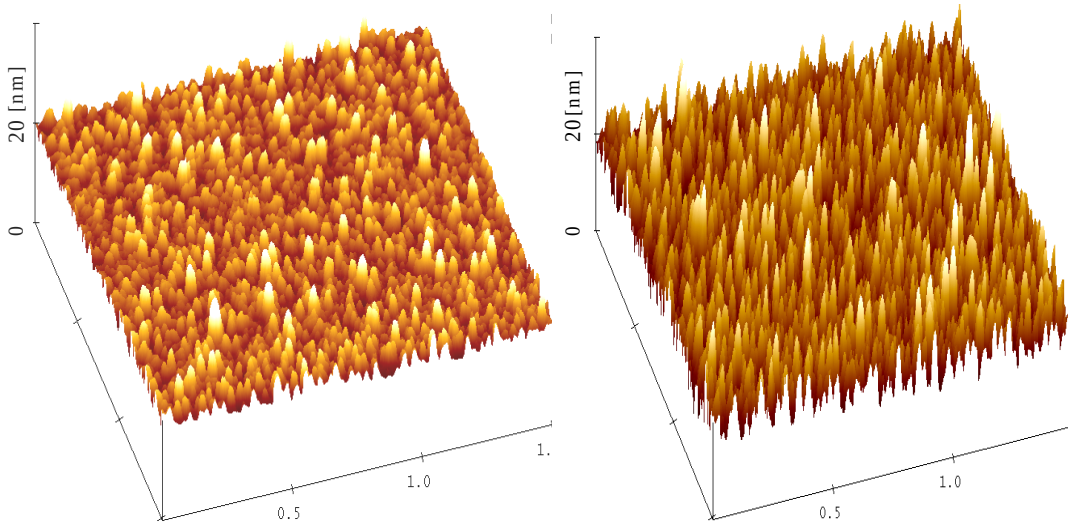

(a) (b)

Figure 5.9 TM-AFM image of silver deposition on the non-doped LN sample (a) and MgO doped LN sample (b). The area covered in both images is 1.5 X 1.5 μm^{2}and the Z scale is 20 nm.

It is evident from Figure 5.9 that the deposition of Ag clusters is enhanced on MgO doped LN. Particle analysis of deposited silver was done on both the samples and the average particle size is found to be 8.6 nm in undoped LN and 18.3 nm in MgO doped LN. The particle size is more than double in sample (b) as compared to sample (a). ESEM-EDX gives 0.47% Ag present on sample (a) and 1.8% Ag present in sample (b). The quantity of photoreduced silver on MgO doped LN is more than three times greater than on undoped LN.

The difference in photochemical reactivity of the two samples could be due to a change in the band-gap of the two samples arising due to MgO doping. There are several studies reporting that the absorption edge in MgO doped LN crystals is shifted

to higher energy compared to undoped LN crystals[13]. Feng *et al.* have shown that the band-gap of MgO doped LN is 4.04 eV as compared to 3.9 eV of undoped LN[14]. Due to the 0.1 eV increase in band-gap energy of MgO doped LN a slight decrease in photoreduced silver on its surface was expected; conversely, a significant increase in photoreduced silver on its surface was observed. Therefore, other factors that could be causing an increased photochemical reactivity at the surface were investigated.

In 1972, Peterson *et al.*[15] studied the structure of undoped LN and proposed a model called 'Nb-site vacancy model' according to which some Li sites are occupied by Nb ions and vacancies exist at the Nb sites. Later, this model was confirmed by Abrahams and Marsh[16] who determined by X-ray measurements that in congruent lithium niobate Li site contains 94.1% Li and 5.9% Nb whereas the Nb site contains 95.3% Nb and 4.7% vacancies, the O site contains 100% oxygen. The LN was expressed as $[Li_{0.941}Nb_{0.059}]\ [Nb_{0.953}\square_{0.047}]\ O_3$, where □ represents Nb vacancies. The Nb ions in place of Li lead to antisite defects represented as Nb_{Li}. It is believed that defects, such as niobium antisites, create electron traps between valence and conduction bands that act as recombination centres[17]. Kitamura *et al.*[17] observed that LN crystals have deep level traps located at 1.9 eV below the conduction band, and upon irradiation with UV light the photogenerated electrons have a finite probability of ending in these strongly lowered electron traps, as shown in Figure 5.9. When MgO dopant is added to LN, the Mg ions replace the Nb_{Li} antisites and all Nb_{Li} would be replaced by around 5% MgO[16]. Absence of Nb_{Li} electron traps in MgO doped LN results in an increased availability of photoexcited electrons to perform photochemistry at the surface. In addition to this, with the removal of Nb_{Li} electron traps, the photoexcited free carriers have longer lifetime, and a combination of increased availability and longer life of photogenerated electrons leads to an increase

in silver deposition at the surface. This suggestion is further supported by the work of several groups, who have shown that doping a LN crystal with MgO increases its photoconductivity and resistance to optical damage significantly[18]; this is again attributed to the decreasing concentration of Nb_{Li}, acting as electron-traps leading to a longer lifetime of photogenerated electrons and holes. Therefore, it can be said that the difference in photoreduced silver on the two samples is attributed to the variation in their defect structures.

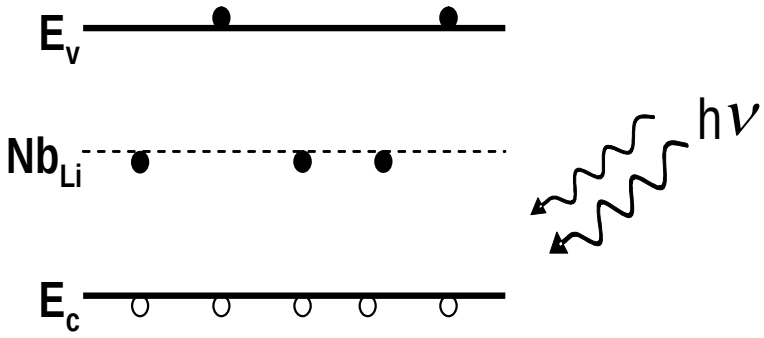

Figure 5.10 Energy band diagram of non-doped LN depicting the presence of Nb_{Li} electron traps. Where ● is photogenerated electron, ○ is photogenerated hole, Nb_{Li} is electron trap created due to Nb_{Li} antisites.

5.3 Impact of photon energy on silver reduction

Energy of incident photon can influence the chemical reactions occurring on the surface of a ferroelectric material. Few investigations into the effect of photon energy on chemical reactions on the surface of PZT have been reported in literature[19,20]. But, there is less information about the photochemistry of LN at different photon energies. In order to understand the impact of photon energy on chemical reactions occurring at the LN surface/solution interface, Ag deposition experiments were performed using monochromatic UV light (light that has only one wavelength) in place of UV source (wavelength between 200-400 nm).

5.3.1 Experimental procedure

The samples used in this work are z-cut 5% MgO doped LN crystal. The crystals have been poled to present either C^+ or C^- faces. Prior to experiments, CLN samples were cleaned, rinsed with deionised water, and finally blow dry with nitrogen gas. The samples were then immersed in freshly prepared 0.01 M silver nitrate solution and kept in a sample holder for UV exposure. The experimental set-up is shown in Figure 5.11.

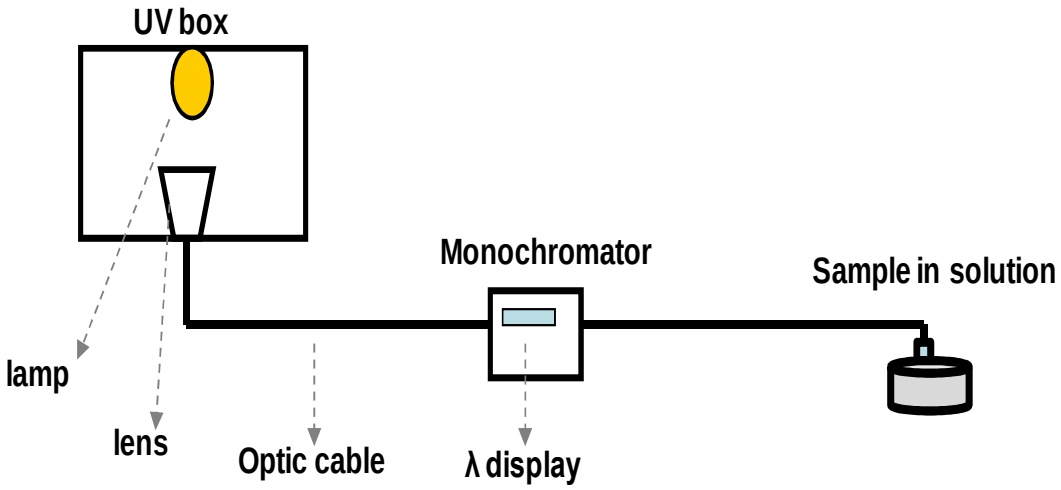

Figure 5.11 Experimental set-up for the Monochromatic UV light experiments

The UV box was fitted with 'H' lamp and a collimating lens (Ocean Optics 84-UV-25) was placed directly underneath the lamp. The output from the lens was transferred via an optic cable (QP600-2-SR/BX) to the Monochromator. The Monochromator resolves polychromatic radiation into its individual wavelengths and allows a narrow band (5 nm) monochromatic light to exit. The desired wavelength of light can be selected by adjusting the wavelength display panel on the front of monochromator. The selected wavelength light was transferred via another optic cable to the sample holder where it focussed directly over the sample. The wavelengths chosen for the experiments were 313 nm (3.96 eV), 294 nm (4.21 eV) and 276 nm (4.49 eV). The C^+ and C^- domains of LN were irradiated for six hours and then rinsed with distilled

water and blow-dry with nitrogen. TM-AFM was done on the samples to analyse silver deposition.

5.3.2 Results and discussion

When the C^+ domain was exposed to 3.96 eV (313 nm) light, no silver was seen on the surface. Upon using 4.21 eV (294 nm) some tiny features were seen on the C^+ surface, whereas 4.49 eV (276 nm) gave a clear silver deposition. The TM-AFM images showing the surface of C^+ domain upon exposure to light at 4.21 eV and 4.49 eV are shown in Figure 5.12 (left) and (right) respectively. In order to present a better picture of silver deposition at 4.49 eV, a 3-D image is presented in Figure 5.13.

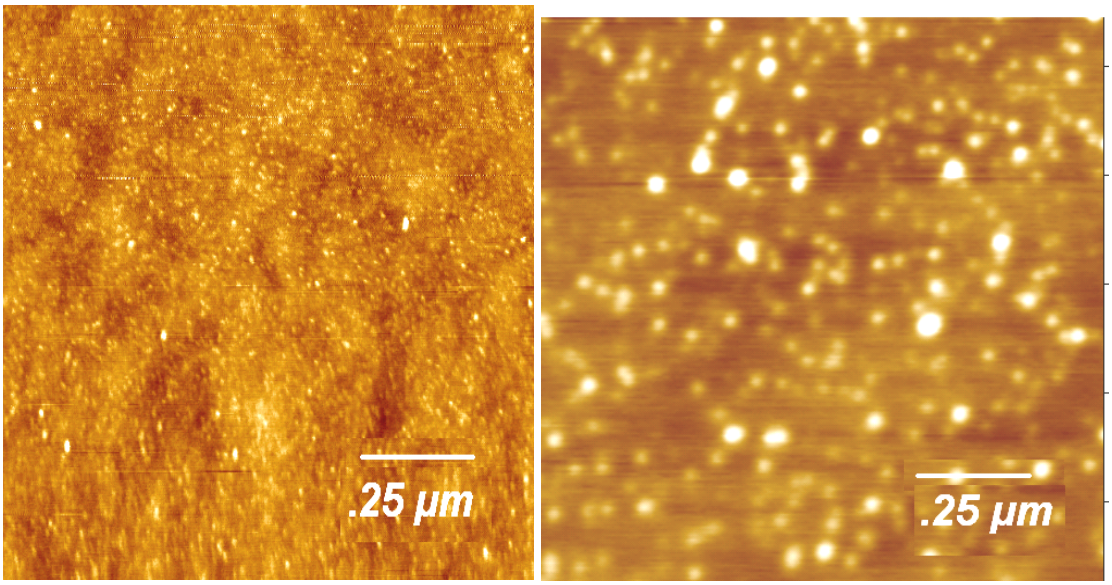

Figure 5.12 C^+ domain after irradiation with 4.21 eV (left) and 4.49 eV (right).

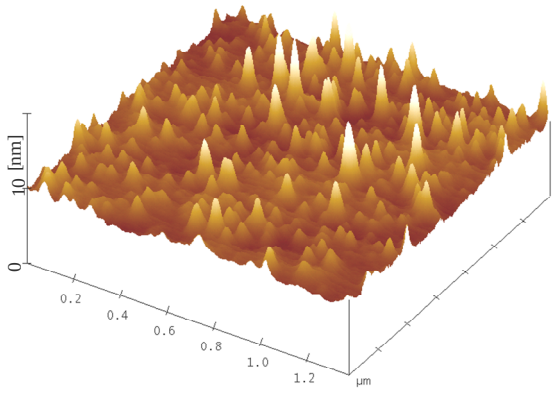

Figure 5.13 3-D image of C^+ domain showing silver deposition at 4.49 eV.

When C^+ domain of LN was exposed to monochromatic light at 3.96 eV no silver deposition was seen. This is due to the fact that 3.96 eV is less then the band gap of MgO doped LN (4.04 eV)[14]. Silver deposition starts at 4.2 eV, as shown in Figure 5.12 (left). This gives an additional 0.16 eV of energy over the band gap for the LN as a requirement for the growth of silver nanoclusters. Silver deposition on the surface improved when light of 4.49 eV was used, Figure 5.12 (right). The size of silver nanoparticles in TM-AFM image was analysed using 'Particle analysis' software and it was found that at 4.2 eV the average particle size is 3.2 nm whereas it increased to 7.4 nm at 4.49 eV. This increase in silver deposition on C^+ domain with the increase in photon energy is due to the structure of density of states of the material. The density of states increases with depth into the valence band, and therefore irradiation with increasing higher energy light leads to an increase in the flux of electron-hole pairs that are formed. An increase in the number of electrons in the conduction band results in a significant increase in photoreduced silver at the surface.

Figure 5.14 shows topographic (left) and 3-D (right) images of C^- domains after irradiation with 4.2 and 4.49 eV.

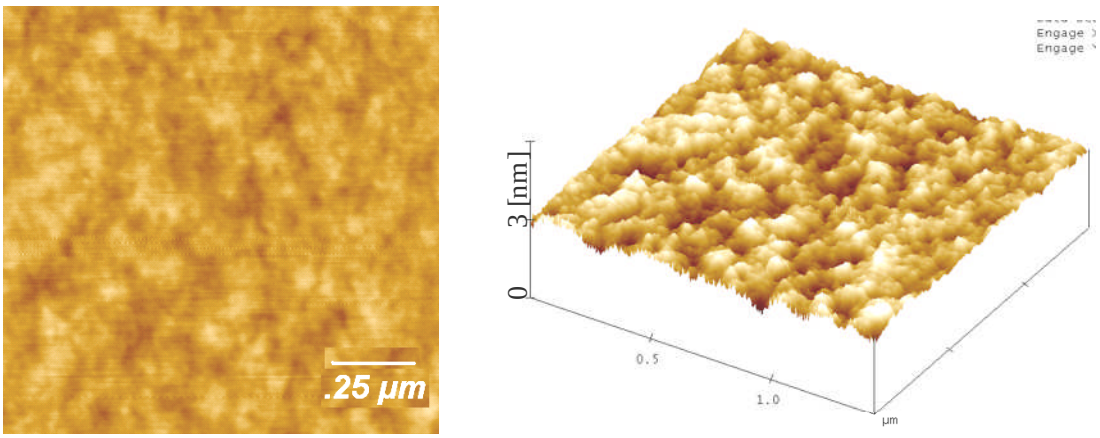

Figure 5.14 A topographic and 3-D image of C^- domain. Z-scale in 3-D image is 3 nm. The surface is clear and no silver deposition is seen.

No evidence of silver deposition is seen on C^- domains up to 4.49 eV. This is again due to the presence of band bending at the surface; the internal electric field in the space charge region drives the electrons away from the surface preventing any deposition of silver.

5.4 Impact of photon intensity on silver reduction

5.4.1 Experimental procedure

The sample used in this work was non-doped LN. For irradiation two Ultra-violet lamps namely 'H' and 'F' lamps were used. The energy spectra of 'H' and 'F' lamp are shown on page 53 (Figures 3.4 and 3.5). Prior to experiments, LN samples were cleaned and then placed inside the UV box fitted with either 'H' or 'F' lamp and exposed for ten minutes. After irradiation, the samples were rinsed with de-ionised water, blow dry with nitrogen, and then were firmly stuck to glass slide using double sided Carbon tape. TM-AFM experiments were performed to analyse Ag deposition.

5.4.2 Results and discussion

TM-AFM analysis of LN samples exposed to different lamps reveals that there is more photoreduced Ag on C^+ and C^- face of LN exposed to 'H' lamp as compared to 'F' lamp. The average particle sizes of silver nanoparticle on C^+ domain exposed to 'H' and 'F' lamp are 7 nm and 4.5 nm respectively. The silver nanoparticles are bigger in size on sample exposed to 'H' lamp as compared to 'F' lamp. EDX analysis shows that there is greater amount of photoreduced silver on sample exposed to the 'H' lamp as compared to the 'F' lamp. Therefore, silver deposition is enhanced when using the 'H' lamp as compared to 'F' lamp. Upon comparing the energy spectrum obtained from both the lamps, it is found that at frequencies above the band gap of

LN, ‘H’ lamp is more intense than ‘F’ lamp. This means that ‘H’ lamp provides a higher flux of photons that have energy above the band-gap of LN. With an increased number of photons hitting the LN surface, an increased number of photo generated electrons are created that can participate in the chemical reaction at the surface, eventually leading to an increased deposition of silver at the surface.

5.5 Photoreduction of Al and Mn salts on lithium niobate

This section focuses on the photoreduction of Al and Mn salts on a LN surface. It was observed that a metal that has reduction potential within the bandgap of the ferroelectric material can be photoreduced on the surface of C^+ domain. Al nanoparticles have gained huge interest in recent years due to their applications in propellants and energetic applications, and their ability to react with water molecules and produce hydrogen at room temperature. A novel technique to produce Al and Mn nanoparticles in the range of 20 nm is presented in this section.

5.5.1 Experimental procedure

The sample used for experiments are single crystal LN. Sample of size 0.5×0.5cm was dipped in freshly made 0.01 M aluminium chloride or manganese nitrate solutions and exposed to ‘H’ lamp for two hours. After illumination, the samples were rinsed with de-ionised water and blow dry with nitrogen. The samples were analysed using Tapping mode-AFM to investigate the deposition of Al or Mn nanoparticles, followed by EDX and XPS analysis.

5.5.2 Results and discussion

A TM-AFM image of LN surface before experiments shows that the surface is smooth and absent from any topographical features. TM-AFM analysis was done on LN samples after 15 min of UV exposure (same amount of time as done for Ag experiments) but nothing was observed on the surface. When the samples were exposed for longer (two hours), photoreduced Al was detected on the surface. TM-AFM image of LN surface after Al deposition is shown in Figure 5.15 (left). Particle analysis of deposited Al informs that the average particle size of deposited Al is around 20 nm. ESEM-EDX of C^+ domain was done and presence of a clear Al peak at 1.5 eV (Figure 5.15 (right)) confirms that Al is present on the surface.

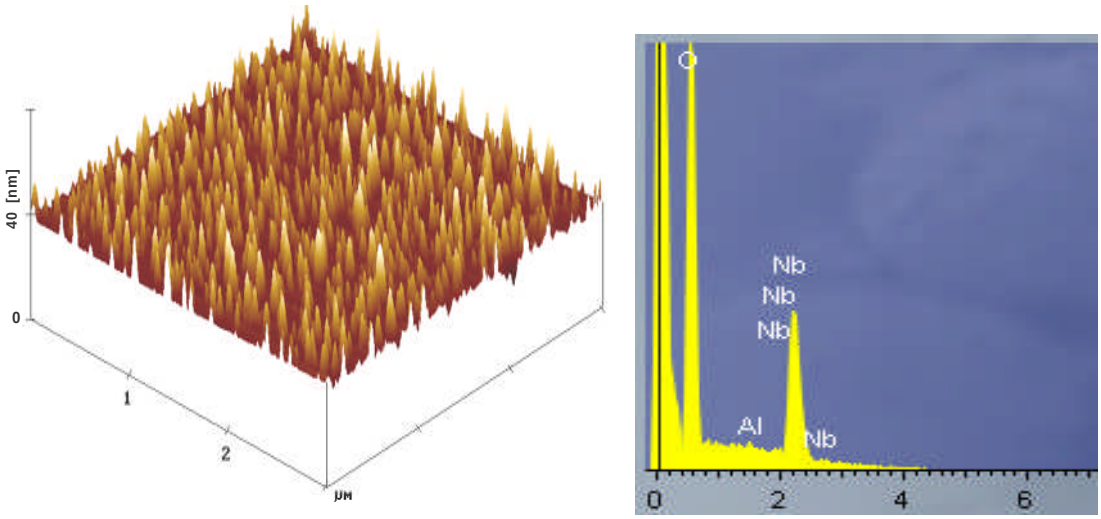

Figure 5.15 AFM image showing Al deposition on C^+ domain (left). The z-scale is 40 nm. ESEM-EDX of C^+ domain shows a clear Al peak (right).

XPS analysis was done on C^+ domain of LN before and after the Al deposition experiments. The XPS plots are shown in Figure 5.16. Due to charging of LN surface during XPS analysis a shift of +11 eV was observed in all the element peaks. An Al peak was observed at 84 eV in the XPS graph (Figure 5.16 (right)) confirming the presence of Al on the surface whereas no such peak was observed before the experiments (Figure 5.16 (left)).

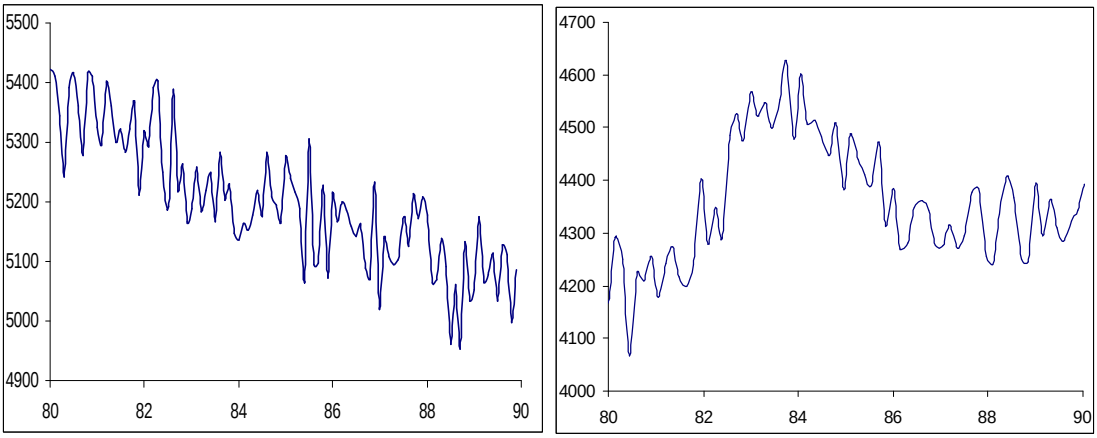

Figure 5.16 XPS plot of LN crystal before Al experiments (left); note the absence of Al peak at 84 eV. XPS plot of LN crystal after Al experiments (right), an Al peak is present at 84 eV.

Similarly, AFM image showing Mn deposition on C^+ domain and XPS plot showing Mn peak at 651 eV are shown in Figure 5.17 (left) and (right) respectively.

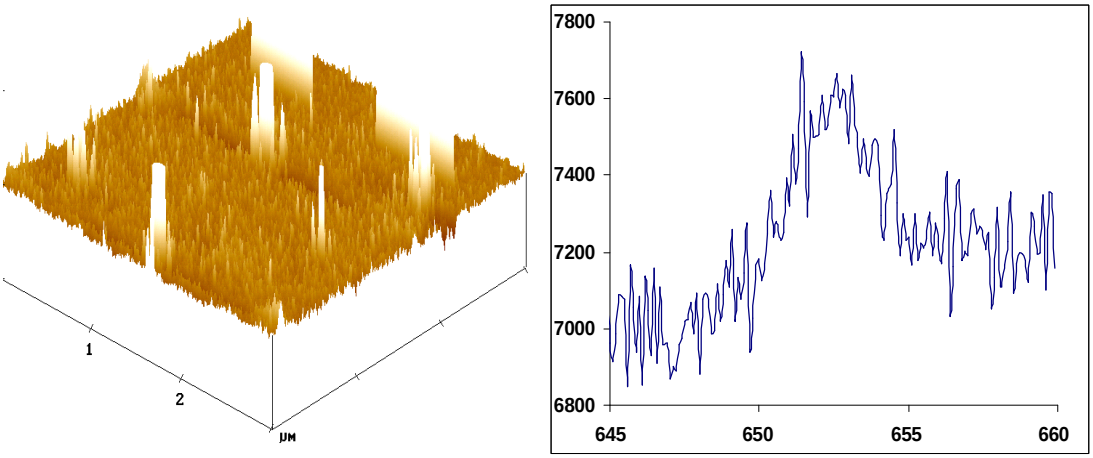

Figure 5.17 AFM image showing Mn deposition on C^+ domain (left) and XPS plot showing Mn peak at 651 eV (right).

In order to determine whether there will be reduction or oxidation of solvated species in a semiconductor, it is convenient to draw an energy diagram for semiconductor interface on which energies of band edges E_c and E_v are displayed along with the electrochemical potentials of the species[21]. The energy scale is indicated using vacuum level or Normal Hydrogen Electrode (NHE) as reference. It is now commonly accepted that the value of the NHE in electrochemical terms lies 4.5V (or 4.5eV) from vacuum[22]. It is therefore possible to map an electrochemical potential

against the band structure of a semiconductor, and determine whether there will be reduction or oxidation of solvated ions on the semiconductor surface. This relation between band edges and electrochemical potential can be applied to ferroelectric $LiNbO_3$ and in this way electrochemical reactions occurring on its surface can be studied. Taking the electron affinity of $LiNbO_3$ between 1.1 and 1.5eV and the band gap (E_g) as 3.9eV[8], E_c and E_v have been marked on energy scale, as shown in Figure 5.18. This implies that metals that have reduction potential (relative to NHE) between -3 and 0.9 eV can be photoreduced on LN surface.

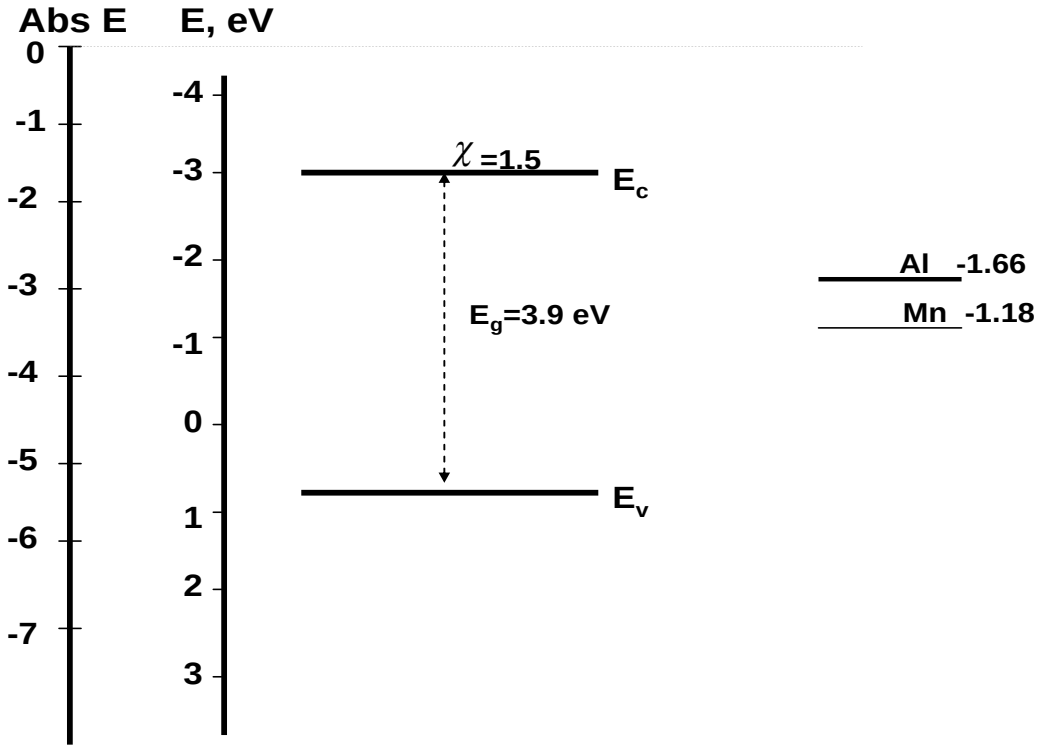

Figure 5.18 Normal Hydrogen Electrode (E) is mapped against the reduction potential of Al and Mn metals. LN band edges are plotted taking E_g as 3.9eV and X_s as 1.5eV.

For experimental work, Al and Mn metals were chosen whose reduction potentials are -1.66 eV and -1.18 eV respectively. Both these metals have their reduction potentials below the conduction band of LN. Therefore, on the C^+ domain it is energetically favourable for the photogenerated electrons to drop from the conduction band and

reduce the metal cations available at the interface to metal. This is the reason why photoreduced Al and Mn were present on C^+ domain via the reaction:

$$Al^{3+} + 3e^- \rightarrow Al$$

$$Mn^{2+} + 2e^- \rightarrow Mn$$

In which Aluminium ion (Al^{3+}) and Manganese ion (Mn^{2+}) combine with photogenerated electron (e^-).

However, Al and Mn cations took longer (approximately two hours) to deposit as compared to Ag (15 minutes). The reason behind this could be that the reduction of Al and Mn involves three and two electrons respectively, whereas silver reduction reaction involves a single electron and therefore is much faster compared to the other two. On the C^- domain there was trace of small amount of Al and Mn metal clusters. The size and distribution of the clusters were identical to the initial stages of metal cluster deposition. This is due to the photoelectric effect, as already discussed in section 5.1. Due to the presence of holes on the surface of C^- domain the most probable oxidation reaction is oxidation of water, via the reaction:

$$H_2O + h^+ \rightarrow \frac{1}{2}O_2 + 2H^+$$

Aluminium has a high affinity to oxygen, and therefore aluminium nanoparticles synthesised during the process react immediately with oxygen present in the air and form aluminium oxide following the reaction:

$$2Al + \frac{3}{2}O_2 \rightarrow Al_2O_3$$

The aluminium oxide forms a layer of thickness few angstroms on the surface of aluminium nanoparticles, so that the core remains aluminium with a skin of aluminium oxide at the surface[23], as shown in Figure 5.19. This oxide skin seals the surface, thus stopping any further oxidation. Performing these experiments in vacuum

should avoid the formation of oxide layer and pure aluminium nanoparticles can be obtained.

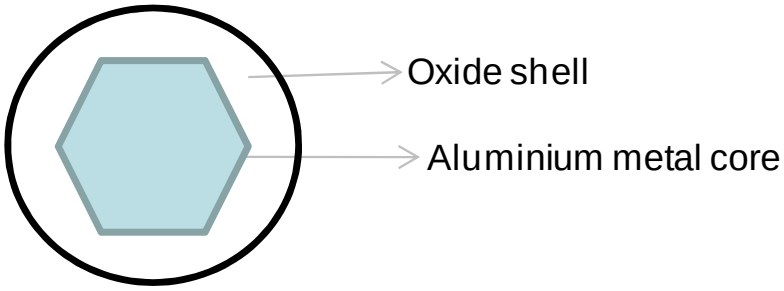

Figure 5.19 Schematic of an aluminium nanoparticle on the LN surface, showing the aluminium metal core and an oxide shell (Source ref. 24)

5.6 Molecular adsorption on $LiNbO_3$

In this section, preferential deposition of stearic acid onto the surface of LN is presented. A vapour deposition technique was utilised in this process. When LN surface was exposed to vapours of stearic acid, the molecules carrying negative charge were attracted towards the C^+ domain of LN. This is attributed to the high magnitude of polarisation bound charge present on the surface of LN and pre-dominant external screening mechanism.

5.6.1 Experimental work

The sample used in this work was single crystal LN of size 0.5 X 0.5cm^2. C^+ and C^- faces of LN were adhered to a glass slide using a carbon tape. Stearic acid powder (Sigma Aldrich, melting point 80 ºC) was used for the experiments. The experimental set-up is shown in Figure 5.20.

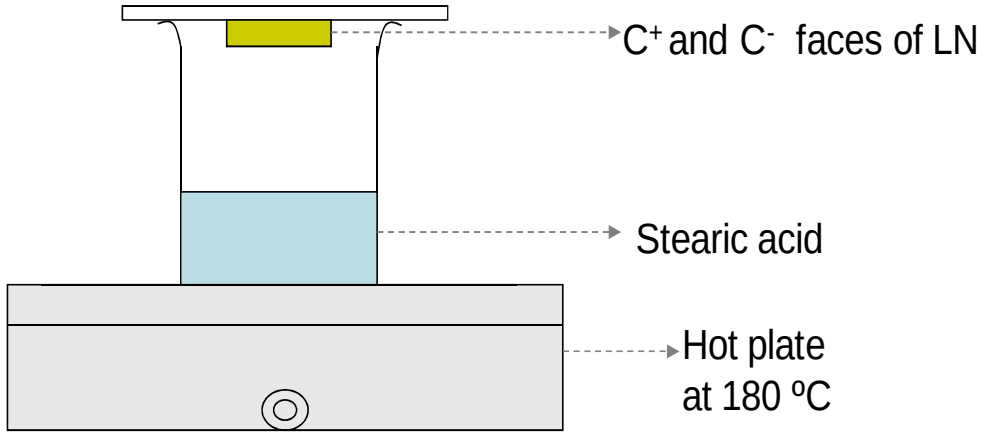

Figure 5.20 Experimental set-up of adsorption experiments

Two cm depth of stearic acid powder was taken in a beaker and the beaker was kept onto a hot plate set at 180 ºC. With temperature high above the melting point the stearic acid in the beaker starts to melt and vaporise. At this point, C^+ and C^- faces of LN were exposed to stearic acid vapours for 90 seconds and 180 seconds. A large beaker was kept upside down to shield the system from atmosphere. After exposure, the samples were immediately taken to the SEM to check adsorption of stearic acid vapours from the surface.

5.6.2. Results and discussion

When the LN samples were exposed to stearic acid vapours for 90 seconds, stearic acid adsorbed on C^+ domain, whereas no adsorption was seen on C^- domain. A magnified SEM image of C^+ domain (Figure 5.21) shows that small islands of stearic acid were formed on the surface, whereas no such islands were seen on C^- domain. When the LN samples were exposed to stearic acid vapours for longer (180 seconds), entire C^+ and C^- domains were covered with stearic acid vapours.

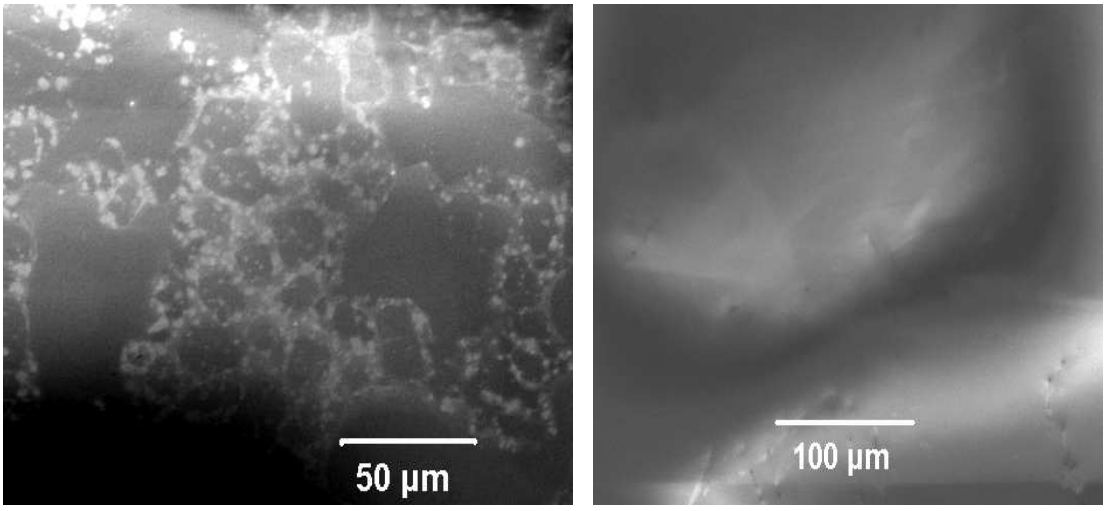

(a) **(b)**

Figure 5.21 SEM image showing (a) adsorption of stearic acid on C^+ domain and (b) no adsorption on C^- domain of LN.

Stearic acid is a fatty acid that has a long hydrocarbon chain with methyl group at one end and a carboxyl group (-COOH) at the other end, Figure 5.22. The carboxyl group is polar in nature and is likely to adsorb to the charged surface of LN.

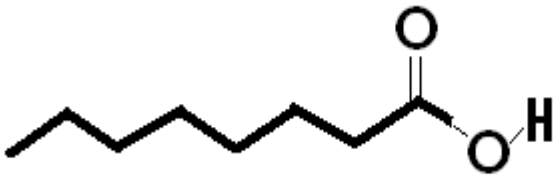

Figure 5.22 A stearic acid molecule representation.

LN possesses one of the highest known magnitude of spontaneous polarisation i.e. 78 ± 3 µC/cm^{-2} and a low density of defects (10^{12} cm^{-2})[5] contributes to weak internal screening. The predominant mechanism of screening is external, and under atmospheric conditions the presence of water and interactions with dipoles in the water contribute to external screening. LN is also a pyroelectric material and heating of the LN crystal will result in a decrease of the spontaneous polarization[25] and overscreening of the polarization at the surface. Therefore, in the case of C^+ domain

there is an excess of negative screening charge on the surface and on the surface of C^- domain there is an excess of positive screening charge. When LN samples were exposed to vapours of stearic acid, the carboxyl end (-COOH) of stearic acid molecule that carries a negative charge should have been attracted towards the excess of positive screening charge present on the surface of C^- domains leading to deposition of stearic acid on C^- domains. However, in contrast to this adsorption of stearic acid was observed on C^+ domain of LN and no adsorption was seen on C^- domain.

When stearic acid was heated up to 180 ºC, the high temperature of the system could have caused some of the adsorbed water molecules at the surface to evaporate[26]. The observed results can be explained by assuming that the effect of water molecular vaporisation is larger than the pyroelectric effect of the LN in this instance. As a result, removal of water molecules from the LN surface may result in some uncompensated positive polarisation charge on C^+ domain and uncompensated negative polarisation charge on C^- domain. Therefore, the carboxyl end (-COOH) of stearic acid molecule gets attracted towards the positive polarisation charge present at the surface leading to deposition on C^+ domain. However, more adsorption experiments need to be performed on LN in order to determine the exact mechanism of selective adsorption of stearic acid molecules.

Giocondi *et al.*[27], have reported adsorption of stearic acid from vapour phase on both C^+ and C^- domains of ferroelectric barium titanate. The reason behind this is that in Giocondi's work stearic acid was heated at 85 ˚C which is close to its melting point and about 100 ˚C less than that used here. Therefore, at that temperature, the flux of stearic acid vapours was too low to cause any selective deposition and exposure for longer time resulted in complete coverage of the surface. Recently in 2008, Habicht *et al.*[28] have reported physical adsorption of charged polystyrene (PS) microspheres

(containing a carboxyl group (-COOH)) on negative domains of LN crystal at elevated temperatures.

Similarly, deposition of stearic acid from the vapor phase was performed on C^+ and C^- domains of PZT. No selective decoration was seen and the whole of PZT surface was covered in stearic acid vapours. The reason behind this is that on a PZT surface the dominant screening mechanism is internal[7], and therefore any change in spontaneous polarisation due to pyroelectric effect will be compensated by internal screening. The removal of water vapours from the PZT surface when exposed to high temperature environment will not leave any polarisation charge uncompensated. The system remains in equilibrium, thus preventing any selective adsorption on the surface.

References

[1] J. Giocondi and G. Rohrer, *J. Phys. Chem*., *B.* 105, 35 (2001)

[2] P.M. Jones and S. Dunn, *Nanotechnology*, 18, 185702 (2007)

[3] S. V. Kalinin, D. A. Bonnell, T. Alvarez, X. Lei, Z. Hu, J. H. Ferris, Q. Zhang and S. Dunn, *Nano Lett*., 2, 589 (2002)

[4] S. Dunn and S. Harada, *J. Eur. Ceram. Soc.*, 28, 14, 2747-2753 (2008)

[5] W. C. Yang, B. J. Rodriguez, A. Gruverman and R. J. Nemanich, *Appl. Phys. Lett.*, 85, 2316-2318 (2004)

[6] A. M. Prokhorov and Y. S. Kuz'minov, *Physics and Chemistry of Crystalline Lithium Niobate*, Taylor and Francis, London (1990)

[7] J. F. Scott, *Ferroelectric Memories*, Springer, Berlin (2000)

[8] W.C. Yang, B. J. Rodriguez, A. Gruverman and R. J. Nemanich, *J. Phys: Condens. Matter*., 17, S1415-1426 (2005)

[9] S. Dunn, P. M. Jones and D. E. Gallardo, *J. Am. Chem. Soc*., 129, 8724 (2007)

[10] J. N. Hanson, B. J. Rodriguez, R. J. Nemanich and A. Gruverman, *Nanotechnology*, 17, 4946 (2006)

[11] X. Liu, K. Kitamura, K. Terabe, H. Hatano and N. Ohashi, *App. Phys. Lett*., 91, 044101 (2007)

[12] S. Kim, V. Gopalan, K. Kitamura, and Y. Furukawa, *J. Appl. Phys*., 90, 2949 (2001)

[13] K. K. Wong, *Properties of Lithium Niobate*, Chapter 9, Institution of Engineering and Technology (2002)

[14] X. Feng *et al.*, *Sci. in China*, Series A, 33, 1, 108-118 (1990)

[15] G. E. Peterson and A. Carnevale, *J. Chem. Phys*., 56, 4848 (1972)

[16] S.C. Abrahams and P. Marsh, *Acta Crystallogr*., *B* 42, 61 (1986)

[17]M. Lee, S. Takekawa, Y. Furukawa, K. Kitamura, and H. Hatano, *J. Appl. Phys*., 87, 1291 (2000)

[18] T. Volk, B. Maximov, S. Sulyanov, N. Rubinina, and M. Wöhlecke, *Opt. Mater.*, 23, 229-233 (2003)

[19] P. M. Jones and S. Dunn, *J. Phys. D: Appl. Phys*., 42, 065408 (2009)

[20] X. Lei, D. Li, R. Shao and D. Bonnell, *J. Mater. Res.*, 20, 3, 712-718 (2005)

[21] Y. V. Pleskov and Y. Y. Gurevich, *Semiconductor photoelectrochemistry*, 1st ed, Consultants Bureau, New York (1986)

[22] M. Grätzel, *Nature*, 414, 338 (2001)

[23] Ch. Schmitz, *Handbook of Aluminium recycling*, Vulkan-Verlag, GmbH (2006)

[24] A. Rai, K. Park, L. Zhou and M. R. Zachariah, *Comb. Theo. Model.*, 10, 5, 843–859 (2006)

[25] E. Fatuzzo and W. J. Merz, *Ferroelectricity*, Amsterdam: North-Holland (1967)

[26] C. E. Nelson, J. W. Elam, M. A. Cameron, M. A. Tolbert, and S. M. George, *Surf. Sci*., 416, 341 (1998)

[27] J. L. Giocondi and G. S. Rohrer, *Mat. Res. Soc. Symp. Proc.*, 654, AA7.4 (2001).

[28] S. Habicht, R. J. Nemanich and A. Gruverman, *Nanotechnology*, 19, 495303 (2008)

6. Conclusions and Future work

6.1 Conclusions

The main conclusions drawn from this work are as follows:

In agreement with the previously reported studies, it was observed that the reactivity of ferroelectric PZT is dependent on polarisation of domain underlying the surface. On a PZT (30/70) of [111] orientation, under UV irradiation metal deposition occurred only on C^+ domains and no deposition was observed on C^- domains.

Annealing of PZT alters the defect concentration which was shown by an increase in the deposition of photoreduced silver on the surface. Silver deposition onto the C+ domain of PZT (30/70) thin films was investigated for samples annealed at a variety of temperatures from 530 - 690°C. With the increase in annealing temperature of PZT from 530-690°C, the amount of deposited silver on C^+ domains increased by more than 150% and the size of deposited silver clusters increased by about four times. In contrast to this, no silver deposition was observed on C^- domains. The increase in the deposition of silver is attributed to increase in the defect concentration due to the volatilisation of components from the PZT leading to an increase in shallow level traps at the surface.

The composition of PZT (Zr/Ti ratio) was also found to influence the photochemical properties of PZT thin films. Silver deposition experiments were performed onto the patterned surface of PZT thin films of three stoichiometric compositions $PbZr_{0.3}Ti_{0.7}O_3$, $PbZr_{0.52}Ti_{0.48}O_3$ and $PbZr_{0.7}Ti_{0.3}O_3$. Photoreduction of silver occurred on both C^+ and C^- domains on $PbZr_{0.52}Ti_{0.48}O_3$ and $PbZr_{0.7}Ti_{0.3}O_3$, whereas it occurred only on C^+ domains on $PbZr_{0.3}Ti_{0.7}O_3$ surface. The difference in deposition pattern is attributed to the difference in width of space charge layer in the three samples and the alteration in the band structure at the surface upon exposure to high energy irradiation.

$PbZr_{0.52}Ti_{0.48}O_3$ and $PbZr_{0.7}Ti_{0.3}O_3$ have narrow space charge region (SCR) as compared to $PbZr_{0.3}Ti_{0.7}O_3$. When high energy 'H' lamp is used to irradiate PZT surface, the photogenerated electron-hole pairs contribute to internal screening at the surface and the width of SCR is reduced. The narrow SCR of $PbZr_{0.52}Ti_{0.48}O_3$ and $PbZr_{0.7}Ti_{0.3}O_3$ is further reduced and on the C^- domain this leads to electrons tunnelling across the narrow SCR and photoreduce silver on the surface.

The size of a poled pattern was found to have an impact on silver deposition at the surface. For smaller size of C^+ domains (smaller than 1 μm), the amount and size of deposited silver decreased as the domain size decreases. This variation in photoreduced silver is attributed to a combination of two factors. Firstly, due to small size of domain, the flux of photogenerated electrons and holes is reduced. Secondly, because of the electric field present at domain boundaries, a substantial number of electrons migrate from the bulk to the side boundaries. The later phenomenon is insignificant on domains of larger size because, despite the electron migration to side boundaries, there still is a great flux of photogenerated carriers reaching the surface for photochemistry.

A top-down approach was utilised to investigate the impact of size effects on the photochemistry of PZT. Islands of different sizes were fabricated on a PZT thin film via focussed-ion-beam milling, and the silver deposition was analysed on them. No silver deposition occurred on PZT islands, whereas normal silver deposition occurred on PZT surface away from the milled region. The reason for no silver deposition on PZT islands is due to the damage caused to PZT area that is exposed to high energy beam during focused-ion-beam milling. Therefore it is concluded that, due to the effects induced by processing in top-down approach, it is difficult to investigate the size effects, and a bottom-up approach could be a better option.

Silver cation reduction on C^+ and C^- domains of ferroelectric lithium niobate (LN) by photochemical and photoelectric processes was demonstrated. In previously reported work, silver deposition was seen only on C^+ domains. This work takes this research further by demonstrating the use the photoelectric effect to reduce metal cations on C^- domains. This is in addition to the previously understood phenomenon of domain directed photophysics, where influences on space charge layer, due to the internal dipole of a ferroelectric material, determine the carrier at the surface. The reduction of the photoelectric threshold for LN, due to the polar nature of the crystal, allows high energy UV irradiation to produce free electrons that can participate in photochemical reduction of silver nitrate on the surface. The interaction of photoelectric and domain dependent influences can be observed in LN due to its low electron affinity (ca 1.1-1.5eV).

It was found that doping a LN crystal with MgO changes its photochemical properties. The amount of photoreduced silver was more than three times and the size of silver particles was more than double on 5% MgO doped LN as compared to undoped LN. The enhancement in the photochemical activity of LN upon doping with MgO is attributed to the removal of defects, such as niobium antisites, that create electron traps between valence and conduction bands. This results in an increased availability of photoexcited electrons to perform photochemistry at the surface.

The energy and intensity of incident photon was found to have an impact on the photoreduction of silver on LN surface. Silver deposition on the C^+ domain started at 4.2 eV (which is 0.3 eV above the band gap of LN), and was improved when light of 4.49 eV was used. No silver deposited on C^- domain up to the energy of 4.49 eV. This increase in silver deposition on C^+ domain with the increase in photon energy is due to the structure of density of states of the material. In addition to this, silver deposition

on LN enhanced when a higher energy ‘H’ lamp was used as compared to a lower energy ‘F’ lamp. This is due to an increased number of photons hitting the LN surface, resulting in an increased number of photogenerated electrons and an increased silver deposition at the surface.

Deposition of Al and Mn nanoparticles on LN surface by means of photoreduction reaction has been demonstrated. It was shown that for a metal to photoreduce on C^+ domain of a ferroelectric material, its reduction potential has to be within the band-gap of the material.

It was shown that under atmospheric conditions, it is possible to selectively adsorb molecules of opposite charge on the surface of LN due to uncompensated polarisation charge. The LN surface, upon exposure to stearic acid vapours, caused adsorption of stearic acid molecules only on C^+ domain, and no adsorption was seen on C^- domain.

6.2 Future work

This research has provided many prospects for future research. Some of the possibilities of future work are described as follows:

1. Improve the efficiency of Al photoreduction on LN surface. It was proved that photoreduction of Al is possible, and therefore further investigations on increasing the efficiency of photon to Al metal reduction by adjusting the experimental conditions such as photon energy, solution concentration, LN sample processing etc. can be done. Al nanoparticles have gained interest in recent years due to their ability to react with water molecules to split oxygen and hydrogen bonds and produce hydrogen at room temperature. The synthesised Al nanoparticles can generate hydrogen on demand eliminating the need to store it.

2. Investigate the smallest size of ferroelectric island or structure at which it can perform photochemistry. A bottom-up approach should be utilised to create small sized ferroelectric structures so that the effects induced by processing conditions are eliminated. This knowledge will aid in understanding the impact of size effect of ferroelectric material on their photochemistry.

3. Investigate the effect of doping PZT with different impurities on the photochemical reactivity at the surface. Doping PZT will change the defect concentration of the material and this will have an impact on the deposition of metal at the surface.

4. Further investigations on the photoreduction of gold onto PZT surface are required. It was noticed that spherical, triangular and hexagonal gold plates were depositing on PZT surface irrespective of the underlying domain. Further studies on selective photoreduction of gold can be done and the possibility of making other structures e.g. gold nanowires etc. should be explored.

APPENDIX A. PUBLICATIONS

J Mater Sci (2009) 44:5063–5079
DOI 10.1007/s10853-009-3472-1

FERROELECTRICS

Photochemistry on a polarisable semi-conductor: what do we understand today?

Divya Tiwari · Steve Dunn

Received: 28 February 2009 / Accepted: 6 April 2009 / Published online: 22 April 2009

Abstract The continued development of ferroelectric materials into more and more consumer led applications has been at the forefront of recent ferroelectric material research. It is, however, possible to view a ferroelectric as a wide band gap semi-conductor that can sustain a surface charge density. This charge density arises from the movement of ions in the crystal lattice and the need to compensate for this charge. When viewing ferroelectrics as polarisable semi-conductors a large number of new interactions are possible. One such is the use of super band gap illumination to generate electron hole pairs. These photogenerated carriers can then perform local electrochemistry. What is most interesting for ferroelectric materials is that the REDOX chemistry can be chosen by selectively modifying the domain structure of the ferroelectric—we can perform oxidation and reduction on the surface of the same material at spatially separate locations, or use the material to drive photoexcited carriers apart. This means we can separate the REDOX products or produce patterns of photogenerated material in places we have predetermined. This review aims to introduce the background research that has led to the current understanding as well a highlight some of the current areas that require further development.

Introduction

The review is intended to contextualise the current understanding of the interactions of the surface of a ferroelectric under non-equilibrium conditions in the light of excellent work undertaken last century. It shows where the new understanding is knitting together a number of diverse research topics into one thread of understanding. This current work is not intended to give a deep expose on any one topic rather highlight some of the seminal works in topical areas and bind them together. Over the past 5 years there has been an increase in the interest in the use of ferroelectric materials as photocatalysts, or their use in photochemistry. This is due to the ability of a ferroelectric material to be patterned at length scales that range from tens of nanometres to many centimetres. The different regions that have been patterned on the ferroelectric surface are both stable (with only a few exceptions) and exhibit different REDOX chemistry that is determined by the polarisation of the ferroelectric. The possibility of using such materials in a host of optoelectronic devices is also covered due to the effective electron hole separation that can be achieved.

This review will cover the historical perspective of the semi-conducting nature of ferroelectric materials which is the natural pre-cursor to investigating the photochemistry, and then focus on the new developments of patterned surfaces being used for selected chemical reactions. It will conclude by looking at some of the possible future implications, and applications of the results. Work focussing on the semi-conductor nature of a ferroelectric has shed light on the properties and phenomena occurring on the surface of the ferroelectric material under the non-equilibrium conditions of irradiation by super band gap irradiation. It also gives some indications as to what is happening at the interface between a poled ferroelectric material and its wider environment. Prior to the publication by Kalinin et al. in 2002 [1], where a novel paradigm for the assembly of 3-D nanoparticles on a ferroelectric surface, was

D. Tiwari · S. Dunn (✉)
Nanotechnology Centre, Cranfield University,
Cranfield MK43 0AL, UK
e-mail: s.c.dunn@cranfield.ac.uk

Available online at www.sciencedirect.com
ScienceDirect
Journal of the European Ceramic Society 29 (2009) 2799–2805
www.elsevier.com/locate/jeurceramsoc

Influence of annealing on the photochemical deposition of silver onto PZT thin films under UV irradiation

Divya Tiwari, Steve Dunn *

Nanotechnology Centre, Bldg. 30, Cranfield University, Beds, MK43 0AL, UK

Received 8 September 2008; received in revised form 12 March 2009; accepted 23 March 2009
Available online 25 April 2009

Abstract

Silver nanoparticle deposition from an aqueous solution of 0.01 M silver nitrate solution onto the c^+ domain of PZT (30/70) thin films has been investigated for samples annealed at a variety of temperatures from 530 to 690 °C. The impact of annealing was to increase the deposition of photoreduced silver on the surface. When the PZT samples were annealed in air at temperatures ranging from 530 to 690 °C the silver deposition increased by more than 200%. The increase in the deposition of the silver is attributed to increase in the defect concentration due to the volatilisation of components from the PZT, most importantly PbO. Variations in the Pb concentration of the sample are measured using EDX and show a marked change, reduction in Pb, with annealing temperature.

Keywords: PZT; Defects

1. Introduction

Over the past few years there has been an increase in the interest in the use of ferroelectric materials as photocatalysts, or their use in photochemistry. The historical perspective of the semiconducting nature of ferroelectric materials is the natural pre-cursor to investigating the photochemistry. What is most interesting is the use of patterns on ferroelectric surfaces that can be used for spatially selected chemical reactions. Initially Giocondi and Rohrer[1] demonstrated that it was possible to spatially separate the reduction and oxidation processes on the surface of a ferroelectric material using barium titanate. This was quickly followed by the work of Kalinin et al.[2] who developed an interesting approach for the growth of nanostructures of metals which they called 'ferroelectric nanolithography'. The technique highlighted the possibility of growing metallic nanostructures on predefined locations of a ferroelectric surface. The exact location of surface reaction was defined by the availability of photoexcited carriers at the surface of the ferroelectric. Either electrons for reduction or holes for oxidation of solvated species. The selective deposition process is attributed to the interaction between the space charge region (SPR) developed in the ferroelectric resulting from the internal dipole formed by the displacement of ions in the crystal lattice. The SPR induces photoexcited carriers to separate near the surface; electrons to migrate to the surface on a c^+ domain while holes migrate to the surface on a c^- domain.

When a photosensitive material, such as a ferroelectric, is exposed to super band gap irradiation photoexcited charge carriers (e^-–h^+) pairs are generated.[3] These charge carriers are established in the ferroelectric material and driven apart by the internal electric field in the SPR. As described earlier in positively polarized domains electrons are forced to migrate towards the surface[4] and in negatively polarized domains electrons move away from the surface and towards the bulk.

In the vicinity of surfaces and interfaces of ferroelectric materials a polarisation bound charge σ exists which is:

$$\sigma = P\,n \tag{1}$$

where σ is surface or polarisation charge, P is polarisation vector and n is unit vector normal to the surface. This induced surface charge may be compensated by two possible mechanisms – internal and external screening. External screening involves surface adsorption of oppositely charged molecules or ions on the surface of the ferroelectric. Internal screening involves

* Corresponding author. Tel.: +44 01234 754066; fax: +44 01234 751346.
E-mail address: s.c.dunn@cranfield.ac.uk (S. Dunn).

0955-2219/$ – see front matter © 2009 Elsevier Ltd. All rights reserved.
doi:10.1016/j.jeurceramsoc.2009.03.018

Materials Research Bulletin 44 (2009) 1219–1224

Contents lists available at ScienceDirect

Materials Research Bulletin

journal homepage: www.elsevier.com/locate/matresbu

Impact of Zr/Ti ratio in the PZT on the photoreduction of silver nanoparticles

D. Tiwari *, S. Dunn, Q. Zhang

Building 30, Nanotechnology Centre, Cranfield University, Cranfield, MK43 0AL, UK

ARTICLE INFO

Article history:
Received 11 November 2008
Received in revised form 6 January 2009
Accepted 22 January 2009
Available online 3 February 2009

Keywords:
A. Semiconductors
A. Nanostructures
D. Surface properties
D. Ferroelectricity

ABSTRACT

Silver nanoparticle deposition from an aqueous solution of silver nitrate onto the surface of PZT thin films of stoichiometric compositions $PbZr_{0.3}Ti_{0.7}O_3$ and $PbZr_{0.52}Ti_{0.48}O_3$ has been investigated. The impact of Zr/Ti ratio on the photochemical properties of PZT is shown by the preferential growth of silver nanoparticles onto the surface. Photoreduction of silver occurs on both c^+ and c^- domains on $PbZr_{0.52}Ti_{0.48}O_3$ whereas it occurs only on c^+ domains on a $PbZr_{0.3}Ti_{0.7}O_3$ surface. The difference in deposition pattern is attributed to difference in magnitude of spontaneous polarization, effective hole concentration and band gap of the two samples which impacts shape and width of space charge layer in the two samples resulting in a change in band bending at the surface.

1. Introduction

Nanostructured materials and systems have generated intense scientific and technological interest over the last few years because of their unique properties and potential applications in areas as diverse as electronics, optics, information storage, bio-medicine, sensors and product labelling. A variety of interesting approaches have been developed for the growth of nanostructures. One of them is ferroelectric nanolithography [1], which facilitates the growth of 3D nanostructures on predefined locations on a ferroelectric surface.

Ferroelectric materials are now considered and treated as wide band gap semiconductors rather than insulators [2]. In ferroelectric materials such as lead zirconate titanate $(PbZr_xTi_{1-x})O_3$ a polarization bound charge exists in the vicinity of surfaces and interfaces which is compensated by internal and/or external screening. External screening involves surface adsorption of oppositely charged molecules or ions from the atmosphere on the surface of the ferroelectrics. Molecules with a dipole can also orient themselves on the surface to screen charge. Internal screening involves compensation of surface polarization charge by defects and free charge carriers in the bulk of the material and takes the form of space charge region (SCR) due to 'band bending' at the surface [3].

When a photosensitive material such as a ferroelectric is exposed to high energy UV light, photoexcited charge carriers (e^-–h^+) pairs are generated in both the surface layer and the bulk of the film as deep as the absorption limit. These charge carriers are driven apart by the internal electric field in the SCR. In the positively polarized domains electrons are forced to migrate towards the surface [4] and in negatively polarized domains electrons move away from the surface and towards the bulk. When the ferroelectric surface is dipped in a silver salt ($AgNO_3$) solution and exposed to UV light, the metal cations can react with photoexcited electrons available on c^+ domains and are reduced to silver metal. It is also possible to produce PbO by oxidation of lead salts on the negatively poled domains. The photoreduction and photoxidation reactions on c^+ and c^- domains are described by reactions (1) and (2) respectively.

$$Ag^+ + e^- \rightarrow Ag^0 \quad (1)$$

$$Pb^{2+} + 2H_2O + 2h^+ \rightarrow PbO_2 + 4H^+ \quad (2)$$

On a positive (c^+) domain the Ag^+ ions should not be intimately attached to the c^+ surface and in fact the negatively charged counter ions would be forming a Stern or double layer [5]. Therefore there was a tunnelling mechanism that was allowing the electrons to pass through the bound ions and reduce the metal cations to metal. Recent works by Giocondi and Rohrer [6] show that similar domain specific reactivity exists on the surfaces of ferroelectric microcrystal owing to the existence of dipolar field effect. Similar spatially selective oxidation and reduction reactions were observed on non-ferroelectric $SrTiO_3$ surfaces [7].

* Corresponding author at: Building 30, Materials Department, Cranfield University, Cranfield, Bedfordshire, MK43 0AL, UK. Tel.: +44 1234 750111x2723; fax: +44 1234 751346.
E-mail address: d.tiwari@cranfield.ac.uk (D. Tiwari).

0025-5408/$ – see front matter © 2009 Elsevier Ltd. All rights reserved.
doi:10.1016/j.materresbull.2009.01.016

Influence of ferroelectricity on the photoelectric effect of $LiNbO_3$

S. Dunn[a] and D. Tiwari
Building 30, Nanotechnology Centre, Cranfield University, Cranfield MK43 0AL, United Kingdom

(Received 13 June 2008; accepted 12 August 2008; published online 5 September 2008)

A comparison between domain dependent photochemical and photoelectric cation reduction in $LiNbO_3$ is presented. The reduction in photoelectric threshold for $LiNbO_3$ due to the depolarization field allows UV irradiation to produce free electrons that can participate in photochemical reduction in silver nitrate. This is in addition to domain directed photophysics, where influences on the space charge layer due to the internal dipole of a ferroelectric determine the carrier at the surface. We show that the interaction of photoelectric and domain dependent influences is observed in $LiNbO_3$ due to the low electron affinity (~1–1.5 eV) and band bending (0.3–0.8 eV). © *2008 American Institute of Physics*. [DOI: 10.1063/1.2978195]

There has been a growing interest in the study of the photophysics and chemical and photochemical interactions of ferroelectric materials since the late 1990s.[1] At this time some of the early confusions regarding the nature of the interaction between the semiconducting and ferroelectric properties of the materials are being resolved. Furthermore interesting work from Giocondi and Rohrer[2] demonstrated that it was possible to spatially separate the reduction and oxidation processes on the surface of a ferroelectric. This was resolved by examining the influence of the internal dipole of a poled ferroelectric on the space charge layer and has led to a number of publications highlighting the influence of semiconductor physics on the surface photochemistry of ferroelectric systems.[3,4]

In the case of a c^+ domain there is downward band bending and so e^- is driven to the surface, while in a c^- domain there is upward band bending and h^+ is driven to the surface. In e^- we have a surface that acts to reduce species in contact with the surface, and a surface with h^+ is oxidative. The exact degree of reductive or oxidative power of this mobile carrier is determined by the relative position of the conduction and valence bands. It is now commonly accepted that the value of the normal hydrogen electrode (NHE) in electrochemical terms lies at 4.5 V (or 4.5 eV) from vacuum.[5] It is, therefore, possible to map an electrochemical potential against the band structure of a semiconductor and determine whether there will be a reduction or oxidation of solvated species on the semiconductor.

The degree of band bending that is influenced by the dipole of the ferroelectric is determined by a number of factors that include the defect density and magnitude of remnant polarization.[6] It must also be considered that a ferroelectric material can screen the internal polarization by external screening, which increasingly happens as the defect density reduces or remnant polarization increases. Examples of opposite effects are lead zirconate titanate (PZT) where a high number of defects allow almost complete internal screening and $LiNbO_3$, where there is a significant degree of external screening due to low defect numbers. Interestingly there is also an influence on the photoelectric effect seen on poled semiconductor systems as was demonstrated in 2004 by Yang *et al.*[7]

The interesting questions that arise from the studies on $LiNbO_3$ that have been undertaken so far relate to the subtle differences seen in the work undertaken. Two different broad observations have been published—one shows photo assisted deposition on domain boundaries[8] and the other is deposition across the bulk of a poled domain.[9] The differences in the results presented in these reports are in the wavelength of irradiation and power of the source used. In cases where a high power and therefore higher flux of photons is generated, then complete domain decoration according to domain dependent coverage is observed. When a lower power output is used then only domain boundaries are sites of nucleation.[3]

In this work, we have used a single crystal $LiNbO_3$ that has been poled to present either c^+ or c^- face. $LiNbO_3$ (z cut from MTI Corporation) is known to have a Curie temperature of 1210 °C with polarization along the c axis. Experiments were conducted using a high energy (400 W) UV bulb produced by Honle, which gives irradiation from 200 nm to the band gap energy of $LiNbO_3$ at ~320 nm.[6] Each sample was 0.5 mm^2 and adhered to a glass slide substrate using a silver loaded epoxy. Irradiation was performed under 0.01M silver nitrate solution (Aldrich 99.99%) that was freshly prepared for each sample. A Veeco Dimension 3000 scanning probe microscope was used to investigate the coverage of the $LiNbO_3$ after irradiation with the UV and prior to deposition.

Figure 1(a) shows the coverage of silver nanoparticles as deposited on the c^+ domain of the $LiNbO_3$. This image is consistent with a previous work published in the field where the band bending of the semiconductor produces an interface to which either e^- or h^+ is preferentially driven. The pattern

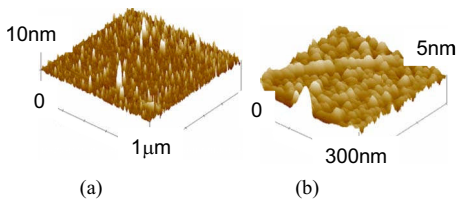

FIG. 1. (Color online) (a) Scanning probe microscopy image (z scale is 10 nm and field of view is 1 μm) of silver nanoparticle growth on the c^+ domain of $LiNbO_3$. (b) Localized nanowire formation due to subsurface defects (z scale is 5 nm and field of view is 300 nm).

[a]Author to whom correspondence should be addressed. Electronic mail: s.c.dunn@cranfield.ac.uk.

THIS PAPER MUST BE CITED AS:

Journal of Materials Chemistry, 17 (2007),

4460–4463

Insights into the relationship between inherent materials properties of PZT and photochemistry for the development of nanostructured silver.

Steve Dunn, Divya Tiwari, Paul M. Jones and Diego. E. Gallardo*

Nanotechnology Centre, Cranfield University, Building 30, Cranfield, MK43 0AL, United Kingdom

s.c.dunn@cranfield.ac.uk

Abstract

Recently there has been great interest in using patterned ferroelectric materials for the photochemical growth of metal nanostructures. Variations in surface and sub-surface structure influence the photochemical processes. Here we show that crystallography, and hence remnant polarization, of the ferroelectric affects photo-deposition. The ratio of metal growth on c^- and c^+ domains varies from 1:2 for [100] to 1:100 for [111]. This is shown to be dependent on the variations in the band structure.

APPENDIX B. CONFERENCES

Conferences

1) Presentation

i) Growth of Ag nanoparticles on PZT thin films under UV irradiation: Impact of defect concentration.

Ferroelectrics UK 2007 Conference, Dundee, UK, 20-21 August.

2) Poster presentation

i) Growth of Ag nanoparticles on PZT thin films under UV irradiation: Impact of defect concentration. **(Best Poster prize)**

Electroactive Materials 2007 Conference, Cranfield, UK, 20 September.

ii) Photo induced chemical interactions on PZT surfaces; an insight into semi-conducting behaviour.

Ferroelectrics UK 2007 Conference, Dundee, UK, 20-21 August.